POLITECNICO DI MILANO

School of Industrial and Information Engineering

Master of Science in Engineering Physics

Integrated Optical Biosensing Assays exploiting Magnetic Labels

Supervisor:

Prof. Riccardo BERTACCO

Co-supervisor:

Dott. Ing. Nicola PESERICO

Master Thesis of:

Chiara GROPPI

ID: 876175

Academic Year 2017–2018

Contents

List of Figures

Sommario

I biosensori sono oggi presenti e largamente utilizzati nelle analisi biochimiche. Il recente progresso scientifico e tecnologico ha portato questi dispositivi a ricoprire un ruolo sempre più importante in molteplici settori applicativi, tra i quali diagnosi mediche, monitoraggio ambientale, controllo alimentare, rilevazione di droghe, difesa e sicurezza. Al giorno d'oggi, sono disponibili numerose tecnologie volte all'implementazione dei biosensori, ma la ricerca in questo campo è sempre puntata allo sviluppo di nuove soluzioni innovative che permettano di ottenere per questi semplici, compatti dispositivi lab-on-chip alti livelli di sensibilità, rapidi tempi di risposta, ampio range dinamico.

In questo contesto, il presente lavoro di tesi si è concentrato sullo studio, lo sviluppo e la validazione di metodi di biorilevamento che utilizzano la tecnologia dell'ottica integrata combinata con campi magnetici in strategie di rilevazione "label-based" di agenti biochimici. I metodi utilizzati sono stati sottoposti ad analisi e studi di ottimizzazione delle performance, con lo scopo di fare di loro una valida alternativa ad alcune delle tecniche di biorilevamento ottico più comuni con alti livelli di sensibilità e robustezza.

Abstract

Biosensors are nowadays largely and extensively employed in biochemical analyses. As a result of recent scientific and technological progress, such devices play an increasingly important role in many sectors of human endeavour, including medical diagnosis, environmental monitoring, food control, drug discovery, defense and security. Today, several technologies are available for the implementation of biosensors, but research in this field is always looking for new innovative solutions aimed to achieve higher sensitivity, faster responses, wide dynamic range of these simple, inexpensive, compact, lab-on-chip devices. Within this framework, the present thesis work was focussed on the study, development and validation of biosensing methods employing integrated optics technology combined with magnetic fields in label-based sensing strategies for biochemical agents. Appropriate optimization studies regarding the performances of the applied methods were carried out, in the view of achieving a suitable alternative to some of the most common optical biosensing techniques with high levels of robustness and sensitivity.

Introduction

The biosphere contains a myriad of substances that can influence, inhibit, aggravate or stimulate many different aspects of the health and behaviour of whole living organisms or systems. That is why, over the last decades, the potential development of a range of detection and sensor technologies able to monitor and estimate biological substances has been raising significant interest in the scientific sphere. This development has lately been subjected to rapid acceleration because of the recently estimated commercial potential of these systems and processes and because of the emergence of biotechnology-based industries. At the same time such sensing devices, or biosensors, have been considered significantly useful to promote advancements in several fields of analytical biotechnology, including health care, veterinary, agricultural, petrochemical and pollution monitoring.

A major role in the development boost in the field of biosensors is undoubtedly retained by the rapid advances in health care technology. The maintenance of health is one of the most laudable technological objectives challenging science and technology, and diagnosis is an essential prerequisite for disease treatment and prevention. The possibility of instant analyses of clinical samples and of continuous in vivo monitoring of metabolites, drugs, and proteins using miniature, highly portable systems is undeniably appealing for many medical applications. The most representative clinical example is the glucose sensor for diabetes, which has become a very popular reliable implementation of

biosensing technology, today accounting for 85% of the gigantic world market, and it still retains a recognition ability that has proven superior to many newly developed sensors. The increasing costs of healthcare and the always present consumer demands are likely to promote a new generation of inexpensive wearable, integrated and less-invasive sensors eligible for mass production to support the maintenance of wellbeing, care of the elderly, pharmaceutical development and testing, and distributed diagnostics.

Over the last few years there has been a growing interest in the application of biosensors to other fields. From the medical area biosensing-related researches are starting to influence the veterinary areas and animal husbandry. Recently growing concerns about food quality has led food industry to the appreciation of rapid methods for estimating levels of aliment deterioration and contamination. The rise of biotechnology has stimulated investigations into industrial process monitoring, promoting research on sensors for pollutants such as carbon monoxide and herbicides, due to the increasing concerns about natural environment. The military field is focussing on biological and chemical defense, especially against possible biowarfare agent threats.

To conclude, many new biosensing methods and technologies are emerging, and the study of new cutting-edge technologies is still a fundamental aspect many scientific researches.

0.1   Outlook on the thesis

The work described in this thesis was performed at Polifab, the micro- and nanofabrication facility of Politecnico di Milano, as a part of a project resulting from the collaboration between the Photonic Devices group of Prof. A. Melloni and the Spintronics group of Prof. R. Bertacco. The work also included the collaboration of ICRM-CNR group of Dr. Marcella Chiari for the

functionalization of the biosensors. From this work a regional project started (Ready project, 2017-2019), involving the collaboration of several partners, including Sacco hospital and CNR.

The goal of the project consists of combining the optical sensing technology with the use of magnetic nanoparticles, in order to obtain an innovative sensing platform characterized by robustness and better sensitivity with respect to other usual methods. The first part of the project is focussed on the sensitivity improvements that can be achieved exploiting magnetic beads as passive labels: the latter have a significant impact, with respect to the only target analyte, on the effective refractive index change felt by light propagating in an optical waveguide near the sensitive surface of the biosensor. This has been demonstrated employing immunosensing assays for antibody-antigen-antibody sandwiches. The second part concerns the possibility of combining optical sensing, magnetic beads, and magnetic fields. The detection of magnetic-induced actuation of complexes made of double-stranded DNAs attached to magnetic beads is a novel and innovative technique that, with its coherent detection, increases the robustness of the optical biosensor.

The thesis work was focussed on the study of the various physical processes involved in the operation of the biosensing optical and opto-magnetic assays and on the validation of the properties of the developed platform. The contents of the 5 Chapters of this thesis are briefly summarized hereafter:

1. **Biosensors**. This chapter focusses on the introduction of the concept of biosensor. The main biosensing techniques, transducing methods and applications are described, with a particular focus on immunosensors. Moreover, the possible introduction of labels in bioassays is discussed, mentioning advantages and disadvantages of label-free and label-based techniques, and the passive and active labelling strategies are explained, referring in particular to the case of magnetic nanoparticles.

2. **Theoretical aspects**. This chapter is devoted to the theoretical considerations and models concerning the operation of the employed optical and opto-magnetic methods. In first part of the chapter the main aspects of biochemical interactions, optical waveguides and resonators, and superparamagnetic nanoparticles are introduced, while the second part describes the application of optics and magnetism to biosensing assays, and the concept of the opto-magnetic platform is presented.

3. **Experimental methods**. In this chapter the main set-up components employed during biosensing tests are described. These include microchip characteristics, biochemical functionalization methods and hybridization protocols, optical and electronic components of the measurement set-up with a focus on the geometry and structure design of the electromagnet needed to generate the magnetic field.

4. **Experimental results**. In this chapter the main experiments carried out for the study, validation and optimization of the methods are presented. The optical sensing technology was employed for biosensing experiments with HIV antigen p24 sandwiched between two antibodies, while the opto-magnetic platform was used with DNA molecules varying some physical parameters in order to identify the optimum conditions maximizing the analytical performances of such strategy.

5. **Conclusions**. This chapter briefly summarizes the obtained results, the achieved goals and the fundamental considerations, mentioning also future perspectives both terms of improvements and potential applications of the developed platform.

Chapter 1

Biosensors

In this chapter a general introduction on the concept of biosensor is provided, mentioning its working principle and fundamental figures of merit to assess the reliability of the employed biosensing method and the main physical transducing principles that can be exploited to obtain measurable signals from biochemical interactions. The focus is on immunosensors, a specific kind of biosensing devices dealing with antibodies and virus recognition. Finally, the label-free and label-based strategies, and how they can provide significant signals within the considered immunosensing or biosensing technique are described and compared. The possible labels and label properties that can be used are described, focussing on magnetic particles and their applications in the biological field.

1.1 Concept and overview

A chemical sensor is an analytical device that is able to transform chemical information, ranging from the concentration of a specific sample component to the global composition analysis, into an analytically useful signal [4]. Such chemical sensor comprises the following fundamental components combined together to generate the signal:

i) A receptor, i.e. a molecular recognition system.

ii) A physico-chemical transducer (electrochemical, electrical, optical, thermal, etc.), which converts the response coming from the output domain of the recognition system into a measurable signal, exploiting different property changes or signal generation that occur after the binding event. The transducer part of a sensor is also called a detector or sensor.

iii) A signal processor, i.e. electronic devices and circuits, and appropriate hardware or software for acquisition and processing of the signal and conversion into a readout.

When the receptor is a biological element (such as an enzyme, antibody, microorganisms, nucleic acid), the device is called a biosensor. A bioreceptor will specifically bind to a target analyte and cause the transducer to generate a measurable signal for detection of target compounds (see Figure 1.1) The biocomponent determines the degree of selectivity or specificity of the biosensor whereas the sensitivity of the biosensor is greatly influenced by the transducer. Ideally speaking, biosensors must be highly specific, independent of physical parameters such as pH and temperature and should be reusable. Additionally, all these processes must be carried out at a small scale, with sample volumes of the order of microliters, and this often requires the use of microfabricated structures and microelectronic circuits. Finally, biosensors can profit from the
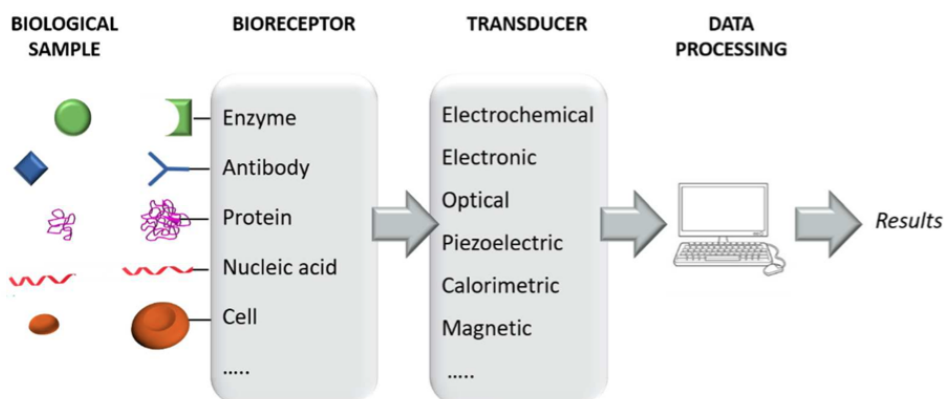
Figure 1.1: Main components of a biosensor and principal steps of a generic biosensing assay. Target solution comes in contact with the surface of the biosensor, which is provided with appropriate biological receptors; the recognition reaction takes place and the system response is detected by the transducer, and subsequently turned into a measurable signal. Data processors operate by means of suitable electronic systems to yield quantitative responses.

benefits of nanomaterials and nanostructures [5] [6], such as large area to volume ratio, superparamagnetism, and surface enhanced resonance spectroscopy among many others, allowing highly sensitive and convenient transduction of the resulting binding and catalytic events. Nanotechnology is rapidly emerging as key enabling technology for the development of biosensors. Besides, production of more robust, versatile and widely applicable sensors is possible thanks to the emergence of semi-synthetic and synthetic receptors. Therefore, the biosensors field is by no means an exclusively biological field, but a truly multidisciplinary one.

Potential uses embrace virtually every conceivable analytical task, ranging from medical diagnostics through drug discovery, food safety, process control and environmental monitoring, to defense and security applications (see Section 1.1.2).

1.1.1 Figures of merit

The fast diffusion of biosensors and their diversity has led to a lack of rigorous definitions of performance criteria. In order to demonstrate the quality and the significance of the results of an analytical procedure, the validation of the used method is an essential step. This can be carried out by assessing its figures of merit, which are quantities concerning the methods, the used analytes and the results of the procedure assessing the quality of the whole process. It is useful to establish standard protocols for evaluation of performance criteria, in accordance with standard IUPAC definitions and protocols [7]. Some of the most important figures of merit characterizing sensor performances are here discussed.

- Sensitivity is the slope of the analytical calibration curve, and it is well defined within the linear response range of the applied method. When the slope is large, it means a small change in analyte concentration produces a big variation in the detected response signal.

- Selectivity is the ratio of the slopes of the calibration curves of the analyte of interest and a particular interference, useful to assess analytical reliability of a sensing procedure. A method is said to be selective if the response of the considered analyte is by far superior with respect to all the other responses, and is therefore able to discriminate and quantify the presence of the analyte in presence of interferences and spurious contributions.

- Limit of detection (LOD) is a measure of the analytical capacity of a specific procedure. It is usually the smallest concentration, or the quantity derived from the smallest signal, detectable with acceptable degree of certainty for a given method. It can also be defined as the ability of a biosensor to discriminate a signal from the instrinsic instrumental background noise [8].

- Repeatability refers to the amount of agreement between results obtained in successive measurements performed always in the same conditions in terms of apparatus, operator, period of time.

- Reproducibility is in principle similar to repeatability in terms of assessing the analytical variability, but refers to measurements carried out in different conditions related to place, time, apparatus.

The reliability of biosensors for given samples depends both on their selectivity and their reproducibility. It has to be determined under actual operating conditions, therefore even in the presence of possible interfering substances. A reliable biosensor should offer a response that is directly related to the sample analyte concentration and should not vary with fluctuations of concentrations of possible interfering substances present within the sample. Therefore, the analyst should assess the accuracy of the application by stating the reasonable interferants to be considered and how to quantify their influence on the system.

The operational stability of a biosensor response may vary considerably depending on the sensor geometry, method of preparation, as well as on the applied receptor and transducer. Also operational conditions (the analyte concentration, the continuous or sequential contact of the biosensor with the analyte solution, temperature, pH, buffer composition, etc.) strongly influence stability. Although some biosensors have been confirmed usable under laboratory conditions for more than one year, their practical lifetime is either unknown or limited to days or weeks when they are incorporated into industrial processes or to biological tissue.

1.1.2 Transducing principles and applications

There are many criteria that can be adopted to classify the existing biosensors: according to their applications (i.e. in food safety, environmental moni-

toring, clinical analysis, and medical diagnosis), on the basis of the transducer principle (electrochemical [4] [9] [10], optical [11] [12], piezoelectric [13] detection etc.), of the biochemical recognition element that takes part in the sensing process (i.e. enzymes, antibody/antigen, nucleic acids and whole cells, DNA fragments, membrane components, organelles or intact cells etc.).

Three popular transducer principles employed biosensing purposes are briefly discussed below.

Electrochemical biosensors are integrated devices that provide a specific quantitative or semi-quantitative information through a biorecognition reaction and an electrochemical transducer (which can be a pair of electrodes, field-effect transistors or other types of devices). They can be characterized by high sensitivity and selectivity, portability, low cost and rapid response times. The measured electrical signal shows significant differences in magnitude if the biorecognition reaction takes place. The main electrochemical transducers are amperometric (measuring of current), potentiometric (measuring of electrode potential or voltage differences) and conductimetric (measuring of conductivity or resistance). Recently, carbon nanotubes have have been studied for applications to electrochemical biosensors, because electrodes modified with carbon nanotubes highly improve the performances due to their reduced dimensions and peculiar electronic structure [14].

Optical biosensors consist of a light source, as well as numerous optical components to generate a light beam with specific characteristics to address the beam onto the sample. In this case, either an optical signal (e.g. color or fluorescence) or a change in the optical properties of the surroundings (such as absorption, reflectance, emission, refractive index, and optical path) is generated because of the biochemical reaction. The optical signals are then collected by a photodetector and converted into electrical signals that are further electronically processed [15]. They are powerful and versatile detection instruments that

allow for a high signal-to-noise ratio and require small reagent volumes. Besides, they can reach high sensitivity and accuracy and wide detection capacity, they are immune to electromagnetic interference and are appreciated for their ease of operation and possibility of remote sensing measurements. Common sensing methods include fluorescence spectroscopy [16], interferometry [17], reflectance [18], chemiluminescence [19], light scattering or refractive index-based methods [20].

Piezoelectric biosensors exploit specific kinds of materials that resonate when an external oscillating electric field is applied. Employing quartz crystals is very common, and the interaction between a free analyte in solution and a ligand immobilized on the crystal surface produces a mass change that reflects in a change in the quartz oscillation frequency.

As regards the possible applications of biosensors, these devices have proven useful in many fields and often provide better stability and sensitivity with respect to the traditional methods. Among the many involved areas we find:

- Food processing industry, where biosensors allow to overcome the limitations of traditional chemical and spectroscopic methods allowing for simple, inexpensive, real-time techniques for monitoring of food quality and safety, and food authenticity and conservation [21].

- Fermentation industries, in which the working efficacy of biochemical reactors is optimized by means of effective monitoring of the fermentation processes. Thanks to biosensors, this goal can be pursued with simple instrumentation, formidable selectivity, low prices and easy automation [22].

- The medical field, in which the applications of biosensors are growing rapidly. There is an increasing interest in biosensors because of the possibility for infectious disease diagnosis. For example, the interaction between

the antibody and antigen can be studied and monitored [3], and bio-recognition of the protein is achieved. The most successful application of biosensors in clinical analysis is the electrochemical determination of glucose in blood by encapsulating the glucose oxidase enzyme (GOx) within polyethylene on the metal electrodes [23] and measuring the amount of oxygen consumed by the enzyme. Such biosensors are now commercialized in different configurations available mostly in single-use formats for self monitoring of blood glucose [24].

- Biodefense biosensing applications, which involve for example the military need of preventing biological attacks. The aim of such biosensors is to sensitively and selectively identify organisms (such as bacteria, toxins and viruses) called biowarfare agents that pose threat in real time [21].

- Environmental monitoring, for high-sensitivity real-time detection of pollutants and contaminants (such as heavy metals, phenols, surfactants, pesticides) that are released in the environment by industrial processes, in order to guarantee sustainability of industrial products and economy [25].

1.2 Immunosensors

As explained above, biosensors are devices able to recognize and analyze specific biomolecules of interest. Antibodies are one of the most studied and most employed kind of bioreceptors [26] [27]. Antibodies are proteins generated by the immune system to identify antigens, generally protein molecules, but they can also recognize a virus particle or a bacterium by recognizing the proteins on its surface. The affinity between antibodies and antigens, though of non-covalent nature, is very strong. In addition, antigens can also be used as bioreceptors to capture and analyze specific antibodies. Biosensors that utilize

antibodies or antigens as bioreceptors are called immunosensors, and are widely being investigated and developed for practical applications, included in the ones mentioned in Section 1.1.2. Such devices are much more superior in sensitivity and specificity to other types of biosensors, because of the high specificity of antibodies binding to proteins, viruses, bacteria, cells, etc. Just like the other biosensors, immunosensors comprise different transducing principles, which include electrochemical, optical and piezoelectric.

Immunosensors have become very popular recently, and one particular assay protocol that is worth mentioning because it has dominated over the others is the enzyme-linked immunosorbent assay (ELISA) [28]. In ELISA, first, the antibody is immobilized on a solid surface. Empty spaces on a surface are filled with a passivating protein, typically bovine serum albumin (BSA), to prevent non specific reaction. A target solution is dispensed onto this surface, and antibody-antigen binding occurs if there is a complementary antigen in the target solution. In order to add more stringency to the test and be able to reveal the binding event through the generation of a physical signal, additional materials that will bind specifically to the target molecule as well as generating optical or electrochemical signals are added. Indeed, first, the same antibody is added (called secondary antibody) to the surface, which should specifically bind to the target antigen. As a result, the latter is sandwiched between two identical antibodies. In this sense, ELISA is often referred to as sandwich immunoassay. Afterwards, a label particle, which is typically pre-conjugated (through covalent binding) with an enzyme or a fluorescent dye, is added to specifically bind to the secondary antibody. If the label is tagged with a fluorescent dye, for example, a light source and a light transducer pair are used to detect its optical signal. The more targets are present on the surface, the larger the generated signal. Such an assay can be employed to detect antigens using antibodies, but also antibodies using antigens. In the latter case, the

ELISA plate should be pre-immobilized with antigens rather than antibodies, and the secondary antigens must be covalently conjugated to an appropriate enzyme. A good example of antibody assay using antigen as bioreceptor is the detection of human immunodeficiency virus (HIV) [29], which causes acquired immune deficiency syndrome (AIDS). The amount of HIVs in human body is typically very small that is hard to detect. The presence of HIVs in human body triggers the generation of a substantial amount of antibodies against them (anti-HIV), which are a lot easier to detect. Another advantage of antibody sensor biorecognition elements is that the immunogen, i.e. target, need not be purified prior to detection.

The performance of ELISA and other immunosensors is greatly affected by the choice of the used antibodies. The latter are generally produced by injecting into animals' bodies, usually mice, rats or rabbits, a specific antigen, that is identified by the immune system. This recognition translates into a production of a mixture of antibodies that recognize different portions (called epitopes) of the antigen. This "mixture" of antibodies able to recognize different epitopes of the same antigen are called polyclonal antibodies (pAb). However, certain epitopes are sometimes common to more than one bacterium, and this raises the problem of cross-reactivity, i.e. the non-absolute specificity of the antibody-antigen pair. Therefore, there is a need to develop an antibody that recognizes only one type of epitope, called monoclonal antibody (mAb) [30]. These mAb are widely used in ELISA and other immunosensor applications whenever a higher specificity is required.

Moreover, some scientists believe that aptamers could be a valid alternative to antibodies [31]: these are, essentially, artificial nucleic acids (single-stranded DNA or RNA) that recognize or bind to specific antigens, just like antibodies. The small size of aptamers (antibodies are relatively big, with molecular weight of 150 kDa) makes them less vulnerable to the denaturations caused by heat

and/or long-term storage. Progressing from semi-synthetic to fully synthetic analogues of biological receptors could furnish a new generation of sensors that display the desired sensitivity and specificity of biosensors, but lack their consequential instability and, in some instances, irreproducibility.

1.3 Label-free and label-based approach

The quantification of changes between various physiological states in a biological system is highly complex in nature. Transduction in biosensors is based on the assumption that the amplitude of the signal is proportional to the amount of detected bound analyte. Reducing the overall complexity of assays in terms of steps, protocol and instrumentation is an appealing goal, but deciphering the exact abundance of targets in a solution can sometimes become problematic if the sensitivity of the method constitutes a limitation for the detectable amount of biological mass. That is why two distinct transduction approaches can be exploited: label-free detection schemes consist of configurations in which the output signal is generated directly by the interaction of the analyte with the bioreceptor, without the need for additional markers [32] [33]; alternatively, label-based detection methods are possible, which utilize stable labels that are incorporated within, or made to attach to, the biological targets, introducing a sizable difference within the experimental conditions [34]. The latter technique is now well established and widespread in the field of immunoassays for its sensibility and flexibility. The already discussed ELISA assay is itself a label-based technique, employing colour or fluorescence enzymes for labelling. Figure 1.2 shows the label-free and label-based steps for the ELISA assay. The label-free procedure simply comprises the sandwich formation, in which the addition of secondary antibodies leads to an increase of detection stringency; the label-based additional step consists of adding markers
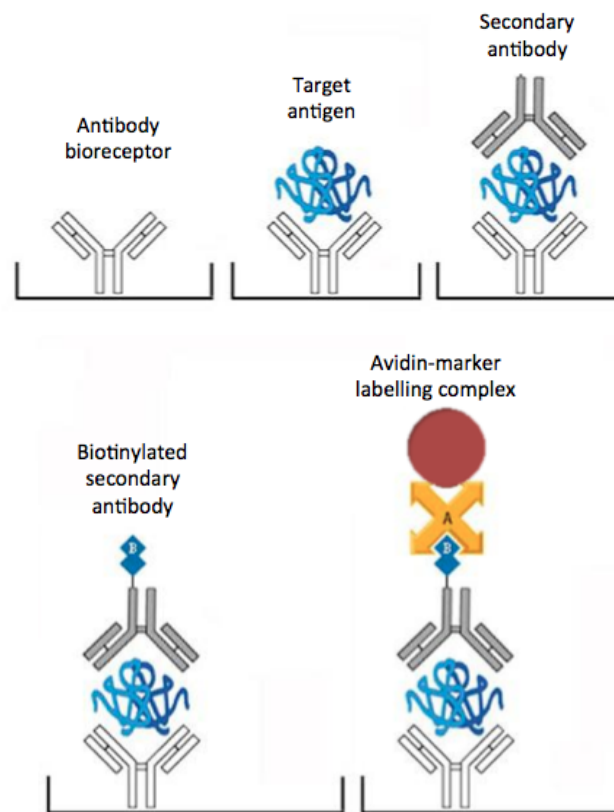
Figure 1.2: Label-free and label-based steps for the ELISA biodetection assay. The biological sandwich is detected without additional steps in the label-free strategy; the addition of markers and their binding to secondary antibodies constitutes the labelling step.

to the biological complex. A very common strategy to accomplish the binding reaction between the sandwich and labelling particles comprises secondary-antibody functionalization with biotin, a vitamin that shows very high affinity to streptavidin and avidin proteins in general. Markers can be coated with this protein so that the strong binding of biotin-avidin is exploited for a resulting highly robust complex.

Label-based biosensing is often preferred because of the enhancement in sensibility induced by the addition of detectable labels and the high robustness

of the assay due to the specific binding between the marker and the analyte target molecule, that increases the stringency reducing the possibility of false positives. Indeed, total specificity of the sample is not achievable in analyses with real biological samples, even if the bioreceptor is chosen to interact almost exclusively with the target, and some non-specific reactions may always occur. Moreover, multiplexing of different analytes in the same platform can be performed by simply employing different label species meant to bind to specific target molecules. The presence of the labels also allows to overcome the necessity for real-time measurements or comparison between signals acquired at different times, because on-off signal responses can be measured based only on the presence and properties of the label particles. This comes at the expenses of the simplicity and overall duration of the assay, because of the necessity to handle label solutions and carry out the extra binding step. For these reasons, many efforts are spent for the development of devices able to work in the label-free configuration, looking into methods of reduced complexity, time duration and costs in terms of material consumption, but still sensitive enough to recognize the small variations induced by the binding event.

Since both approaches present limitations and valid advantages, an appealing strategy can consist in combining the two types of detection, by performing a fast label-free assay with high analyte concentrations and subsequently a label-based phase providing for higher sensitivity and robustness when necessary.

1.3.1 Active and passive labels

As already explained, the introduction of labels within a bioassay strategy is functional to the aim of increasing the sensitivity and the specificity. This can be carried out in two ways, that exploit different characteristics or the markers depending on the adopted experimental method.

Markers can work as *passive* labels, i.e. the enhancement in signal amplitude in achieved by introducing a second specifically interacting particle or molecule, which carries a high molecular weight or, for optical biosensors, high refractive index tag. Therefore, only the presence of an extra mass contribution is exploited, which can result in a signal increase regardless of the extra properties of the labels [35] [36] [37]. To date, liposomes [38], latex particles [39] and certain proteins [40] have been tested as amplification tags, but also metallic nanoparticles [36] [41], because they offer ease of preparation, high density, large dielectric constant, and biocompatibility [42].

Another approach consists in employing *active* labels, which means specifically choosing them in the view of exploiting the extra intrinsic properties they may have to produce an externally observable signal. A possible advantage is that their activity can be reversibly switched on and off, so that real-time measurements during the whole assay are not necessary and possible spurious contributions due to false positives are reduced. The label may be a radio-isotope [43], enzyme [44], fluorescent molecule [45], or charged molecule [46], for example, but also electrochemically active labels such as organic dyes, metal complexes, or metal nanoparticles are employed in many electrochemical transducer methods [47]. Furthermore, magnetic nanoparticles, microparticles, or magnetic beads (see Section 2.3.2) also offer interesting possibilities in the context of active-labelling [48]: indeed, having embedded magnetic entities, they can be magnetically manipulated using permanent magnets or electromagnets. This extra degree of freedom can be exploited for both active stirring of the magnetic markers in solution independently of normal microfluidic processes and magnetic actuation of the particles attached to the probe complexes. The fact that a magnetic field gradient can be used to either remotely manipulate or selectively filter biological materials attached to a magnetic bead has led to a number of applications. An important in vivo application is using the

magnetic beads to produce a distortion in the magnetic field at a given site under examination via magnetic resonance imaging (MRI) [49]. The presence of magnetic beads strongly alters the contrast of cells, enabling visualization of otherwise non-detectable objects. Magnetic beads can also play a role in drug targeting, as they can be vectors for carrying the drug and can be magnetically guided to the desired location [50]. For in vitro applications, the possibility of the specific labeling of cells or biomolecules with magnetic microbeads has lead to advanced developments in cell manipulation and biomolecule separation, DNA sequencing, and biomolecule selection and purification. Magnetic labels have several advantages over other labels. The magnetic properties of the beads are stable over time, in particular, because reagent chemistry does not affect their magnetism, nor does photo-bleaching (a problem with fluorescent labeling). There is also no significant magnetic background present in a biological sample and magnetic fields are not screened by aqueous reagents or biomaterials. In addition, magnetism may be used to remotely manipulate the magnetic particles. Finally, a number of very sensitive magnetic field detection devices have been developed during recent years, such as giant magnetoresistance (GMR) [51] and spin-valve [52] magnetic sensors that enable the measurement of extremely weak magnetic fields, for example, the one generated by the magnetization of a single magnetic microbead.

Chapter 2

Theoretical aspects

This chapter illustrates all the relevant physical phenomena that take part in the proposed biodetection mechanism based on optical waveguides, resonators and magnetic nanoparticles. The fundamental steps that determine the functioning of the considered biosensing device are three: a biochemical reaction between the target analytes in solution with a certain concentration with the probe ligands fixed to the surface of the sensor; the interaction between the molecules and the mode within the optical resonator, which constitutes a first level of biorecognition assay in terms of a detectable change of refractive index; the exploitation of magnetic nanoparticles first as passive labels, which are made to bind to target molecules to enhance the optical transduction signal; afterwards as active labels, by magnetically actuating them via an applied AC magnetic field, thus generating a suitable signal for a second level investigation.

Therefore, in the first part the dynamics of the biochemical reaction are described, as they can strongly affect the measurements, afterwards the main features and parameters of optical waveguides and resonators are introduced and finally the magnetic aspects of the used nanoparticles are explained.

In the last part, all these notions are put together in the biosensing context to describe the concept and the working principles of the optical and opto-magnetic detection methods.

2.1 Biochemical interaction model

In biosensing assays, the interaction dynamics between the involved substances at a molecular level are of vital importance, because it is what mostly characterizes this kind of analysis. The interaction between two molecules resulting in a stable association, in which the molecules lie close together, is what molecular binding is about. It can be covalent or non-covalent, the second one being the most common, highly dependent on the affinity between molecules and, in certain conditions, possibly reversible.

Recently, many simple assay methods have been described, based on the interaction between a diluted analyte solution and a surface containing a certain concentration of ligands fixed via coating techniques. Many high-sensitivity methods allow to distinguish the single binding event, provided a high sampling rate is also available.

Regardless of the physical method involved in the biosensing technique for detection of binding dynamics, however, the performance of the device will be influenced by the chemical factors determining the degree of binding. The most important factors to be taken into account in binding events are the equilibrium and the kinetics of the reaction, to be combined with the study of mass transport dynamics of the analyte species travelling towards the surface, where the interaction with fixed ligands actually takes place.

Many theoretical models can be found in literature: here, Eddows's approach for immunochemical sensing developed for fixed antibody-antigen binding interaction [53] is presented. This model will be applied to two specific kinds of binding processes:

i) single-stranded DNA molecules binding to their complementary fixed to the sensor surface;

ii) the sandwich-based assay for p24 HIV protein, implemented by first dispensing the p24 protein and afterwards a solution of secondary antibodies which bind to the p24 so as to increase the stringency of the biomolecular recognition.

2.1.1 Equilibrium dynamics

Let's begin by considering a surface S coated with a matrix of immobilized ligands, and a volume V of solution containing the analyte A, with concentration [A] expressed in moles per liter (M). The adsorption and desorption rates (units: moles $\cdot$ m^{-2}s^{-1}) of A with respect to the surface are given by:

$$\nu_{on} = k_{on}[A]\sigma_{lim}\left(1 - \xi\right) \tag{2.1a}$$

$$\nu_{off} = k_{off}\sigma_{lim}\xi \tag{2.1b}$$

where k$_{on}$ (units: M^{-1}s^{-1}) and k$_{off}$ (units: s^{-1}) represent, respectively, the adsorption and desorption rate constants, and quantify the rate of reaction towards the products and the reagents, σ_{lim} (units: moles $\cdot$ m^{-2}) is the surface density of binding sites, depending on the concentration of ligands, and ξ is the adimensional fraction of surface covered with bound analytes.

When the equilibrium regime is reached, [A]→[A]$_{eq}$ and adsorption and desorption events dynamically balance each other, therefore, by equating 2.1a and 2.1b, it is possible to obtain for equilibrium fractional surface coverage ξ_{eq} with an expression of what is known as the Langmuir adsorption isotherm:

$$\frac{1}{\xi_{eq}} = 1 + \frac{K}{[A]_{eq}} \tag{2.2a}$$

$$\xi_{eq} = \frac{[A]_{eq}}{[A]_{eq} + K} \tag{2.2b}$$

In the formulas the *dissociation constant* $K = \frac{k_{off}}{k_{on}}$ (units: M) has been introduced, the binding surface is assumed homogeneous and all single binding processes must happen independently. From this expression it is already clear

that the detectable concentration range for analyte A when measurements are carried out in equilibrium conditions strongly depends on the dissociation constant K which determines $\xi_{eq}(K)$.
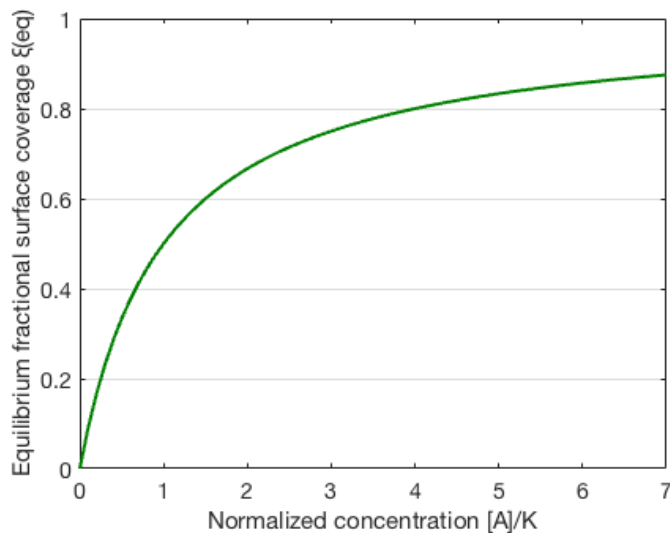
Figure 2.1: Equilibrium surface coverage as a function of normalized analyte concentration $[A]/K$ for adsorption site-limited model.

In the case of *adsorption site-limited model* [A] is more than sufficient to cover all the binding sites and according to Equation 2.2 when $[A]_{eq} \gg K$ $\xi_{eq} \to 1$, equilibrium can be reached and the upper concentration limit is determined by K. Indeed, as shown in Figure 2.1, the fractional surface coverage is brought to saturation conditions when analyte concentration largely exceeds K, which means, in biosensing applications, that these high concentrations cannot be distinguished from one another. Choosing binding reagents with higher dissociation constant could seem a solution to the problem, however this would in turn become detrimental for the detection of lower concentrations, because a smaller number of analytes would be bound to the surface at equilibrium. In the end, the lower limit of detection (LOD) depends on both the sensitivity of the detection technique and on equilibrium surface coverage. Typical values of

K $(10^{-6} - 10^{-9})$ would suggest that for immunosensor applications based on surface coverage measurement, in which [A] is kept below K, allowed analyte concentration detection can fall as low as pM range, provided the sensitivity is high enough.

However, unless the binding protocol implies a continuous flux of A onto the surface, such that the solution is continuously replenished with unbound analytes, it is not correct to consider [A] constant in time, because the initial solution is gradually depleted in analyte concentration as multiple binding events take place at the surface. If $\sigma_{lim} S \xi$ moles of A contained in a volume V (L) bind onto an area S (m^2) in order to reach a concentration of $[A]_{eq}$, the depletion of [A] is given by $\frac{\xi \sigma_{lim} S}{V}$ and the initial and final equilibrium concentrations are related as follows:

$$[A]_0 = [A]_{eq} \left(1 + \frac{\sigma_{lim} S}{V[A]_{eq} + VK} \right) \tag{2.3}$$

From this relation, it is possible to observe that the Langmuir equilibrium treatment of Equation 2.2, which assumes [A] is constant in time, is only applicable when $\sigma_{lim} \frac{S}{V} \ll [A]_{eq} + K$ is satisfied. The difference between initial and final analyte concentrations starts to become significant only at low concentration values and for small K. Since for immunosensing methods $[A] \leq K$, the constraint can become $\sigma_{lim} \frac{S}{V} \ll K$.

We can make some simple practical estimates on the validity of the inequality mentioned above by observing that the sample volume for the considered applications will be of the order of 100 μL and an approximate area $S \sim mm^2$ is usually compatible with optical sensing. As regards surface density of binding sites σ_{lim}, the molecular weight of the typical binding site is around $50 \cdot 10^3 - 100 \cdot 10^3$ Da [54]. If the geometry of the binding sites is modeled as close packing of spheres, a radius r of about 3 nm can estimated, and $\sigma_{lim} = \left(N_A \sqrt{3} r^2 \right)^{-1} \sim 10^{-7}$ moles·m^{-2}. This gives $\sigma_{lim} \frac{S}{V} \sim 10^{-9}$ M. Now, because it was stated above that K determines the upper concentration limit,

and the Langmuir treatment implies $\sigma_{lim}\frac{S}{V} \ll K$, in light of the obtained estimate for $\sigma_{lim}\frac{S}{V}$, it appears evident that detection can still be successfully achieved for concentrations equal or higher than tens of nM, but below these values the assay becomes tricky unless equilibrium fractional surface coverage is kept very low: by inserting the constraint $K \gg 10^{-9}$ M into Equation 2.2 (a K a couple of orders of magnitude larger than 1 nM is assumed), $\xi_{eq} \leq 10^{-4}$ is obtained for $[A] \sim 10^{-11}$ M.
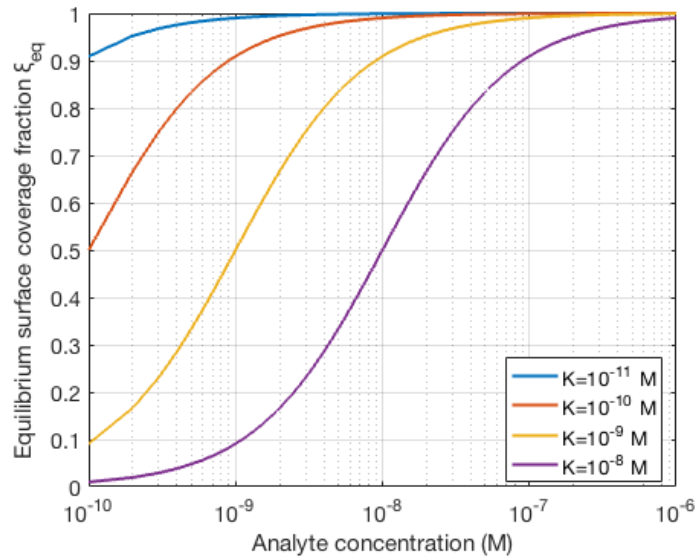
Figure 2.2: Behaviour of the fractional surface coverage as a function of analyte concentration. Different curves for different values of the dissociation constant are shown.

Therefore, in the assumption that the signal output of the biosensor is proportional to the surface occupied fraction, if the the detection method allows for recognition down to certain equilibrium surface coverage fraction ξ_{eq}, which is known, it is possible, given a certain dissociation constant K, to calculate the minimum detectable concentration $[A]$ at equilibrium from Equation 2.2. Otherwise, for a given small analyte concentration $[A]$, biological species with a certain K must be chosen such that the obtained ξ_{eq} lies above the

lowest detectable limit for equilibrium fractional surface coverage determined by the sensitivity of the method. However, as already mentioned, going for a dissociation constant that is too small with respect to the analyte concentration implies that biorecognition signals coming from different high concentration values cannot be distinguished anymore (see Figure 2.2). This means that the value of K and the concentrations to be recognized must be chosen carefully according to the sensitivity of the method and to the above considerations.

In case the total amount of analyte in the solution is less than what is required to completely cover the surface and obtain $\xi = 1$ (*analyte concentration-limited regime*), then $[A]_0 V < \sigma_{lim} S$, equilibrium cannot be reached and for $[A]_0 \gg K$ all analytes will experience binding onto the surface, even for small concentrations, until the solution is completely depleted in $[A]$, and the final surface coverage at the end of the reaction is

$$\xi_{final} = \frac{[A]_0 V}{S \sigma_{lim}} < 1 \tag{2.4}$$

In this case the upper concentration limit for immunosensor detection is given by the inequality $[A]_0 V < \sigma_{lim} S$, and considering the previously computed estimate $\sigma_{lim} \frac{S}{V} \sim 10^{-9}$ M, $[A]_0 \leq 10^{-9}$ M is obtained. The lower limit is once again determined by the sensitivity of the method. If $[A]_0 \ll K$, instead, dissociation events will limit the maximum number of analytes bound to the surface, but $[A]$ in this case is so small that the number of binding events is very small and can hardly be detected, unless very high sensitivity is possible.

2.1.2 Kinetic analysis

Kinetic considerations about the binding event are fundamental in order to determine the time required to reach the equilibrium conditions described above. The reaction involves adsorption and desorption rate processes: these are dynamically related to one another and also coupled to mass transport

phenomena. The latter can be introduced in the system to model the migration of analytes towards the coated surface. Diffusion is the main phenomenon that plays a role in this scheme.

2.1.2.1 Fast analyte diffusion

We shall consider the simplest case where the recognition process is slow compared to the analyte diffusion in solution, and the number of dispensed analytes is large enough to consider their concentration [A] constant. In this case the adsorption rate equation expressed in terms of the time variation of surface coverage can be written as

$$\frac{d\sigma(t)}{dt} = k_{on}[A]\left(\sigma_{lim} - \sigma(t)\right) - k_{off}\sigma(t) \tag{2.5}$$

Because in this regime [A] has been assumed constant, assuming a surface coverage fraction described by the Langmuir isotherm in Equation 2.2, this relation in its integrated form is:

$$\frac{\sigma(t)}{\sigma_{eq}} = 1 - e^{[-k_{on}([A]+K)t]} = 1 - e^{[-t/\tau]} \tag{2.6}$$

where $\sigma_{eq} = \xi_{eq}\sigma_{lim}$ has been used, and where τ is the time constant for the adsorption defined as

$$\tau = \frac{1}{k_{on}\left([A] + K\right)} = \frac{1}{k_{on}[A] + k_{off}} = \frac{t_d}{1 + [A]/K} \tag{2.7}$$

where $t_d = 1/k_{off}$ is the desorption time. This equation clearly shows that the adsorption kinetics from dilute solutions is controlled by the desorption time. The plot in Figure 2.3 shows the time dynamics of normalized fractional surface coverage for different analyte concentrations. Changing [A] means changing the time constant within the exponential, thus modifying the binding velocity, and also, from Equation 2.2, the final ξ reached at equilibrium.

At low concentrations the adsorption time constant is dominated by the desorption rate, whilst it is dominated by the adsorption rate at high concentrations. The transition corresponds to a concentration of K (see Figure 2.3),
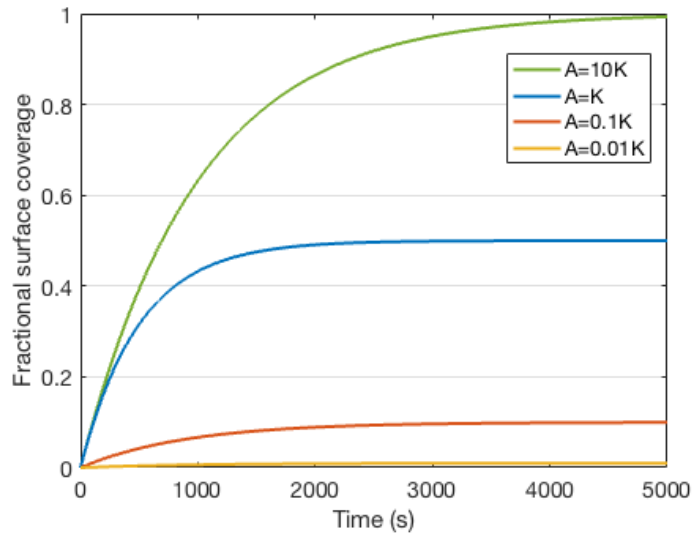
Figure 2.3: Binding curves for different analyte concentrations. Lower concentration means slower exponential increase and lower final covered area from Equation 2.6.

in which case equilibrium fractional surface coverage is equal to 0.5. At low bulk concentrations ($[A] \ll K$), from Equation 2.2 we have that $\xi_{eq} = [A]/K$, thus:

$$\sigma_{eq} = \xi_{eq}\sigma_{lim} = \frac{[A]}{K}\sigma_{lim} \tag{2.8}$$

and from Equation 2.6 the surface concentration of bound species is given by:

$$\sigma(t) = \sigma_{eq}\left[1 - e^{(-t/t_d)}\right] \tag{2.9}$$

At short times, the linearization of the exponential terms leads to a surface coverage that is directly proportional to time:

$$\sigma(t) = \sigma_{eq}\frac{t}{t_d} \tag{2.10}$$

2.1.3 Slow analyte diffusion

When the rate of adsorption is fast compared to the time scale of diffusion, it is necessary to take into account mass transport properties, which determine the travelling dynamics of analytes in solution migrating towards the reactive

surface. To know the case in which we operate, we can define a diffusion time $t_{diff} = \frac{\delta^2}{D}$, where δ is the diffusion layer thickness and D the diffusion coefficient ($\mathrm{m^2 s^{-1}}$). The diffusion layer thickness varies with time in unstirred solutions, but can be fixed by controlling the hydrodynamics (e.g. flow cells).

Mass transport can be described by Fick's second law on linear diffusion from a chamber of a given thickness:

$$\frac{\partial [A]}{\partial t} = D \frac{\partial^2 [A]}{\partial x^2} \tag{2.11}$$

The variation of the surface concentration of the target species with time is equal to the flux of arrival at the surface Φ_s:

$$\Phi_s(t) = D \left(\frac{\partial [A]}{\partial x} \right)_{x=0} = \frac{d\sigma(t)}{dt} \tag{2.12}$$

Surface coverage density $\sigma(t)$ as a function of time is provided by integration of Φ_s:

$$\sigma(t) = \int_0^t \Phi_s dt = \int_0^t D \left(\frac{\partial [A]}{\partial x} \right)_{x=0} dt \tag{2.13}$$

Unfortunately, these equations cannot be solved analytically in the general case, but specific solutions can be obtained for example assuming that the diffusion process is steady-state.

To be able to treat kinetic and mass transport, we shall use the two-layer model, where we define a volumetric surface concentration $[A]_{surf}$ that differs from the bulk value $[A]_{bulk}$, such that the diffusion flux is driven by the gradient $([A]_{surf} - [A]_{bulk})/\delta$.

We start considering a situation with negligible number of occupied sites, i.e. the shortest times characterized by $\xi \ll \xi_{eq}$ for all values of $[A]/K$. In this case, Equation 2.5 reduces to

$$\frac{d\sigma(t)}{dt} = k_{on}[A]_{surf}\sigma_{lim} \tag{2.14}$$

Moreover, if the diffusion layer thickness is steady-state, e.g a well-stirred system or a spot in a protein array, then:

$$\frac{d\sigma(t)}{dt} = k_{on}[A]_{surf}\sigma_{lim} = \Phi_s(t) = \frac{D}{\delta}([A]_{bulk} - [A]_{surf}) \qquad (2.15)$$

Therefore, the volumetric surface concentration can be computed as

$$[A]_{surf} = \frac{D[A]_{bulk}}{k_{on}\sigma_{lim}\delta + D} \qquad (2.16)$$

This results, for $[A] \ll K$, in the surface concentration increasing linearly with time

$$\sigma(t) = \left(\frac{k_{on}[A]_{bulk}\sigma_{lim}}{1 + \frac{k_{on}\sigma_{lim}\delta}{D}}\right) t = \left(\frac{\sigma_{eq}}{1 + Da}\right)\frac{t}{t_d} \qquad (2.17)$$

When D is very large, Equation 2.17 tends to Equation 2.10. We can see that when the diffusion layer thicknesses are thin or for large values of D (i.e. small molecules) then the mass transfer is very fast. The dimensionless ratio $\frac{k_{on}\sigma_{lim}\delta}{D}$ is called the Damköhler number, Da, and represents the ratio between the adsorption rate and the diffusion rate, both expressed in $m^2 s^{-1}$ [55]. When $Da \gg 1$, diffusion plays an important role and we have a pure diffusion control:

$$\sigma(t) = \frac{D[A]_{bulk}}{\delta}t \qquad (2.18)$$

while for $Da \ll 1$ Equation 2.10 is recovered.

Generally speaking, it is not possible to solve the time dependence of an adsorption-diffusion process. Anyway, to a first approximation the diffusion layer thickness in Equation 2.17 can be assumed to grow with time according to $\delta = \sqrt{2Dt}$ (Einstein's equation). We use this expression in Equation 2.17.

In Figure 2.4 surface concentration-time plots are reported showing the influence of the diffusion in stirred and unstirred solutions. The blue curve represents the ideal stirring condition where the volumetric surface concentration is always equal to the bulk concentration. In this case, the adsorption is limited by the kinetics of the binding reaction (Equation 2.6). The dashed line
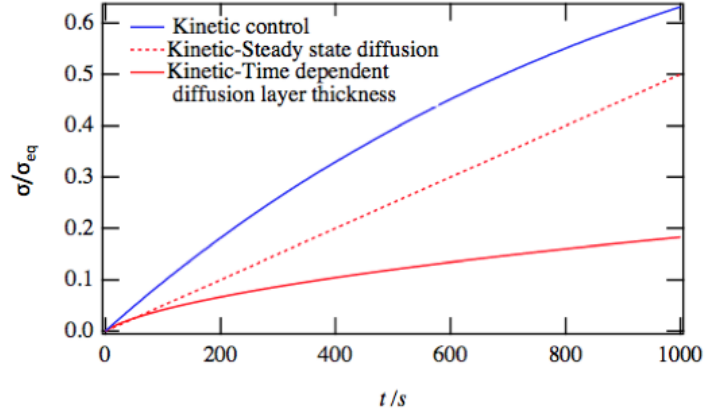
Figure 2.4: Time variation of the surface concentration $\sigma(t)$ for different contributions of diffusional mass transport: $Da \ll 1$ (solid, blue), $Da = 1$ (dashed, red), $Da \gg 1$ (solid, red) ($k_{on} = 10^4$ M^{-1}s^{-1}, $K = 10^{-8}$ M, $\sigma_{lim} = 10^{-7}$ moles·m^{-2}, $D = 10^{-8}$ m^{2}s^{-1}, $\delta = 10^{-8}$ m, $[A] = 10^{-10}$ M).

represents a stirring condition that fixes the diffusion layer thickness such that $Da = 1$, thus the slope from Equation 2.17 is equal to half that of the initial tangent of the top curve. In this case, the adsorption process is controlled both by kinetics and diffusion. The bottom curve represents a non-stirred system where the diffusion layer thickness in Equation 2.17 grows with square root of time. We see that stirring only plays a role after 1 minute. Indeed, at short times the transient Damköhler number (proportional to $\sqrt{t}$) is small.

After these shortest times, the surface concentration and the volumetric surface concentration both vary with time in conjunction with the flux of oncoming target species [56]:

$$\frac{d\sigma(t)}{dt} + z\frac{d[A]_{surf}(t)}{dt} = \Phi_s(t) = \frac{D}{\delta}([A]_{bulk} - [A]_{surf}) \qquad (2.19)$$

$$\frac{d\sigma(t)}{dt}\left(1 + \frac{zK}{\sigma_{lim}}\right) = \Phi_s(t) = \frac{D}{\delta}([A]_{bulk} - [A]_{surf}) \qquad (2.20)$$

where z represents the arbitrary thickness of the volumetric surface layer (see Figure 2.5) and it has been assumed that $[A] \ll K$ and that $[A]_{surf}$ is the
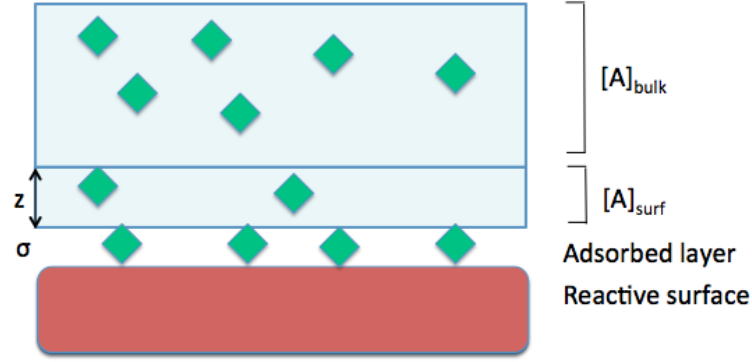
Figure 2.5: Schematic of the system comprising a distinct bulk and surface concentrations. The surface concentration, which varies with time, is assumed to extend up to a distance corresponding to the diffusion layer thickness z.

equilibrium concentration from the Langmuir isotherm. After a few calculations [57], the solution can be found:

$$\sigma(t) = \sigma_{eq} \left[1 - e^{-\frac{KDt}{\delta(Kz + \sigma_{lim})}} \right] \tag{2.21}$$

The latter equation describes the kinetic of surface adsorption under steady-state diffusion control. Now, again we can apply the perturbation approach and introduce a time dependent diffusion layer thickness $\delta = \sqrt{2Dt}$ to obtain:

$$\sigma(t) = \sigma_{eq} \left[1 - e^{\left[-\left(\frac{K\sqrt{D/2t}}{\sigma_{lim}} \right) t \right]} \right] \tag{2.22}$$

For the linearized Langmuir isotherm (Equation 2.8), the exact time dependence of the surface concentration can be obtained analytically solving Fick's equation with Laplace transforms [58], obtaining:

$$\sigma(t) = \sigma_{eq} \left[1 - e^{\frac{K^2 Dt}{\sigma_{lim}^2}} erfc \left(\frac{\sqrt{KDt}}{\sigma_{lim}} \right) \right] \tag{2.23}$$

Figure 2.6 shows a comparison between the trends of the kinetic steady state diffusion (Equation 2.23), the diffusion-controlled reaction (Equation 2.21) and the solution to the perturbation approach for the time dependent diffusion layer (Equation 2.22).
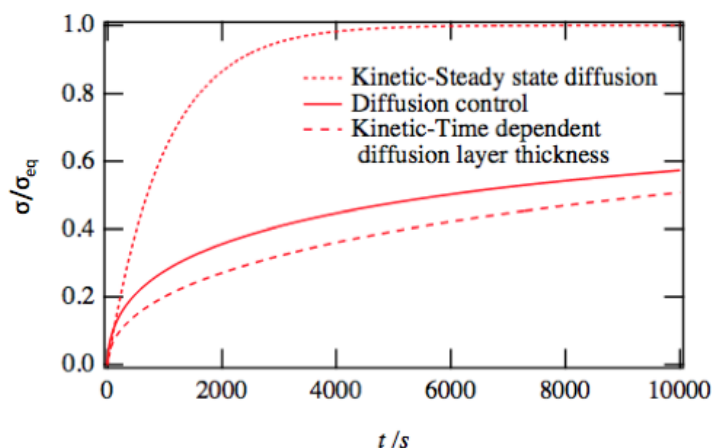
Figure 2.6: Comparison between stirred and unstirred diffusion controlled reactions ($k_{on} = 10^4$ M^{-1}s^{-1}, $K = 10^{-8}$ M, $\sigma_{lim} = 10^{-7}$ moles·m^{-2}, $D = 10^{-8}$ m^{2}s^{-1}, $\delta = 10^{-8}$ m, $[A] = 10^{-10}$ M)

In the analytical experiments carried out in this thesis, and in the following data interpretation, we assumed that biorecognition assays (carried out statically) are always only limited by the kinetics of the reaction for simplicity. However in the case of microfluidically stirred systems more detailed computational analyses on the mass transport regime (with its diffusion layer thickness, Damköhler number etc.) and type of flow (laminar or turbulent) would be required.

It is important to underline the role of the dissociation constant K in determining response times: as seen in Section 2.1.1, while higher dissociation constants may be preferred to avoid saturation of the reaction and, as a consequence, of the biodetection, they also imply higher response times, increasing the duration of the whole process. For lower concentrations lower K is preferred for suitable detection, but in these cases, for a given K, the concentrations to

recognize can be so low that response times are often long. Therefore, higher sensitivity and better limit of detection can be achieved only at expenses of the duration of the assay.

These considerations are to be assumed valid also for the labelling step, i.e. when magnetic particles bind to target molecules which lie on the sensor surface. The reaction leading to the final bound state requires magnetic markers to be coated with a layer of streptavidin, which non-covalently binds to biotin, a molecule DNA strands or the p24 antigens are previously functionalized with. The biotin-streptavidin bond is characterized by a dissociation constant as low as $K \sim 10^{-14}$ M. Since during labelling phase magnetic markers are injected onto the sensitive surface in a solution with very high concentration with respect to the number of active sites on the sensor, saturation of the binding sites is easily reached (provided steric hindrances given by the functionalized markers' geometry do not constitute a serious limitation). The utilized passive labels in bio-optical assays are magnetic nanoparticles of 150 nm diameter and $2.9 \cdot 10^{-18}$ kg mass, and diffusion should be considered as a limiting factor in the kinetics because such particles are much bigger than target analytes. However, hybridization was performed with a highly saturated beads solution in static conditions, by injecting a drop of solution onto the sensor surface and letting the system evolve freely. By adopting the binding site-limited model approach it is possible estimate the binding time by computing the time constant in the exponential of Equation 2.6: if the adsorption rate constant is taken to be $k_{on} \sim 10^5$ M^{-1}s^{-1} [59], and the dispensed beads solution concentration around 10^{-7} M, a time constant of around 10^2 s is obtained. This value has to be considered an underestimation of the effective overall binding time, because its computation disregards both diffusional transport limitations and the fact that the effective dissociation constant K between biotin and streptavidin is

expected to be larger when the latter (a few nanometers in size, like most proteins) is attached to massive particles (150 nm in diameter).

A more detailed discussion of this theoretical model applied to our specific case is presented in Chapter 4.

2.2 Integrated guided optics

Integrated optics is an emerging technology that consists on building on the same substrate (often a chip) devices and components meant to generate (laser, LED), manipulate (modulators, commutators, polarizers, filters, couplers, etc.) and detect (photodiodes, phototransistors) optical signals. Optical biosensors offer great advantages over conventional analytical techniques because they enable the direct, real-time and label-free detection of many biological and chemical substances. Their advantages include high specificity, sensitivity, small size and cost-effectiveness.

2.2.1 Optical waveguides

An optical waveguide is a structure meant to drive light, i.e. electromagnetic waves, along a determined path with the smallest possible attenuation. It can commonly consist of a slab, a stripe, or a cylinder made of transparent dielectric material with refractive index n_1 embodied in a second dielectric structure with refractive index $n_2 < n_1$. Light confinement is accomplished, in all significant cases for applications, via total internal reflection (coming from Snell's law for $\theta_i > \theta_{crit}$ at the interface between the two dielectric media).

Important parameters to take into account for waveguide optimization are geometry, wavelength and initial field distribution, material data, and electrooptic driving conditions. Common waveguides include Semiconductor
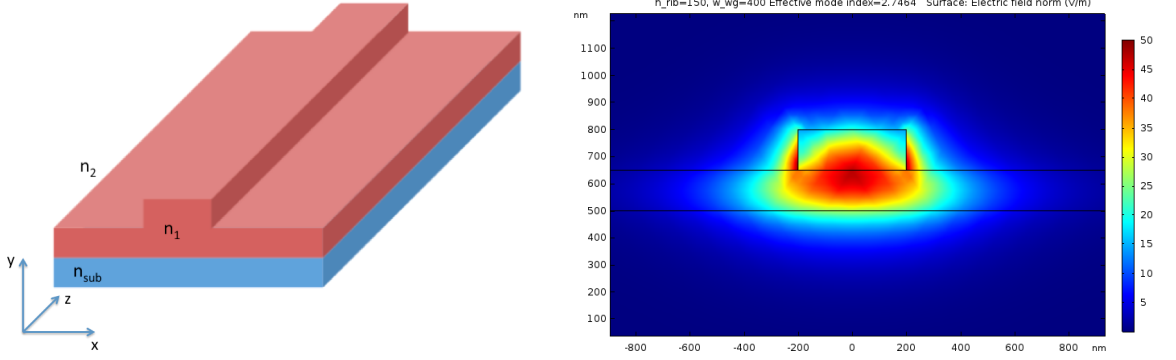
Figure 2.7: Example of a rib-shaped optical waveguide. For biosensing purposes it is appropriate to suitably expose the waveguide, therefore usually $n_2 \neq n_{sub}$, though still both are smaller than n_1. On the right the electrical normalized field intensity of the fundamental quasi-TE mode of the waveguide is represented.

waveguides (GaAs, InP, etc.), Electro-Optic waveguides (mostly LiNbO$_3$), glass waveguides (silica, SiON), and polymer waveguides.

In this work, silicon-on-insulator rib-shaped rectangular waveguides are used (see Figure 2.7). Core waveguide layer is made of Si (n$_1$ = 3.475 for $\lambda = 1550$ nm that will be exploited for our purposes). A silica layer under the core layer is used for lower cladding, and air on top acts as the top cladding layer. This structure allows tightly confined waveguide mode because of large index difference.

An optical mode is solution of Maxwell's equations satisfying all boundary conditions (tangential component of E and H be continuous across both interfaces). Its spatial distribution does not change with propagation. For waves modeled as complex exponentials $e^{-i\omega t}$, modes are obtained by solving the curl equations:

$$\nabla \times \mathbf{E} = i\omega\mu_0\mathbf{H} \tag{2.24a}$$

$$\nabla \times \mathbf{H} = -i\omega\epsilon_0 n^2\mathbf{E} \tag{2.24b}$$

These equations have two distinct sets of linearly polarized solutions: Transverse-Electric (TE) and Transverse-Magnetic (TM) modes.

In order to determine the transversal field distribution of the modes within the guide, it is necessary to analyze the problem inside and outside the guiding layer separately [60]. The internal field roughly consists, because of the total internal reflection phenomenon, of the superposition of two plane waves propagating at $\pm\theta_m$ with respect to the longitudinal z-axis, where m is the mode index. If we sum the two complex fields which represent the mentioned plane waves, which are $m\pi$-dephased with respect to one another on a generic transversal plane, we obtain the spatial amplitude for the transversal field:

$$E_x(y,z) \propto U_m(y)e^{-i\beta_m z} \tag{2.25}$$

where $\beta_m = k_{zm} = nk\cos\theta_m$, and U_m has the following form:

$$U_m(y) \propto \cos\frac{2\pi n_1 \sin\theta_m}{\lambda}y \qquad \text{for } m = 0,2,4,... \tag{2.26a}$$

$$U_m(y) \propto \sin\frac{2\pi n_1 \sin\theta_m}{\lambda}y \qquad \text{for } m = 1,3,5,... \tag{2.26b}$$

Outside the guiding layer, the field $E_x(y,z)$ must satisfy Helmholtz's equation:

$$(\nabla^2 + n_2^2 k^2)E_x(y,z) = 0 \tag{2.27}$$

But because boundary conditions impose the continuity of the tangential component of E, then Equation 2.27 must apply to the field in Equation 2.25 also at the boundary (i.e. for $y = \pm d/2$, with d transversal dimension of the guiding layer), giving:

$$\frac{d^2 U_m}{dy^2} - \gamma_m^2 U_m = 0 \tag{2.28}$$

where $\gamma_m^2 = \beta_m^2 - n_2^2 k^2$. The allowed values for θ_m and $\beta_m(\theta_m)$ can be computed from self-consistency conditions of the field in the waveguide, and it turns out that $\gamma_m > 0$, thus the solution to the constant coefficients-differential equation derived above consists of two real exponentials, $e^{-\gamma_m y}$ for $y = d/2$ and $e^{\gamma_m y}$
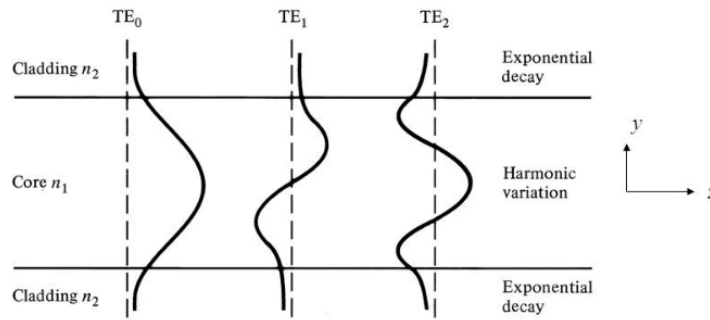
Figure 2.8: TE modes propagating inside a waveguide: they combine sinusoidal behaviour near the center of the core layer with exponential decay right beyond the interfaces with the non-guiding layer.

for $y = -d/2$. The field is exponentially attenuated with increasing y in the non-guiding layer (see Figure 2.8). γ_m is called *extinction coefficient* and the resulting wave is an evanescent wave, with no power flux associated to it along the y-direction in the non-guiding layer.

2.2.2 Microring resonators

An optical cavity, also called optical resonator, is a device that is able to confine light at a certain frequency within a defined volume. Electromagnetic waves can exist inside in the form of stationary waves which are null at the interfaces, and multiple configurations for the stationary waves, i.e. multiple modes, can be possible. Thanks to their sensitivity to light frequency, optical resonators are used as spectrum analyzers or as optical filters. They are typically implemented with a design that allows a high Q-factor, so that the light beam can be reflected many times with low attenuation, and the resonance is very narrow. The use of silicon for fabricating these devices allows for very small sizes, great compactness and large free spectral range.
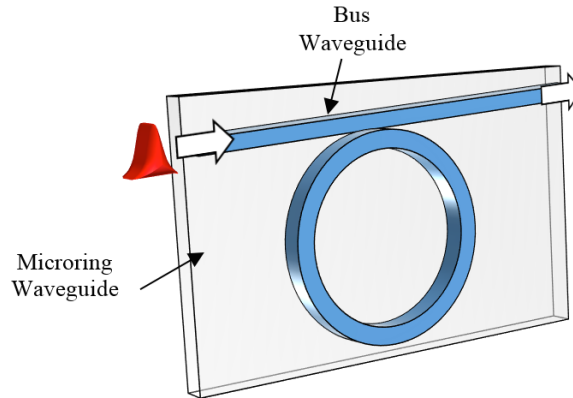
Figure 2.9: Looks of an all-pass ring resonator.

A particularly interesting geometry is the micro-ring resonator, which is a looped optical waveguide such that resonance occurs when the optical path around the whole ring corresponds to an integer multiple of the wavelength, therefore many resonances are possible. In order to access the loop, and to make micro-ring resonators useful in practical applications, some coupling mechanism is required, usually a bus guide placed in close proximity, at a distance smaller than the radiation wavelength: in such a way, the evanescent field of light injected in the bus from one side couples to the ring, and the transmitted signal is acquired from the other side. This configuration corresponds to an all-pass filter (APF) (see Figure 2.9) or notch-filter, and is the simplest form of a micro-ring resonator[1].

When the waves in the loop complete a round trip around the ring, they accumulate a phase of 2π, interfere constructively and the cavity is in resonance. In other words, the wavelength of the light must fit an integer number of times

---

[1]As described in Chapter 3, the used micro-rings in our case are actually in the add-drop configuration, with two bus lines coupled to the ring. However only the all-pass port was used, so the theoretical overview is limited to APFs for the sake of simplicity.
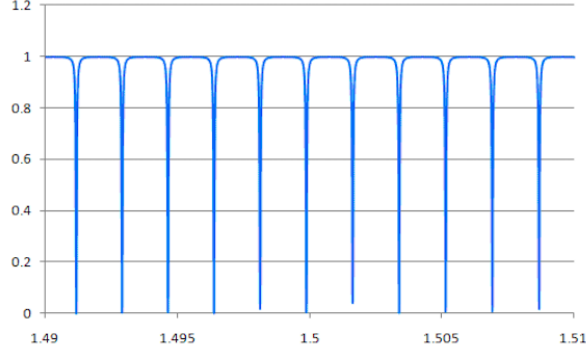
Figure 2.10: Transmission spectrum of a typical ring coupler.

inside the optical length of the ring L:

$$\phi_{res} = 2m\pi \qquad\qquad \text{m=1, 2, 3, ...} \qquad\qquad (2.29a)$$

$$\lambda_{res} = \frac{n_{eff}L}{m} \qquad\qquad\qquad\qquad (2.29b)$$

After a certain number of loops, however, the accumulated phase shift produces destructive interference with the radiation in the coupler, thus notches appear in the transmission power spectrum of the structure for certain wavelengths (see Figure 2.10).

Let's now mention a few important parameters characterizing a resonator. An important spectral property of this system is the intensity transmission, i.e. the ratio between transmitted and injected intensities in the bus.

$$T_{notch} = \frac{I_{pass}}{I_{input}} = \frac{a^2 - 2ra\cos\phi + r^2}{1 - 2ra\cos\phi + r^2a^2} \qquad\qquad (2.30)$$

In this equation, $\phi = \beta L$ is the single-pass phase shift, for a given L length of a round trip and β propagation constant of the circulating mode; a represents the single-pass amplitude transmission and includes losses in the ring and in the coupler; r indicates the self-coupling coefficient, representing the fraction of radiation travelling in the bus only. If cross-coupling coefficient k is introduced, the squares of the coupling coefficients represent the power splitting ratios of

the coupler and the relation $r^2 + k^2 = 1$ is assumed to be valid, meaning there are no losses in the coupling section.

For ideal cavities with zero attenuation $a \approx 1$, so $T_{notch} = 1 \; \forall \phi$. Instead, when the coupled power is equal to the power loss inside the ring, $1 - a^2 = k^2$ or $r = a$, and at resonance $T_{notch} = 0$. Even out of this critical coupling condition, a strong reduction of the transmitted intensity is expected at resonance, which is why the characteristic notch shape is generated.

The full width at half maximum (FWHM) of the resonance spectrum is another important characteristic of the resonators, and it can be derived from Equation 2.30:

$$FWHM = \frac{(1 - ra)\lambda_{res}^2}{\pi n_g L \sqrt{ra}} \tag{2.31}$$

By considering an approximation for dispersion up to first order, the free spectral range, i.e. the wavelength range between two consecutive resonances, is given by the following relation:

$$FSR = \frac{\lambda^2}{n_g L} \tag{2.32}$$

n_g being the group index, which accounts for the dispersion of the waveguide, a phenomenon describing the envelope of a propagating pulse travelling through a dispersive medium. It is given by

$$n_g = n_{eff} - \lambda_0 \frac{dn_{eff}}{d\lambda} \tag{2.33}$$

Micro-rings are single-mode waveguides, which makes it easier to produce large free-spectral range with tunable lasers.

The finesse is a measure of the sharpness of resonances with respect to their spacing, and it is expressed by the ratio of the FSR and resonance width:

$$Finesse = \frac{FSR}{FWHM} \tag{2.34}$$

It represents, within a factor of 2π, the number of round-trips light has travelled inside the ring before its energy falls down to $1/e$ of its initial value.

Finally, the quality factor (Q factor) quantifies the sharpness of the resonance relative to its central frequency:

$$Q = \frac{\lambda_{res}}{FWHM} \tag{2.35}$$

It indicates the number of oscillations of the field before the circulating energy becomes to $1/e$ of the initial one.

A complete description of the physics of micro-ring resonators, their geometries, spectral characteristics, losses, coupling and sensitivity can be found in [61].

2.3 Magnetic aspects

This section describes in detail the physical behaviour of magnetic nanoparticles, their magnetic features and frequency-dependent dynamics, in order to shed light on the interesting features which are often exploited in sensing applications, especially biological ones, due for example to the stability of their magnetic properties and the possibility to easily manipulate them through suitably applied forces.

2.3.1 Superparamagnetism

Superparamagnetism (SPM) is a type of magnetism that occurs in small ferromagnetic or ferrimagnetic nanoparticles, which are usually, because of their size, in a single-domain configuration. The total magnetic moment of a nanoparticle, to a first approximation, is composed of all the magnetic moments of the atoms forming it. The collinearity of the spins can be maintained only over a certain length, which depends on the material (e.g. around 80 nm for Fe_3O_4 particles and 90 nm for Fe_2O_3 particles [62]). For spherical particles,

this size limit can be approximated by [63]:

$$R = 9\frac{\sqrt{AK}}{\mu_0 M_s^2} \tag{2.36}$$

Where A indicates the exchange stiffness, K is the magnetic anisotropy constant, μ_0 is the permeability of free space, i.e. $4\pi\cdot10^{-7}$ H/m, M_s is the saturation magnetization. Single-domain particles are magnetically saturated because all the magnetic moments are aligned with or without an external magnetic field. This determines the maximum correlation distance between spins, and therefore the size of a domain. If the size of the system is bigger than this critical size, it is a bulk material and a multi-domain configuration is expected, whereas single domains are necessarily formed in nanoparticles.

Bulk particles and nanoparticles behave differently in presence of a magnetic field: single-domain nanoparticles show spin rotation, bulk particles display a movement of the domain walls according to the amplitude and direction of the field, as shown in Figure 2.11.
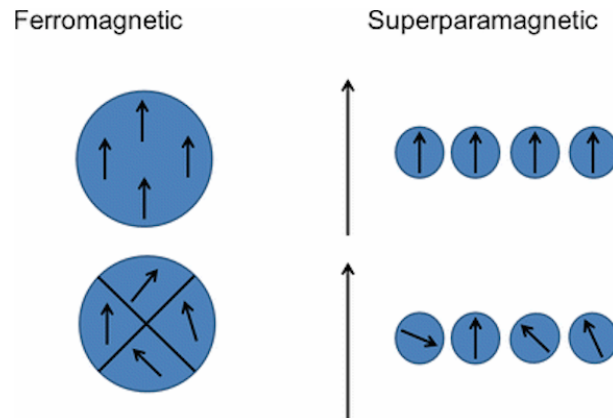
Figure 2.11: In an external magnetic field, multi-domain bulk particles are purely ferromagnetic and respond via domain wall movement and domain rotation, generating the well-known characteristic hysteresis loop; single-domain magnetic nanoparticles simply orient their moments along the field.

Let's consider a magnetic particle of volume V, whose size is small up to a point such that it is a single magnetic domain, with magnetocrystalline or

shape anisotropy described by an energy density term:

$$E = K sin^2\theta \tag{2.37}$$

Where K defines the magnetic anisotropy constant. It follows that in these conditions, assuming uniaxial anisotropy for the particle, only two magnetization configurations are possible, i.e. characterized by a magnetic moment aligned along the axis pointing in two opposite directions with respect to one another. The activation energy required for flipping the magnetization state from the condition $\theta = 0$ to $\theta = \pi$ is $\Delta E = KV$, which depends, beside on the particle dimension, on the anisotropy of the material itself.

If this energy barrier is small compared to k_BT, where k_B is the Boltzmann constant, the direction of the magnetization randomly flips between the two possible states because of thermal fluctuations. For $k_B T \gg KV$ an ensemble of non-interacting magnetic particles will behave as a paramagnet, and after application of a magnetic field the relaxation of the magnetization can be expressed through a characteristic time. The latter corresponds to the average time to perform such a flip and is given by the relaxation time:

$$\tau = \tau_0 exp \left(\frac{KV}{k_B T} \right) \tag{2.38}$$

where τ_0 is a characteristic time length of the probed material, often of a magnitude of around 10^{-9} to 10^{-12} s for non-interacting particles.

A commonly used criterion for blocking is:

$$\frac{KV}{k_B T_B} = 25 \tag{2.39}$$

This corresponds, at a given temperature, to $\tau \approx 100$ s, which lies above the amount of time required for the measurement of a magnetic moment.

T_B, the blocking temperature, is defined as the temperature separating the blocked and the superparamagnetic states.
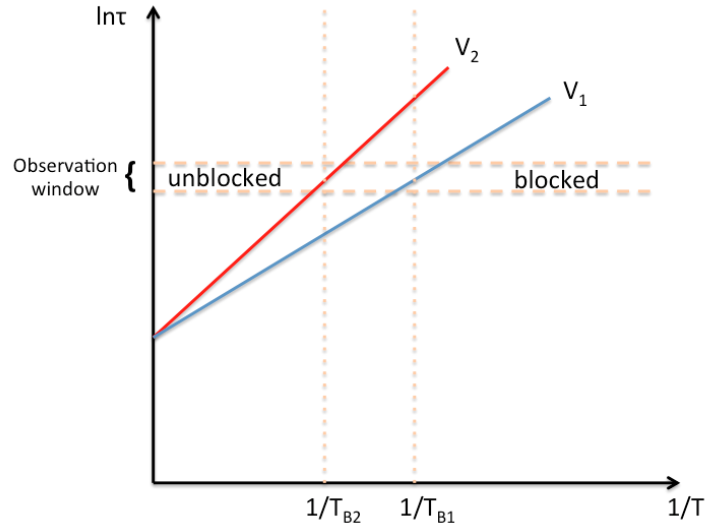
Figure 2.12: Relaxation time τ, logarithmically plotted, for different particle volumes with $V_2 > V_1$. For a given observation window, if $T_{B1} < T < T_{B1}$, V_1 particles will be in the unblocked regime while V_2 particles will be in the blocked one.

The observation of nanoparticles in the superparamagnetic state intrinsically depends, as indicated above, on the temperature and on the height of the energy barrier between states, but it also depends on the characteristic measurement time t_m of the chosen experimental technique: whenever $t_m > \tau$ the measurement actually observes a state which is strongly fluctuating in time, therefore, when no external magnetic field is applied, the measured net magnetic moment is zero, because it represents a time average of the fluctuating states. This situation is called the superparamagnetic state of a system, since, if we consider an ensemble of magnetic nanoparticles, the magnetic moment taken from the ensemble freely and randomly fluctuates when thermally activated, however the single atomic moments retain their ferromagnetic order.

The plot in Figure 2.12 intuitively shows, for a given observation time, the expected state of the system, blocked or unblocked, for different particle volumes V_1 and V_2 with $V_2 > V_1$. Since from Equation 2.38 $\ln \tau = \ln \tau_0 + \frac{KV}{k_B T}$, the energy barrier is proportional to the volume, which determines the slope of

the straight line. Therefore, if the observation window falls below the line (i.e. the working temperature is $T < T_B$), the particle will appear blocked. Also, if higher working temperatures are needed, the observation window will have to be moved downwards towards shorter time scales because the particle will relax faster. The figure also shows how the particle volume influences the blocking temperature T_B, indeed $T_{B1} < T_{B2}$.

2.3.1.1 Effect of a magnetic field

If we consider magnetic particles of all kinds and sizes, their magnetic behaviour can be classified according to the value of the volumetric susceptibility χ:

- Small χ: when $\chi < 0$ the material is diamagnetic, and the magnetic moments align along a direction opposite to the applied magnetic field; when $\chi > 0$ the material is paramagnetic, there is no remnant ordering of the particles' moments and they align along the direction of the external magnetic field when it is applied.

- Large χ: the material is ferromagnetic, exchange interaction between moments can stabilize single domain configuration. Superparamagmetic regime depends on system dimensions, and it scales with thermal energy and anisotropy constant K.

In the superparamagnetic region the particles can be modeled as Langevin's superparamagnets, each of which has a giant magnetic moment.

Let's now consider the case of a magnetic field H being applied along an arbitrary axis, e.g. the z axis. If we define the adimensional parameter

$$x = \frac{\mu_0 m H}{k_B T} \tag{2.40}$$

which represents the ratio between the Zeeman interaction energy term and the thermal energy term, m being the magnetic moment of a single particle, it
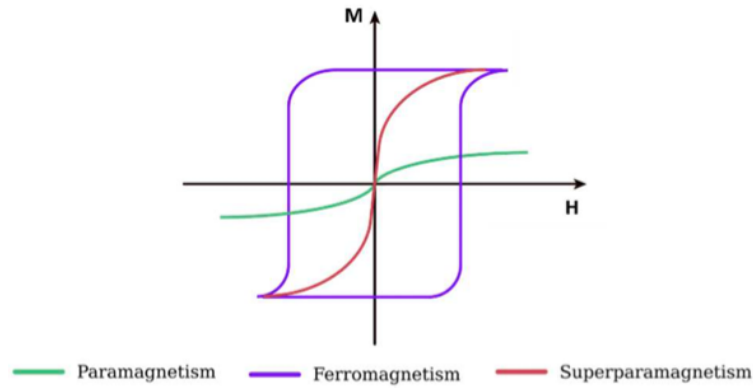
Figure 2.13: Magnetization hysteresis loops for different magnetic materials.

follows that the average component of m along the preferential axis z is given by:

$$< m_z >= mL(x) \tag{2.41}$$

where

$$L(x) = \left(\coth(x) - \frac{1}{x} \right) \tag{2.42}$$

is called the Langevin function.

For low applied magnetic field or at high temperature, this function can be approximated to

$$L(x) \sim x/3 \tag{2.43}$$

So that the magnetic susceptibility of the sistem of particles is:

$$\chi = \frac{n < m_z >}{H} = \frac{\mu_0 n m^2}{3k_B T} \tag{2.44}$$

with $n = $ volume density of particles.

2.3.2 Magnetic beads

The energy barrier ΔE affects the spin reversals and the corresponding relaxation time. Referring to Equation 2.38 for the relaxation time, it is clear

that, because the volume V of the particle is contained in the exponential term, as soon as the nanoparticles become too large, the behaviour of moment flipping ceases to be an interesting aspect and becomes negligible. Therefore there exists a critical diameter for nanosized particles below which the superparamagnetic regime holds. The corresponding volume can be obtained by equating τ in Equation 2.38 to the characteristic measurement time of the considered experimental technique. Nanoparticles in superparamagnetic regime at room temperature are characterized by a significantly reduced critical size, typically ranging from a few nanometers to a few tens of nanometers.

Because they are often used in biological applications, where the particles are in suspension in a liquid solution, the Brownian relaxation motion plays a significant role, whereas the magnetic forces end up being relatively small, so the particles are not easily manipulated with external fields. For this reason, it is very common to choose to use ensembles of superparamagnetic nanoparticles.

Magnetic beads are made of a polymer matrix embodying a core of superparamagnetic particles (see Figure 2.14), usually made of magnetite (Fe_3O_4) or magnemite (Fe_2O_3) having a critical diameter of 30 nm at room temperature. They behave as magnetic cores whose reciprocal interaction is very weak, because of their negligible remanence. The total magnetic moment of a bead corresponds to the sum of the magnetic moments of the nanoparticles contained in the non-magnetic polymer matrix.

Magnetic beads' diameter size can range from a few tens of nanometers to a few microns, and they can be chemically surface-functionalized, which makes them, as already mentioned in Section 1.3.1, a useful instrument for in-vitro diagnostics, high-throughput screening, magnetic bioseparation, cell labeling as well as for research and development of novel diagnosis and therapy methods.
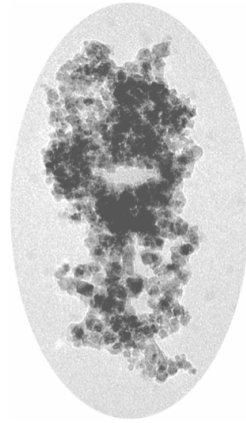
Figure 2.14: TEM image of a section of a bead particle. Magnetite cores consist of aggregates of iron oxide crystals with diameters of a few nanometers and are contained in the dextrane polymer matrix.

2.3.3   Brownian and Néel relaxation

The dynamics of superparamagnetic particles in the presence of an external magnetic field are related to the minimization of the Zeeman magnetic energy, which corresponds to a general tendency displayed by the single-domain magnetic cores to align their magnetic moments in the direction of the field. For this purpose, two competing mechanisms can act in the system:

i) If the particle is free to move, it will rotate in order to reach the minimum energy state as mentioned. This behaviour is called Brownian rotation [64] and it is connected to some anisotropy of the particle leading to a preferential orientation of the magnetization;

ii) If the particles are fixed in space and cannot move, as is the case of individual nanoparticles embodied in the solid polymer matrix of the beads, then it is the magnetic moment of every single nanoparticle the entity that exhibits a rotation in order to align to the external field. This phenomenon is related to the Néel relaxation [65].
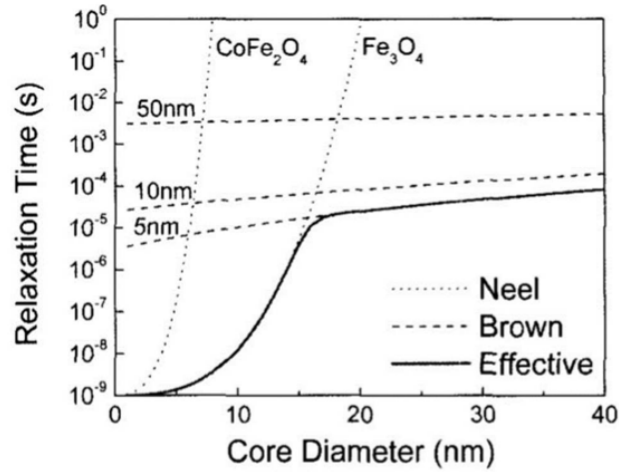
Figure 2.15: Relaxation time trends for Néel (dotted) and Brownian (dashed) rotation phenomena. Néel relaxation is plotted for two different magnetic core materials, while Brownian relaxation in different non-magnetic surfactant thicknesses in liquid solutions is provided. The effective trend for magnetite nanoparticles with surfactant thickness of 5 nm is plotted by the solid line. Adapted from [1].

The competition between these two phenomena in a superparamagnetic system can be quantified, compared and explained by considering the two different relaxation times. The Brownian relaxation time can be expressed as

$$\tau_B = \frac{3\eta V_h}{k_B T} \tag{2.45}$$

where η is the dynamic viscosity of the fluid and V_h the hydrodynamic volume of the particle. The Néel relaxation time τ_N is closely related to the intrinsic behaviour of a superparamagnetic system, and simply corresponds to τ in Equation 2.38.

The combination of the relaxation dynamics involves an effective relaxation time which is mostly influenced by the faster of the two phenomena, therefore it can be written as:

$$\tau_{eff} = \frac{\tau_N \tau_B}{\tau_N + \tau_B} \tag{2.46}$$

Figure 2.15 shows the general trend of relaxation times for different particle diameters and materials. It can be observed that magnetic beads containing magnetite cores are mainly governed by Brownian relaxation, for a size larger than 50 nm.

2.3.4   Frequency behaviour

In the case of a time-dependent external magnetic field applied to an ensemble of magnetic nanoparticles, the behaviour of the system depends on the complex frequency-dependent magnetic susceptibility. From a magnetic model similar to the Debye theory of dipole polarization, it is possible to make a simple description of the phenomenon (a more theoretical treatment of relaxation time and frequency behaviour can be found in [66]).

We begin by expressing the frequency-dependent susceptibility as:

$$\chi(\omega) = \frac{\chi_0 - \chi_\infty}{1 + i\omega\tau} + \chi_\infty \tag{2.47}$$

ω being the angular frequency of the applied field, χ_∞ the high frequency susceptibility and χ_0 the static susceptibility.

If we separate the real and imaginary part of Equation 2.47, we obtain:

$$\chi\left(\omega\right) = \chi\left(\omega\right)' - i\chi\left(\omega\right)'' \tag{2.48}$$

$$\chi\left(\omega\right)' = \frac{\chi_0 - \chi_\infty}{1 + i\left(\omega\tau\right)^2} + \chi_\infty \tag{2.49}$$

$$\chi\left(\omega\right)'' = \frac{\left(\chi_0 - \chi_\infty\right)\omega\tau}{1 + i\left(\omega\tau\right)^2} + \chi_\infty \tag{2.50}$$

The last two expressions define the in-phase and out-of-phase magnetic susceptibility.

As Figure 2.16 shows, we can distinguish three main regimes for the magnetic susceptibility and therefore for the kind of response the particles are able to display in presence of the external field. When the frequency is very low,
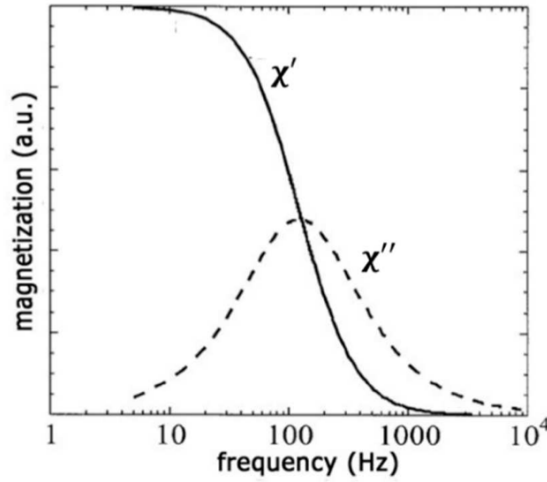
Figure 2.16: Real and imaginary part of the magnetic susceptibility of an ensemble magnetic nanoparticles as a function of the frequency of an AC magnetic field.

close to zero, the field variation is slow enough that the magnetic moments of the particles are able to follow the orientation of the field and $\chi\left(\omega\right)''$ is null. In the high frequency region, the oscillation is so fast that the particles are not able to follow the variations, therefore no response is observed, and both $\chi\left(\omega\right)'$ and $\chi\left(\omega\right)''$ tend to zero. Finally, an intermediate regime is observed, in which the single magnetic moments are able to follow the changes of the field to some extent, although not completely, giving a decrease in $\chi\left(\omega\right)'$ with increasing frequency. The peak observed in the trend of $\chi\left(\omega\right)''$ describes the resonant behaviour occurring when the frequency of the external field matches the relaxation frequency of the dominating relaxation phenomenon. In the case of magnetic beads of average size above 50 nm, the Brownian relaxation plays a significant role, with respect to Néel relaxation, in varying the moments' direction, therefore the peak in $\chi\left(\omega\right)''$ corresponds to the so-called Brownian relaxation frequency, given by

$$f_B = \frac{1}{2\pi\tau_B} = \frac{k_B T}{6\pi\eta V_h} \tag{2.51}$$

2.3.5   Force on magnetic particles

Since many applications in biomedicine require to manipulate the path of magnetic particles, it is important to understand the force required to do so, in its mathematical form and in its value. A uniform magnetic field may give rise to a torque, however it cannot be used to obtain a translational movement, which requires the presence of a gradient. The magnetic force on a point-like magnetic moment $\mathbf{m}$ is given by

$$\mathbf{F} = (\mathbf{m} \cdot \nabla) \, \mathbf{B} \tag{2.52}$$

Considering the fact that magnetic nanoparticles find many popular applications in the biological and/or microfluidic field and so often find themselves immersed in some fluid, then, with the approximations

$\mathbf{m} = V\mathbf{M}$;

$\mathbf{M} = \Delta\chi\mathbf{H}$;

$\Delta\chi = \chi - \chi_{fluid}$ (effective susceptibility relative to the fluid magnetic nanoparticles are immersed in);

$\mathbf{B} = \mu_0\mathbf{H}$ (a dilute suspension of nanoparticles considered in this case allows this approximation);

we finally arrive at the following form of the previous equation [67]:

$$\mathbf{F}_{magn} = \mu_0 \int_{V_{bead}} (\mathbf{M} \cdot \nabla) \, \mathbf{H} dV \approx \mu_0 V_{bead} \left(\mathbf{M} \left(\mathbf{r}_c \right) \cdot \nabla \right) \mathbf{H}(\mathbf{r}_c) \tag{2.53}$$

where it has been assumed that, to a first approximation, the length scale associated to the magnetic field gradient is larger than the bead dimension, and the magnetic properties of the medium have been neglected. $\mathbf{H}$ is the applied magnetic field, $\mathbf{r}_c$ the position of the bead, V_{bead} its volume.

Assuming the material of the beads is isotropic, non-dispersive and has linear susceptibility, Equation 2.53 becomes:

$$\mathbf{F}_{magn} = \mu_0\chi V_{bead} \left(\mathbf{H} \left(\mathbf{r}_c \right) \cdot \nabla \right) \mathbf{H} \left(\mathbf{r}_c \right) \tag{2.54}$$

Considering the identity $(\mathbf{H} \cdot \nabla) \mathbf{H} = \frac{1}{2} \nabla (H^2)$, we finally obtain:

$$\mathbf{F}_{magn} = \frac{1}{2} \mu_0 \chi V_{bead} \nabla H^2 (\mathbf{r}_c) \tag{2.55}$$

Therefore, in order to apply a significantly strong force to the beads, and in turn to obtain a detectable signal, for a given susceptibility χ, the size of the particles and the gradient of the square of the externally applied field are the two most important parameters one can work with, to obtain improvements in the measurements.

For the sake of completeness, it is necessary to specify that this expression can be made even more general by considering the initial magnetization of the beads $\mathbf{M}_0$ which results in an extra term in the force [68]. Let's therefore consider:

$$\mathbf{M} = \mathbf{M}_0 + \mathbf{M} (\mathbf{H}) = \mathbf{M}_0 + \chi_{bead} \mathbf{H} \tag{2.56}$$

Where χ_{bead} is magnetic susceptibility of the bead (dimensionless) obtained from the magnetization curve, defined as the slope of the initial (starting from the fully relaxed state) part of the magnetization curve. These considerations would result in an extra term for the force:

$$\mathbf{F}_{magn} = \frac{1}{2} \mu_0 \chi V_{bead} \nabla \left(H^2 (\mathbf{r}_c) \right) + \mu_0 V (\mathbf{M}_0 \cdot \nabla) \mathbf{H} \tag{2.57}$$

The initial magnetization of the bead $\mathbf{M}_0$, present in absence of the applied magnetic field, depends on the history of prior magnetization of the bead. In general, its value for a single specific bead may be anything from zero to the remnant magnetization. In the case of the beads in use in the present experiments, however, the measured hysteresis loop presented negligible magnetization for null field, so it is safe to assume that the used beads have no initial magnetization, and the extra term in the force can be neglected.

2.4   Opto-magnetic biosensing

In this section all the biochemical, optical and magnetic notions illustrated so far are combined to make up a reliable sensing mechanism which is useful for various biological assays. Optical waveguides are able to reveal the biochemical reaction on top of them and this constitutes a first quantitative detection. Furthermore, once magnetic beads bind to the biological sample, they can interact with a time-varying magnetic field with specific dynamics that can be sensed by the resonator.

2.4.1   Biosensing with optical waveguides

Evanescent waves produced by total internal reflection within the resonator extend up to a distance λ outside the silicon waveguides. Planar ring resonators have light guided in a solid medium while liquid samples flow near the sensing surface. The biological samples are probed by the evanescent waves immediately outside of the waveguide, where organic molecules with higher refractive index are bound to the surface of the ring, while fluids with lower refractive index (such as water) are displaced: the electric field-induced dipole moment of the target molecules is higher than that of the solution [69], and this will impact the modes within the guide together with propagation parameters, specifically the refractive index.

Interaction with the molecules thus depends on the ring length because this determines the number of surface sites actually present on the thin waveguide, and also on the number of times waves interact with the sample, i.e. on the number of loops (commonly around $10^4 - 10^8$) light travels around the ring before is couples out, which varies with λ_{res}. The resonance of the ring resonator in turn depends on the optical roundtrip length of the ring, and the losses accumulated.
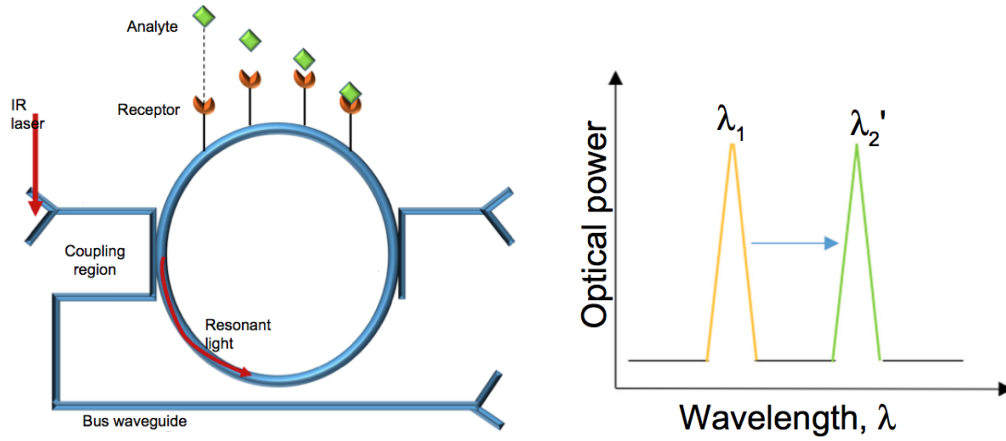
Figure 2.17: Working principle of a ring resonator. Analyte binding occurs on the sensor micro-ring surface, hence the device senses changes in n_{eff} and a difference in resonance wavelengths is recorded. Adapted from [2].

Sensitivity can be defined as the wavelength shift $\Delta\lambda_{res}$ caused, in our case, by the coupling between evanescent field tails and biological molecules, which is basically due to a change of the value of the refractive index of the mode. Recalling Equation 2.29, we can quantitatively write this as:

$$\Delta\lambda_{res} = \frac{\Delta n_{eff}L}{m}, \quad \text{m=1, 2, 3, ...} \tag{2.58}$$

in which m is the order of the mode.

A rigorous derivation of the sensitivity of n_{eff} of waveguides for variations of the environment was performed in [70].

2.4.1.1 Signal enhancement with magnetic beads

Thanks to the biorecognition mechanism described above, the presence of hybridized molecules can be detected by simply placing them above the ring. In such a way, these label-free biosensing processes can be performed with a reduced complexity, since additional steps are not necessary and optimization of a microfluidic system is not strictly needed. However, it has
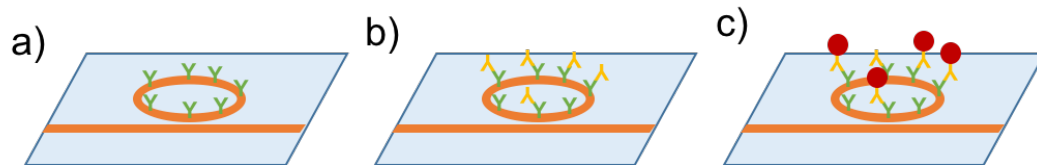
Figure 2.18: The three-step protocol is illustrated: first, a) the micro-ring surface is functionalized with appropriate ligands, then b) a solution of analytes allows for biochemical reactions to occur, already producing a detectable, although often small, signal in the form of a resonance wavelength shift, and finally c) magnetic beads are made to bind to the target compounds, enhancing the acquired signal.

been proven in literature (see [35] [71]) that a multiple-step assay format is a method of confirmed efficacy: a nanoparticle-enhanced binding event is added to the protocol and observed in real-time in order to sensitively quantitate the presence of the analyte over an improved range of concentrations. The nanoparticle passive-labelling assay lowers the limit of detection by enhancing the optical signal arising from a single bound analytes. Besides, it also increases the specificity of the assay by requiring additional target-specific recognition, allowing discrimination against non-specific interferants.

The use of small particles of the order of $100 - 150$ nm does not result in significant sedimentation upon the surface within the expected binding times, which would be detrimental for sensing measurements because it would imply the presence of many false positives. This avoids the necessity for a delicate washing step, which could be performed in a reliable way only with a microfluidic system, increasing the complexity of the whole approach.

In this step, nanoparticles do not necessarily need to be magnetic, since only their binding capacity is exploited, however in view of a different kind of investigation to be performed on the same system, involving magnetic actuation, magnetic beads were used in this assay.

Since the addition of beads will turn out to be the real fundamental step that raise the magnitude of the detected signal over the intrinsic limit of detection of the system, it is important to underline the different factors that may influence the variation of the response with time: indeed, some phenomena that are strictly connected to the implemented protocol determine spurious conrtibutions to the acquired wavelength shift. At a given time the relative response R of the optical biosensor, which in our case corresponds to the resonance wavelength shift of the optical resonator, obtained in this kind of investigation can be expressed as

$$R(t) = \Delta\lambda_{res}(t) = \Delta\lambda_{res}(\Delta T(t), n_{buffer}(t), N(t), \Sigma(t)) \qquad (2.59)$$

In this equation, the possible factors that may affect the response in time have been introduced: $\Delta T(t)$ is the temperature difference between the micro-resonator and the external medium it is directly in contact with, which can be the air at the beginning, and the dispensed buffer solution afterwards; n_{buffer} is the refractive index of the external medium, that goes from being close to 1 when there is air, to a larger value in presence of the aqueous solution; $N(t)$ is the number of immobilized target entities upon biomolecular recognition (in this case, the binding between the beads' streptavidin and biotinylated target ligands positioned on the surface); $\Sigma(t)$ represents the amount of sedimentation, in particles per unit area, of unbound magnetic beads and/or impurity particles coming from the environment. The change in signal level with respect to time is thus given by

$$\frac{dR}{dt} = \frac{d\Delta\lambda_{res}}{dt} = \frac{\partial\Delta\lambda_{res}}{\partial\Delta T}\frac{d\Delta T}{dt} + \frac{\partial\Delta\lambda_{res}}{\partial n_{buffer}}\frac{dn_{buffer}}{dt} + \frac{\partial\Delta\lambda_{res}}{\partial N}\frac{dN}{dt} + \frac{\partial\Delta\lambda_{res}}{\partial\Sigma}\frac{d\Sigma}{dt}$$
$$(2.60)$$

Figure 2.19 shows a sketch of a non-normalized response signal acquired during the assay. Except for the $10-20$ s at the beginning of an injection when
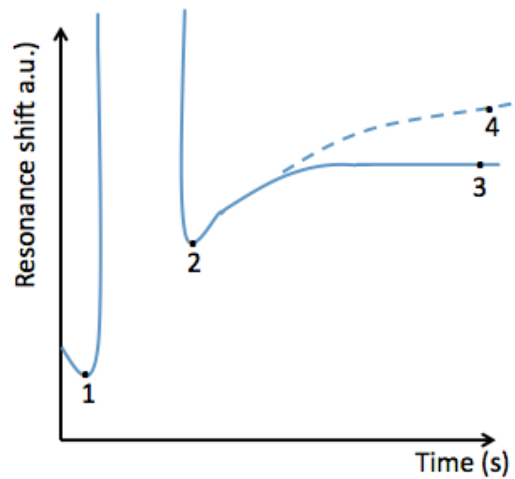
Figure 2.19: Typical non-normalized plot of the resonance signal as a function of time. Points 1, 2, 3 indicate respectively the moment the analyte solution is introduced (1), the stabilization of the buffer and temperature contribution and the beginning of the biorecognition reaction (2), and the saturation of the signal (3). A sketch of possible signal increasing trend due to nanoparticle sedimentation is also shown (4, dashed). Adapted from [3].

running buffer solution is dispensed, $\frac{dn_{buffer}}{dt} = 0$ and hence the contribution is null. Detectable shifts are produced even for small temperature differences between sensor surface and analyte solution (of the order of tens of picometers for $\Delta T = 1$ K [72]), however, after a short transient of time also this contribution falls to zero. Under these circumstances the change in response level reflects the effective binding events N of nanoparticles, provided that the latter are chosen in a size that produces negligible amount of sedimentation Σ and that the duration of the assay is set according to the expected overall binding times. Indeed, if the measurements are carried out for longer times, unwanted spurious contributions due to unavoidable fluctuations could disturb the assay.

2.4.1.2 State of the art

The strategy based on the addition of extra binding bio-entities, which produce a signal enhancement and also an increase in the stringency of the test is already being exploited in other contexts.

On a commercial level, Genalyte company (San Diego, CA, USA) sells the Maverick. This detection system is based on silicon-on-insulator (SOI) ring resonator technology being able to process an assay in 15 min time, which is much faster than traditional ELISA (about 3 hours). Each chip contains 128 separated ring resonators for multiplexed detection. Arrays of rings are serially interrogated using fast scanning mirrors and fast sweeping laser. The analyses are fully automated, with integrated fluid handling, plate sipping, and flow control. The system allows, for example, immunogenicity testing by combining screening, confirmation, and isotyping into a single sandwich assay providing real-time detection of anti-drug antibodies (ADA) without the use of fluorescent probes or radioactive labels. The sensor spots on the assay chip are functionalized with anti-isotype capture antibodies. Anti-drug antibody in the sample is captured and the complex is detected using biotinylated drug followed by streptavidin coated beads causing a change of refractive index. The Maverick system is capable of detecting all immunoglobulin isotypes including monovalent IgG4. However, this platform requires sample pretreatment steps of acid dissociation followed by affinity capture of ADA using drug coated on 96 plates. No user published literature is present on the use of the Maverick, but some currently available information is provided on the vendor's website. Among these, sensograms coming from IgG1 ADA antibodies show a signal up to 10 times larger in magnitude upon addition of the beads. Moreover, quantitative insulin assay employing capture antibody (spotted on chip), the analyte (insulin), the biotinylated detection antibody (in reagent plate) and streptavidin coated beads reported detection signals down to a concentration

of around 25 pg/mL. Multiplex isotyped anti-drug antibody assays for Adalimumab and Infliximab using commercially available monoclonal antibodies spiked into normal human serum and the Maverick Human MT-ADA Assay Kit achieved a sensitivity of 62 ng/mL for both ADAs.

Moreover, in the context of scientific research, a series of papers by Luchansky, Bailey et al. [73] [74] [75] (2010-2011) describe biosensing assays on different types of analytes employing silicon photonic micro-rings and different sensitivity-enhancing strategies. Sandwich assays of antigen between two antibodies allowed for detection of 15.5 kDa human cytokine interleukin-2 (IL-2) and 8 kDa cytokine interleukin-8 (IL-8) with a LOD of around 100 pg/mL (6.5 pM) in both cases. Studies on T cell cytokine secretion in a multiplexing sandwich assay carried out with the same platform showed a LOD of 100 pM in 5 minutes of analysis. Finally, the exploitation of sub-micron beads as passive labels is described in [35]. The signal enhancement from 100 nm nanoparticles (100-fold signal enhancement at 1 ng/mL concentration with respect to standard assays, where the resulting signal was almost negligible) led to a quantification of the cardiac biomarker C-reactive protein with a LOD of 100 pg/mL (around 4 pM). These results were achieved employing a microfluidic system for hybridization protocols.

Still within the framework of the combination of the sandwich scheme with passive labelling, Valera et al. [71] utilized a magnet to attract the beads towards the sensors area, so as to reduce the duration of the assay from about 70 minutes down to 30 minutes (2015). However, in this case the bigger size of the particles (200 nm) and the use of a magnet promoted beads sedimentation. The detection limit was lowered from 124 to 57 pg/mL for the detection of biomarker Monocyte chemotactic protein 1.

In those years some good results were achieved also employing label-free methods: among these, the results obtained by Kindt et al. [76] is worth

mentioning because of the low detection limits that were reached in a sandwich-based assay scheme using silicon micro-ring resonators and enzymatic signal enhancement strategy. For all the targets tested a LOD of 1 pg/mL was reached, with a linear dynamic range extending from 1 up to 1000 pg/mL. An exceptionally low LOD of 500 fg/mL was reported for target analyte IL-8.

However, over the last few years, the labelled approach is generally preferred even at the cost of a longer time for the assays, because it enables to reach extremely low LOD values.

2.4.2 The opto-magnetic platform

In the described optical biosensing technique, a real-time monitoring of the signal is necessary to evaluate the correlation between resonance wavelength shifts and the binding dynamics. Nevertheless, such a requirement makes the whole method quite time consuming. Moreover, the precise discrimination of signal contributions coming from effective recognition reactions and from spurious contributions can be highly demanding in real practical cases. For this reason, a more robust detection strategy is proposed, combining the use of biosensitive waveguides and magnetic actuation of nanoparticles. This method does not require real-time measurements to monitor the binding dynamics and is much more insensitive to disturbances, fluctuations and spurious contributions.

After the biochemical reaction and the addition of magnetic particles which bind to target molecules on the surface of the micro-ring resonator, the magnetic properties of the utilized beads are exploited.

A tunable laser sends light with varying wavelength into the bus waveguide which couples to the micro-ring, and ultimately the resonator transmission spectrum is acquired. One of the multiple notches is chosen as a reference and the laser wavelength is tuned to the one corresponding to the maximum slope of
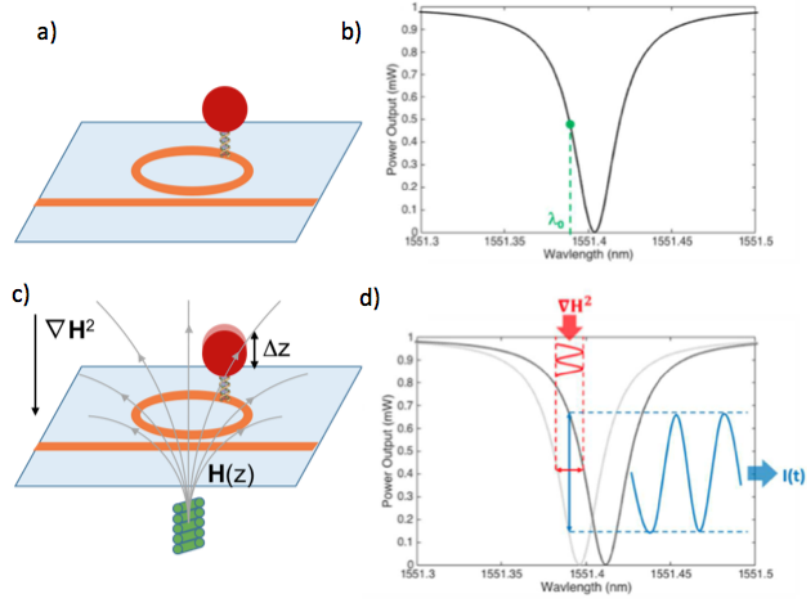
Figure 2.20: Sketch of the platform: (a) the bead-DNA complex is positioned on the ring; (b) the corresponding maximum slope wavelength position is determined; (c) the oscillating magnetic field generated by an electromagnet displaces the beads and (d) causes a shift $\Delta\lambda$ in the spectrum, which is reflected by a variation of the intensity read at initial λ_0.

the notch, λ_0, because this point provides maximum sensitivity to wavelength shifts.

Afterwards, a sinusoidally time-varying magnetic field is applied: its optimum spatial profile should be such that it provides a significant gradient, especially in the z direction perpendicular to the surface. Therefore, the force magnetic beads are consequentially subjected to is large enough and able to push the particles downwards by a distance Δz. This perturbation of the conditions immediately above the waveguide is sensed by the evanescent field tail of the mode travelling within the micro-ring, ultimately resulting in a change of the refractive index Δn which is directly related to a resonant wavelength shift, as previously stated in Equation 2.58 in Section 2.4.1. Hence the notches in the transmission spectrum shift with wavelength, and the acquired intensity

transmission at λ_0 changes. If, to a first approximation, the behaviour of the notch around λ_0 is assumed linear, the detected change in output intensity is:

$$\Delta I(\lambda_0) = I(\lambda_0 + \Delta\lambda) - I(\lambda_0) \approx \left(\frac{\partial I}{\partial \lambda}\right)_{\lambda_0} \Delta\lambda \qquad (2.61)$$

A schematic of the platform is provided in Figure 2.20.

2.4.2.1 Magnetic particles in AC magnetic field

As explained in Section 2.3.5, in presence of an external magnetic field $\mathbf{H}$, magnetic nanoparticles experience a force given by $\mathbf{F}_{magn} = \frac{1}{2}\mu_0 \chi V_{bead} \nabla H^2 (\mathbf{r}_c)$ (Equation 2.55).

If the applied field is non-homogeneous and time-varying, the field gradient will oscillate in time, and the force will follow too. If we write the magnetic field in sinusoidal form

$$H(z,t) = H_0 \sin(\omega_0 t) \qquad (2.62)$$

then H^2 is given by

$$H^2(z,t) = H_0^2(z)sin^2(\omega_0 t) = \frac{H_0^2(z)}{2} - \frac{H_0^2(z)}{2}\cos(2\omega_0 t) \qquad (2.63)$$

If H^2 oscillates at $2\omega_0$, so does ∇H^2, which results in a unipolar magnetic force being applied to the beads, periodically displacing them downwards in the case of a gradient pointing towards the sensing surface. This periodical perturbation will cause fluctuations at $2\omega_0$ in the refractive index and field wavelength inside the optical resonator. As a result, also the transmitted intensity will oscillate at the same frequency, with an amplitude given by Equation 2.61 that is, to a first approximation, directly proportional to the first derivative of the transmission spectrum:

$$\Delta I(\lambda_0) \simeq \left(\frac{\partial I}{\partial \lambda}\right)_{\lambda_0} \Delta\lambda(2\omega_0) \qquad (2.64)$$

It follows, as will be further explained in Chapter 4, that the choice of the oscillation frequency $f = \frac{\omega_0}{2\pi}$ should be made to maximize the amplitude

of the response of the beads bound to the probe-target complexes. This can be computed within the context of a mass-spring elastic model under the appropriate assumptions (see Section 2.4.2.2), and also evaluated experimentally by acquiring and comparing signals at different frequencies. Also the signal-to-noise ratio must be taken into account, because of the presence of low frequency noise components which might affect the quality of the results.

2.4.2.2 Labelled complex in AC magnetic field: mass-spring model

The biological sample used in this thesis work for opto-magnetic measurements was DNA, because it had been largely employed before and good repeatability of experimental results was achieved, and thus it was eligible to lend itself for the optimization of the system.

Plenty of works in literature can be found about micromechanics of oligonucleotides [77] [78] [79] [80]. A single DNA strand can be modeled as a spring attached to the bead above, which plays the role of a mass. Once a magnetic field is applied, because of its gradient profile it displaces downwards magnetic nanoparticles, and this induces a compressive force on the spring. Lateral displacement is supposed negligible, while the vertical one is supposed to be $\Delta z = \frac{F_{magn}}{k}$, where F_{magn} is given by Equation 2.55, its behaviour in the case of a time-varying field being provided in Section 2.4.2.1, and k is the effective elastic constant for DNA.

We can consider double-stranded DNA molecules as semi-flexible polymers, in the context of the so-called worm-like chain model (WLC) [81]. According to the model, if the examined polymer is longer than a certain persistence length, then at finite temperatures thermal fluctuations will act on the complex and the initially unperturbed polymer will end up in a coiled, random configuration, and its end-to-end distance will be significantly shorter than the maximum length. An estimate for oligonucleotide persistence length is 50 nm, which means 150

bases. However, the samples used in this work display 20 nm strands, smaller than the persistence length, so we can safely consider our DNA molecules as stiff rods with low tendency to fold up on themselves multiple times. As will be further specified in Chapter 4, the model should consider every bead attached to a certain number of parallel DNA stiff strands. In this picture, the applied force might result in a tilting action rather than a contraction of the spring. In this case, if we want to roughly describe the system through the mass-spring model, the effective elastic constant $k = F/\Delta z$ experienced by the beads can be evaluated in terms of a displacement Δz produced by this tilting phenomenon. This evaluation should be made considering the picture of the DNA molecule hinged to the surface and subjected to a torque. However this has not been fully developed and calibrated with reference to our system. The following discussion is thus still based on the idea of an effective elastic constant related to the beads tilting, and in order to relate the experimental measurements to this theoretical model the effective elastic constant was evaluated through experimental results and appropriate estimates.

If we now consider the bead-DNA complex attached to the sensing surface in aqueous solution, the dynamics of the bead in presence of a magnetic force coming from the field are those of a damped oscillator because of fluid viscosity:

$$\ddot{x} + 2\gamma\dot{x} + \frac{k}{m}x = \frac{F_0}{m}\sin(\omega_F t) \tag{2.65}$$

In the equation, $F_0\sin(\omega_F t) = F_{magn}$ applied to the particles at a frequency $\omega_F = 2\omega_0$ with respect to the sinusoidal field, as stated in Section 2.4.2.1. Besides, $\gamma = \frac{6\pi\eta r}{2m}$, where η is the fluid viscosity and r, m the radius and mass of the bead, respectively. The general solution is in the form of a linear combination of the homogeneous solution $x_0(t) = C_1 e^{-\alpha_1 t} + C_2 e^{-\alpha_2 t}$ and a particular solution $x_p(t)$. The characteristic equation for the homogeneous solution leads to the determination of the exponential coefficients α_1 and α_2:

$$\alpha^2 + 2\gamma\alpha + \frac{k}{m} = 0 \tag{2.66}$$

$$\Longrightarrow \alpha = -\gamma \pm \sqrt{\gamma^2 - \frac{k}{m}} \tag{2.67}$$

As will be demonstrated in Chapter 4, considering realistic values for the parameters at stake, referring to our specific system, a transient exponentially-decreasing contribution is expected from the homogeneous solution, coming from the overdamped motion regime of the case $\gamma^2 - \frac{k}{m} > 0$.

The second contribution is computed assuming for the particular solution a harmonic behaviour at the same frequency of the applied force: $x_p(t) = a \sin \omega_F t + b \cos(\omega_F t)$. The resulting solution harmonically oscillates, once again, at the same frequency: $A_p = \tilde{A}(\omega_F) \sin(\omega_F t + \phi)$, where $\tilde{A}(\omega_F)$ is given by

$$\tilde{A}(\omega_F) = \frac{\frac{F_0}{m}}{\sqrt{\left(\frac{k}{m} - \omega_F^2\right)^2 + \gamma^2 \omega_F^2}} \tag{2.68}$$

The derivation of appropriate estimates for the significant quantities in this model based on the specific system at our disposal is devolved to Chapter 4.

Chapter 3

Experimental methods

This chapter describes in more detail the technical devices that allow to perform the experiments with the biosensing system. In particular, a description of the optical system for signal transduction of the biochemical reaction is provided. The microchips with the arrays of micro-ring resonators and the laser-fiber system for signal transmission; moreover, the additional devices required to perform magnetic transduction in the opto-magnetic platform are presented, focussing in particular on the optimized electromagnet structure that was designed with the aim to provide an adequate value for the magnetic field and gradient.

3.1 Main components

In this thesis we present results obtained exploiting magnetic particles as passive or active labels of target molecules immobilized at the surface of micro-ring resonators. The basic constituents of the corresponding biosensing technology platforms are illustrated below.

3.1.1 Microchips

The experiments carried out in this work were performed using 6x5 mm^2 silicon photonics microchips provided by STMicroelectronics.
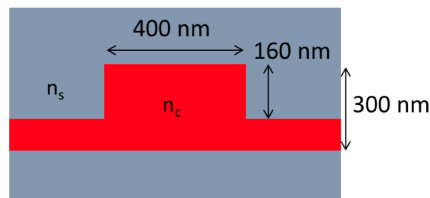
Figure 3.1: Sketch of the waveguide structure.

Such microchips are characterized by a 160 nm high x 400 nm wide rib silicon waveguide (see Figure 3.1) lying over a silicon dioxide layer. Each chip features two columns of 7 micro-ring each and extra 4 resonators on one side of the chip, all of them in the add-drop configuration and having a diameter of 80 μm. The experiments were carried out on the 4 side micro-rings only, because the others would require the output reading via photodiodes, not integrated in these chips, and only the all-pass port was used for simplicity. The 4 rings are characterized by four different values of the Q_{factor} and this results in different shapes in the notch transmission spectra, the high-Q notch being narrow and steeper with respect to a low-Q one, as shown in Figure 3.2.

The waveguides was lying underneath a multilayer structure of multiple alternated silicon dioxide and silicon nitride strata, thus it was necessary to
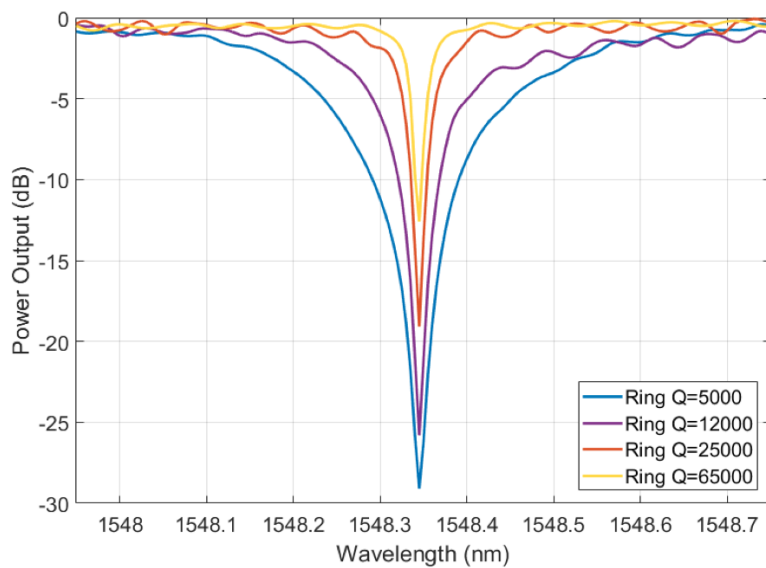
Figure 3.2: Notch in the transmission spectra of the four different rings.
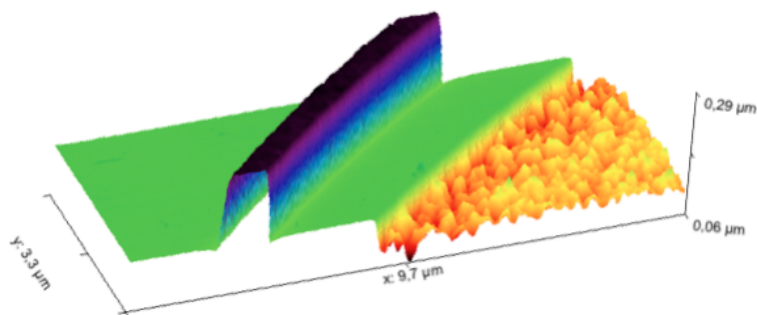
Figure 3.3: 3D AFM profile of the real waveguides.

perform some microfabrication steps in order to expose the waveguide. Reactive ion etching and hydrofluoric acid wet etching techniques were exploited. Figure 3.3 shows the final 3D shape of the surface of the exposed silicon waveguides, and in Figure 3.4 the four active micro-rings connected to the respective optical power outputs are reported.
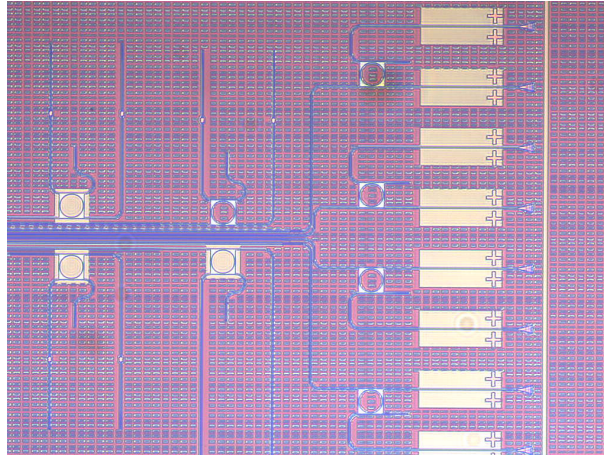
Figure 3.4: Top view of the 4 active micro-rings and the respective optical power output ports.

3.1.1.1 Surface biochemical functionalization

In order to investigate the sensitivity of the optical biosensing platform with superparamagnetic nanoparticles as passive labels, the surface of the chip was first functionalized with probe ligands. As already mentioned, the optical real-time measurements of resonance shifts upon adding complementary analytes and labelling beads were carried out using antigen p24: p24 is a component of the capsid of the HIV particle, with molecular weight of 24 kDa. The protocol was based on the formation of a sandwich structure of p24 protein in the middle of two artificial antibodies (dissociation constant assumed to be in the range $10^{-6} - 10^{-8}$ M [82] [3]), in order to look into detection limits and build a calibration curve. To enable the immobilization of probe reactants, the surface of the chip was coated with a functional polymer that covalently binds to antibodies. Probe antibodies were then immobilized onto the surface by spotting a 1 μg/mL solution with an inkjet spotter. A blocking step was carried out using BSA (bovine serum albumin), in order to avoid non-specific binding interactions during the following steps.

Biosensing analyses are performed by means of two hybridization steps: the first solution dispensed on the chip contains target HIV antigen p24 at the chosen concentration, diluted in PBS (phosphate buffered saline) and BSA to promote hybridization (duration: 2 hours); after the appropriate washing step to remove unbound species the sensor surface is exposed for one hour to a PBS solution of 1 mg/mL of secondary antibodies which bind to the antigen and form the desired sandwich structure. Another washing step is followed by the injection of magnetic nanoparticles for the labelling step, still in a PBS solution. The binding involves streptavidin molecules the beads are functionalized with, and the biotin that is attached to secondary antibodies (dissociation constant around 10^{-14} M, for expected total binding time of $15-30$ min estimated at the end of Section 2.1). Small particles with diameter on the order of $100-300$ nm were used, which do not present sizable sedimentation. Another washing step concludes the labelling stage. An image of the biosteps for the sensing protocol is reported in Figure 3.5
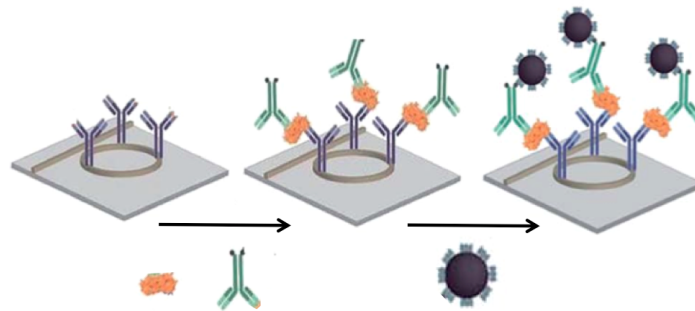
Figure 3.5: p24 sandwich protocol. The ring is spotted with antibodies; subsequent hybridizations with antigen and secondary antibody lead to final sandwich formation; magnetic particles are added and captured by target complex.

The use of the same bioassay for the development of the opto-magnetic platform was unpractical for many reasons: the high cost of reagents, the complexity of the hybridization protocol and also the reduced length of the

probes-target complexes which could be critical for the magnetic beads actuation For these reasons we adopted a DNA-based model of bioassay. The utilized DNA molecules consist of 60 nitrogenous bases roughly corresponding to 20 nm length of the double strand after biomolecular recognition. The spotting protocol of DNA receptors in a concentration of 10 μM onto the chip surface is similar to the one employed for p24 sandwich structure. Complementary DNA molecules at the chosen concentration are dispensed over the reactive chip surface and left there in static conditions for 2 hours to promote binding. Furthermore, target DNA molecules are functionalized with biotin, which once again allows for the bond with streptavidin-coated magnetic beads.

3.1.2 Electromagnet

The oscillating space-varying magnetic field required to induce a driving force acting on the magnetic particles was produced by means of an electromagnet. However, a classical electromagnet configuration with a cylindric iron core was found to be not appropriate to generate an optimum spatial gradient of H^2 to maximize the acquired signal from the opto-magnetic system. Therefore, combining theoretical considerations with COMSOL Multiphysics simulations, a new design of the ferromagnetic core was developed. Many structures have been implemented and compared, varying electromagnet parameters and the shape and material of the core, in order to finally obtain a good design to assure the availability of a gradient bigger than the previously obtained one, of the order of 10^9 A^2/m^3, in the targeted volume occupied by the ring resonators. The region where the effect needs to be maximized corresponds to the area where the active rings are, with a surface of approximately $1 - 2$ mm^2 at a distance

of at least 700 μm from the top of the electromagnet core, corresponding to the thickness of the silicon chip[1].

3.1.2.1   Theoretical derivations
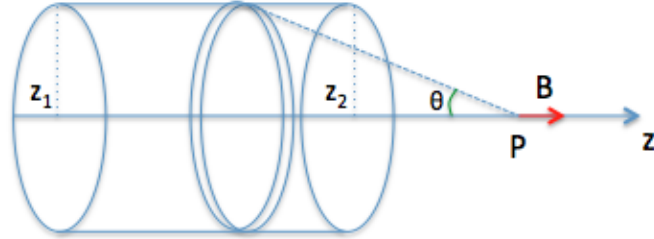
Figure 3.6: Sketch for extending the calculations to the case of a finite electromagnet.

The expression of the magnetic field generated at point P at a distance z from the center of a finite solenoid with N windings is given by:

$$B(z) = \frac{\mu_0}{2} nI(\cos\theta_2 - \cos\theta_1) \tag{3.1}$$

where a current $I_{tot} = nIdz$ has been used, n being the winding density per unit length, and θ_1 and θ_2 are the angles between point P and the to extremes z_1 and z_2 of the solenoid as reported in Figure 3.6. If we want an idea of the trend of quantities relevant for our purposes (i.e. magnetic field, gradient of the square of the magnetic field), we can roughly consider that, as a function of the distance from the electromagnet:

$$B(z) \propto \frac{z}{\sqrt{z^2 + \alpha^2}} \tag{3.2}$$

$$B^2(z) \propto \frac{z^2}{z^2 + \alpha^2} \tag{3.3}$$

---

[1]The thickness of the chip holder should also be take into account, however in the hope for an appropriate optimization of the system the holder thickness should be possibly equal or smaller than 1 mm.

And thus, the z component of the gradient:

$$\nabla B^2 \propto \frac{2z}{z^2 + \alpha^2} \left(1 - \frac{z^2}{z^2 + \alpha^2} \right) \tag{3.4}$$

A plot of the behaviour of the discussed quantities is provided in Figure 3.7. These theoretical trends show the behaviour of the field and gradient that is expected from this kind of structure, and represent a useful reference and mean of comparison with respect to the measured same quantities characterizing the real practical case structure.
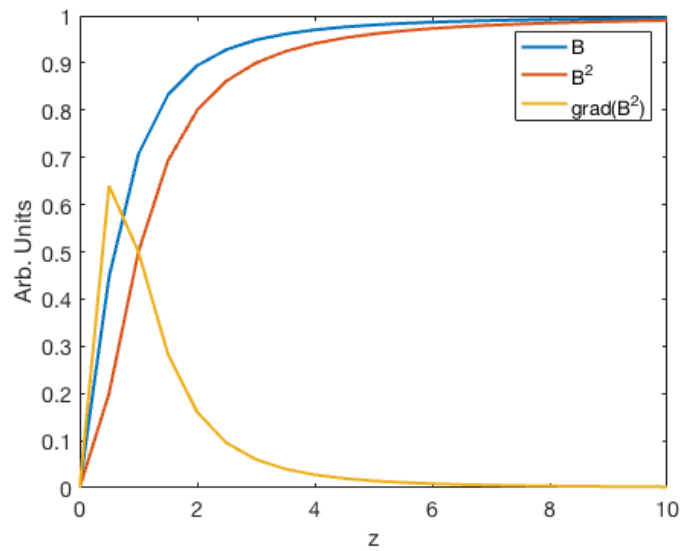
Figure 3.7: Behaviour of the magnetic field, square of the magnetic field and relative gradient as a function of the distance z from the extreme of the electromagnet.

3.1.2.2   Improving the gradient profile

Once the theoretical trends expected for the real case had been defined, COMSOL simulations were performed in Magnetostatics mode for a coil system with a ferromagnetic core.

The involved Maxwell equations are:

$$\nabla \times \mathbf{H} = \mathbf{J} \tag{3.5}$$

$$\nabla \cdot \mathbf{B} = 0 \tag{3.6}$$

with the constitutive relation $\mathbf{B} = \mu_0 \mu_r \mathbf{H}$. The Ampère-Maxwell law for quasi-static systems governing the Magnetostatics mode is:

$$\nabla \times \left(\mu^{-1} \mathbf{B} \right) - \sigma \mathbf{v} \times \mathbf{B} = \mathbf{J}_e \tag{3.7}$$

where $\mathbf{J}_e$ is an externally generated current density and σ is the coil electrical conductivity ($5.8 \cdot 10^7$ S/m for copper). $\sigma \mathbf{v} \times \mathbf{B}$ represents the correction to the charge current density distribution due to the contribution of the Lorentz force term on a particle travelling at speed $\mathbf{v}$ in the context of the quasi-static approximation. Finally, the constitutive relation for coils:

$$\mathbf{J}_e = \frac{N I_{coil}}{S} \mathbf{e}_{coil} \tag{3.8}$$

where N is the number of turns, S is the total cross sectional area of the coil domain and $\mathbf{e}_{coil}$ is the unit vector along the infinitesimal direction of the current in the coil.

The basic input parameters are the relative permeability μ_r of the ferromagnetic core in the linear regime and the current density within the coils of the electromagnet. The relevant magnetic constants and boundary conditions are presented in Table 3.1. The magnetic insulation boundary condition is expressed in terms of vector potential $\mathbf{A}$ (constitutive relation: $\nabla \times \mathbf{A} = \mathbf{B}$). If we think of the coil as sitting in a space that extends to infinity and does not contain anything else, the domain (modeled as an air sphere with size a hundred times larger than the characteristic radius of the coil) must be truncated to some finite size that will give reasonably accurate results but will not require too much computational effort to solve. Mathematically speaking, the magnetic insulation fixes the field variable that is being solved for to be zero at the boundary.

In principle, the starting idea to improve the gradient on top of the electromagnet was based on the observation that a ferromagnetic core with a very

Magnetic constants/B.C.	Value/expression
Relative permeability μ_r	4000 (iron)
Magnetic insulation	$n \times \mathbf{A} = 0$
Initial value	$\mathbf{A} = 0$

Table 3.1: Magnetic constants and boundary conditions (B.C.)
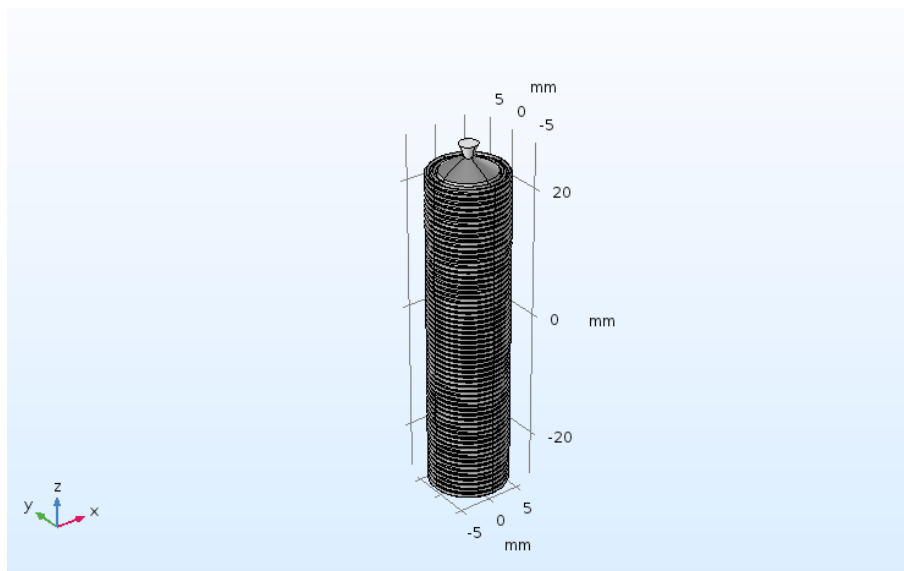
Figure 3.8: 3D shape for the designed system of electromagnet and ferromagnetic core.

sharp tip would be able to confine the magnetic flux density up to the tip and then "release it" in a fountain-like space profile. However, simulations showed that the effective improvement of the gradient was limited to a circular-like three-dimensional corona of radius of a few tens of microns with respect to the tip. Therefore, simulations were carried out on a modified version of this geometry, which is shown in Figure 3.8.

The cylindric core shrinks into bottle neck-shaped configuration, which in turn widens a bit as an inverted cone. This increases the effective volume in which a significant H^2-gradient is generated. Hence the sketch in Figure 3.9
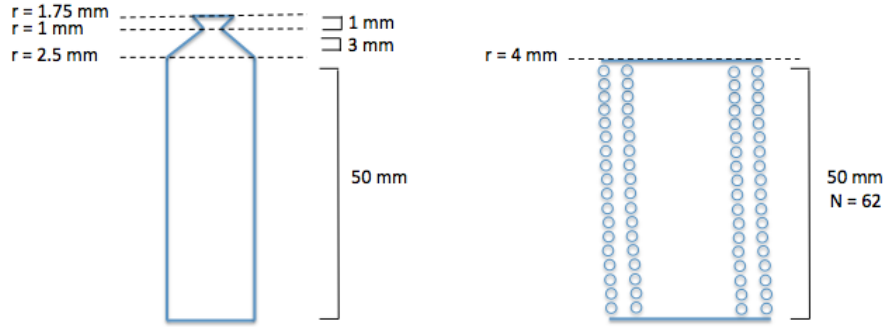
Figure 3.9: Schematic with the shape and values of the principal geometric quantities of the ferromagnetic core (on the left) and copper coil (on the right).

Coil parameters	Value
Diameter of the copper wire	$d = 0.8$ mm
Number of windings	$N = 62$
Number of winding strata	$M = 2$
Input current	$I = 2$ A
Resistance	$R = 0.126\ \Omega$
Power loss	$P = 0.504$ W

Table 3.2: Parameters of the iron-cored coil design.

reports the relevant geometric values for the ferromagnetic core and copper coil, while Table 3.2 indicates further characteristic parameters.

The height of the coil (and thus, the number of windings) was fixed optimizing the competing factors of field, gradient magnitude and compatibility with the available space in our set-up. In order to further improve the desired effects, two series of top-to-bottom windings were made around the coil, and the copper wire was chosen with a diameter large enough to allow for sufficient input current without heating up too much in the operating time.

Figure 3.10 shows the plot for ∇H^2 obtained employing this geometry in the simulations. As can be seen in the image, the reached gradient retains a value of the order of $10^{11} - 10^{12}$ A^2/m^3 within the first millmeter above the structure,
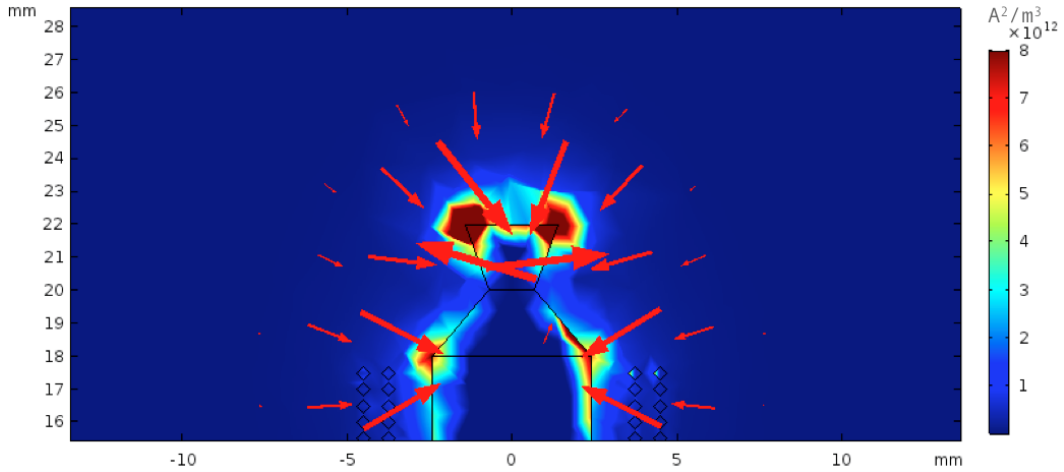
Figure 3.10: Simulations on ∇H^2 (A^2/m^3). The colour-scale is based on the gradient magnitude, while red arrows represent the local direction of magnetic field **H**.

approximately, and within an adequate transverse surface. This constitutes an improvement with respect to the previously available electromagnet: indeed, this structure was purely cylindric in the ferromagnetic iron core, with core radius of 2 mm, coil radius of 3 mm and 20 mm high, and displayed within the first millimiter from the top of the structure a gradient of around $7 \cdot 10^9$ A^2/m^3. As will be specified later in the Chapter, the expected optimum working frequency for AC magnetic field generation was identified in the low value of 10 Hz, hence Stationary mode simulations were taken as a good starting initial approximation for the studied behaviour. Figure 3.11 shows the experimentally obtained (by means of a gaussmeter) field and gradient values as a function of the distance from the structure surface in comparison with COMSOL simulations and the previously available electromagnet structure, and demonstrates the agreement of experimental trends with theoretically computed ones.
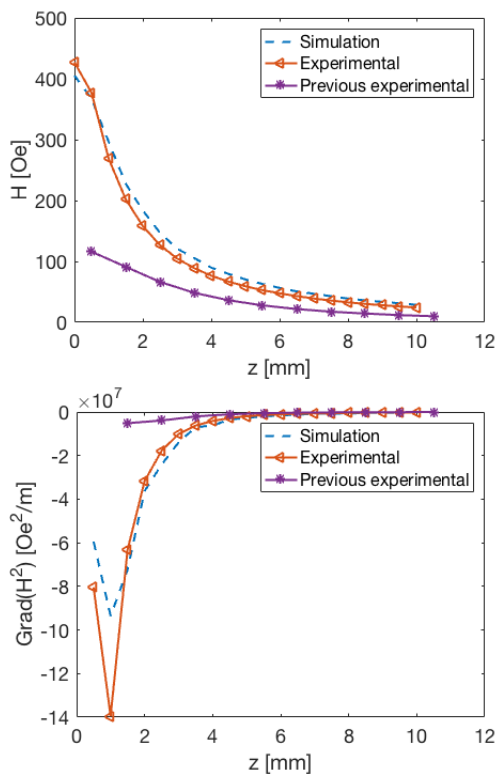
Figure 3.11: Present and previous experimental values for H and ∇H^2 against simulated trends.

3.2 Experimental set-up

3.2.1 Optical measurements

As already mentioned, optical measurements on the $\Delta\lambda_{res}$ shift, due to the immobilization of bioreagents and magnetic markers, were carried out on antibody-p24 antigen-antibody sandwich to estimate limits of detection and calibration curve in case of a label-based protein immunoassay.

The chip is positioned onto a PMMA (polymethylmethacrylate) holder, which features a well-shaped central region that allows for injection of the various solutions. The optical measurement set-up comprises a tunable laser (Agilent 8164B lightwave measurement system) as an IR optical source, which

injects photons into the circuit by means of input optical fibers; a photodiode converts intput optical power into voltage signals; an optical microscope was used for fiber alignment to the input and output gratings of the waveguides on the silicon chips. Input coupling efficiency is maximized through the use of polarizers and intensity transmission is measured through a power meter.

3.2.2   Opto-magnetic measurements

Experiments on the opto-magnetic set-up were performed with DNA molecules because it had shown stable repeatable results in many previous experiments and, in the view of the possibility to optimize some parameters for the system, it was considered a good starting point for tests and comparisons.
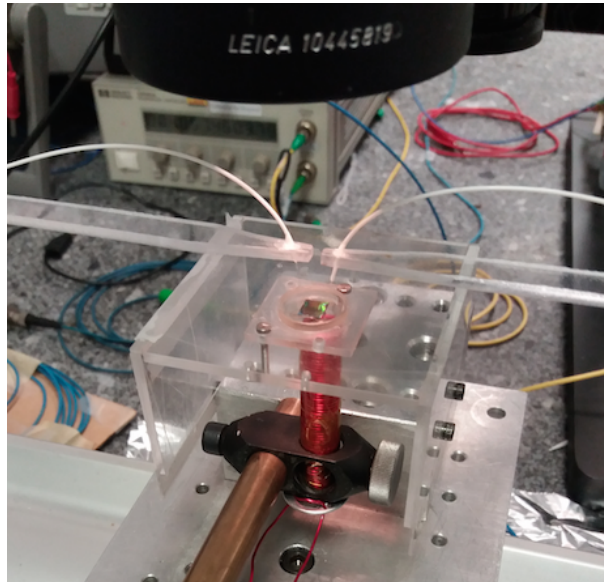
Figure 3.12: Close-up look of the chip placed on the PMMA holder above the electromagnet.

The opto-magnetic platform comprised, besides all the elements already mentioned in the previous section, an electromagnet (see Section 3.1.2 for specifications) able to generate the magnetic field and the spatial gradient producing the force that actuates the beads. The PMMA holder allows for the

positioning of the electromagnet very close to the chip (Figure 3.12). A signal generator produces the sinusoidal signal at frequency f_0 for the lock-in amplifier (Zurich instruments HF2LI Lock-in amplifier) and for a voltage-to-current converter (Kepco bipolar operational power supply/amplifier) that drives the electromagnet. The transmitted signal at the photodiode is fed back into the lock-in amplifier which demodulates it at frequency $2f_0$ and rejects signals due to electronic noise.

Figure 3.13 sums up the main components of the measurement system.
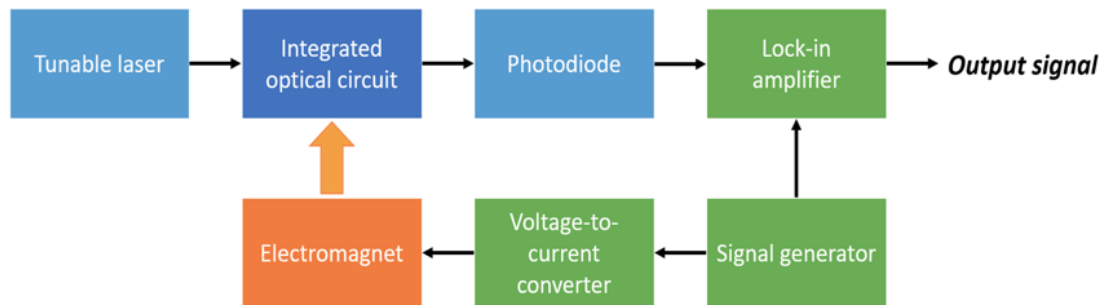
Figure 3.13: Block scheme of the opto-magnetic platform.

Chapter 4

Experimental results

In this chapter the obtained results are discussed. Biosensing assays have been performed with the purely optical system on antigen p24 sandwiched between two antibodies, and the resonance wavelength shift of the optical resonator has been acquired upon adding nanoparticles as passive labels. Data for different antigen concentrations are analyzed and commented in the light of theoretical assessments. A calibration curve displaying measured shifts as a function of antigen concentration is reported, thus providing a quantitative assessment of the feasibility of the whole assay. Some intrinsic limitations of this approach can be overcome combining the latter with the opto-magnetic platform assay, which involves actuation of magnetic nanoparticles with a time-varying magnetic field. This system has been studied with DNA molecules, and possible strategies devoted to maximizing the acquired signal response are discussed, involving the resonator and magnetic beads characteristics. Finally, measurements with the optimized parameters and conditions lead to the determination of a calibration curve for DNA.

4.1 Optical results: p24

This section presents measurements with the purely optical system performed on the antigen p24-antibody biological complex, starting from some simple estimates on the expected detection limit backed-up by the already known theoretical considerations. Afterwards, a description of the standard procedure employed during the experiments is provided and signals from different concentrations are presented, in the view of the construction of a reliable calibration curve, featuring the acquired signal as a function of the employed concentration.

4.1.1 Assessment of detection limits

It is important to underline that the biosensor performance is deeply influenced by the very initial binding process that takes place between analytes and receptors. It determines the biosensor response to the particular concentration of analytes, the time required for the reaction and for complete signal acquisition, the surface coverage and the limit of detection that is interesting in terms of a possible calibration curve. In this section we will make some discussions and estimates regarding the p24 sandwich bio-optical assay.

Assuming that the observed response in the biosensor is proportional to the amount of successfully bound analytes at the functionalized sensor surface, then the output signal strongly depends on the modalities and dynamics of the occupation of the available binding sites by the target analytes. In order to make some estimates for the system, we consider a total functionalized area on the chip of $S \sim 10^{-1}$ mm^2. As mentioned in Chapter 3, the surface is functionalized with 1 μg/mL of antibodies, which corresponds (molecular weight: 150 kDa) to 6.67 nM within a 1000 pL drop of spotting solution, thus to $6.67 \cdot 10^{-18}$ moles. This leads to a surface density of binding sites

$\sigma_{lim} = 6.67 \cdot 10^{-18}/S = 6.67 \cdot 10^{-11}$ moles·m^{-2}. A sample volume of 50 μL is needed to completely cover the chip surface, but assuming only analytes in the region immediately above the rings will take part in the reaction, an active volume of $V \sim 0.6$ μL can be estimated. If we want to assess whether the number of antigen particles is sufficient to completely saturate the immobilized antibodies, we must calculate [A] such that $\sigma_{lim}S \leq [A]V$, which leads to $[A] \geq 10.8$ pM. This means that for concentrations of antigen p24 down to the pM range the equilibrium surface coverage fraction follows the binding site-limited model, with the expression of ξ_{eq} given by Equation 2.2 and the binding kinetics described by Equation 2.6. Due to the difficulty in finding reliable information about biological dissociation constants, we take for the dissociation constant of antigen p24 a value within the range of $10^{-6} - 10^{-8}$ M provided in [82] [3].

Using these values in the equations of Section 2.1.1 and Section 2.1.2 allows to estimate the trend of the equilibrium fractional surface coverage as a function of the analyte concentration and to understand the binding kinetics in time. Taking account of the considered range of dissociation constant values, different values for ξ_{eq} are obtained from Equation 2.2, shown in Figure 4.1. It emerges from the plot that, as already discussed, high values of K do not allow for complete surface coverage at equilibrium even at higher concentrations around the μg/mL (41.67 nM). This has an impact on the signal, which is in turn proportional to the number of bound species. If we consider an intermediate value of 10^{-7} M for the dissociation constant, it is possible to infer from the plot that with an antigen concentration of 1 μg/mL the surface coverage is around 90%. We can consider this as the upper limit for the dynamic range, because all higher concentrations would fill all the available surface binding sites and thus could not be distinguished from one another.
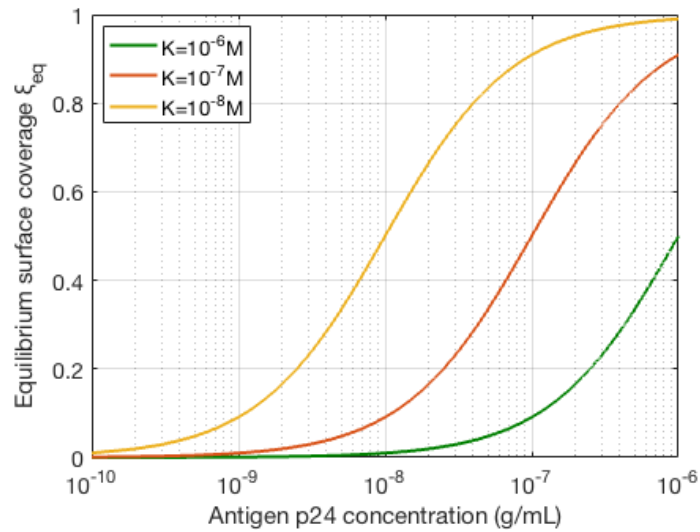
Figure 4.1: Equilibrium fractional surface coverage as a function of antigen concentration for different values of K.

However, the dissociation constant K is not the only potentially limiting factor: as it turned out in the experiments, the mass of antigen p24 is quite small (24 kDa in molecular weight), and this results in a negligible impact on the waveguides. Preliminary experiments were carried out on a concentration of 100 ng/mL. The signal turned out to be below the optical limit of detection or immersed in the unavoidable fluctuations due to the temperature difference between the dispensed buffer solution and the chip. Prior works based on the same technique implemented in a microfluidic cell and employing Ovalbumin protein, which has a molecular weight of 42.7 kDa, almost twice that of p24, reported a LOD of 20 ng/mL [83], with a minimum detectable shift of around 15 pm. This, together with the fact that the sensitivity of the waveguides employed in those experiments was around 10 times higher, gives us an indication on why antigen p24 results hardly detectable in the present conditions. Besides, Figure 4.1 shows that, assuming an average K of 10^{-7} M, the surface coverage for p24 concentration approaching the ng/mL has very little variation with the

concentration. A high detection sensitivity is required in order to extend the dynamic range below the ng/mL concentration.

As far as the injection of secondary antibodies and subsequent magnetic markers is concerned, no issues related to the solution concentration need to be taken into account, as these binding events commonly take place with solutions at such high concentrations that a complete saturation of the binding sites is expected. Indeed, the dispensed solutions were in the concentration of 6.67 μM and 142 nM respectively. As regards secondary antibodies, the same considerations on the produced effect on the waveguides hold: antibodies, too, are light bio-entities with a mass of about 150 kDa, producing small wavelength shifts not detectable with the present set-up, i.e. without a microfluidic cell. Instead, an effective signal enhancement upon adding the magnetic beads has been confirmed. As already mentioned in Section 2.1, the dissociation constant for the binding of streptavidin to biotin is very low (10^{-14} M), which corresponds to a 10^{-12} M minimum dispensed concentration for total surface coverage (from Equation 2.2 and Figure 2.2, [A] should be about 2 orders of magnitude larger than K) and to a time constant of the order of hundreds of seconds. If we use Equation 2.7 to estimate the binding time with $K = 10^{-14}$ M, $k_{on} = 10^5$ M^{-1}s^{-1} and $[A] = 142$ nM, a value of around 70 s is obtained. However, in this case two considerations must be made: first, the effective dissociation constant for streptavidin-biotin binding dynamics in this system is expected to be bigger than the assumed value, due to the fact that streptavidin molecules are not free, but bound to massive magnetic beads; second, for such particles diffusion plays a significant role in the system kinetics. For these reasons, larger overall binding times are expected. Previous experiments performed on a similar system involving hybridization of streptavidin-coated beads and immobilized biotinylated biochemical targets show that the typical time for the reaction to be complete is around $25 - 30$ minutes. As a matter of

fact, the curves acquired in the present assay show that signal saturation is reached after the same amount of time. Afterwards, measurements should be stopped in order to limit the amount of unwanted beads sedimentation that introduces spurious contributions to the signal.

4.1.2 Procedure

In order to carry out the experiments, first the chip is placed on the holder, the optical fibers are properly aligned with the *in* and *out* ports of the optical chip. Note that in these experiments a microfluidic cell is not used, due to the peculiar geometry of the optical chips, with the ring resonators at the end of the chips. This means that the fluids are manually dispensed on the chip contained in a macroscopic well and the optical fibers for the input and output connections are immersed in the fluid. That procedure is affected by a lot of sources of mechanical and optical instabilities giving rise to an effective signal noise associated to spurious fluctuations of the resonance frequency.

The transmission spectrum is acquired as a baseline reference for later resonance wavelength shift calculation coming from subsequently obtained spectra.

The chip is exposed to an antigen solution, and for two hours (i.e. the time required for complete hybridization of the virus with the antibody-coated chip surface) optical power spectra for the different sensitive micro-rings are continuously acquired to monitor the behaviour of the resonance in time. After a proper washing step, a solution of secondary antibodies is injected and spectra are acquired and saved for one hour. Finally, after another washing step, the solution of 150 nm magnetic beads is introduced onto the sensor surface, spectra are acquired for 30 minutes and then measurements are stopped and the surface is cleaned.

As already mentioned, signals from antigen and antibody pre-labelling steps are not distinguishable, mainly because of the fluctuations associated to the lack of a suitable microfluidic cell, while the addition of nanoparticles results in a successfully detectable biorecognition assay. Spectra are acquired continuously in real-time for 30 minutes upon adding the beads, and the variation of resonance shift over time is calculated with respect to a baseline spectrum acquired just before beads injection. The outcome of a typical assay is reported in Figure 4.2. Resonance shifts obtained from the real-time acquired
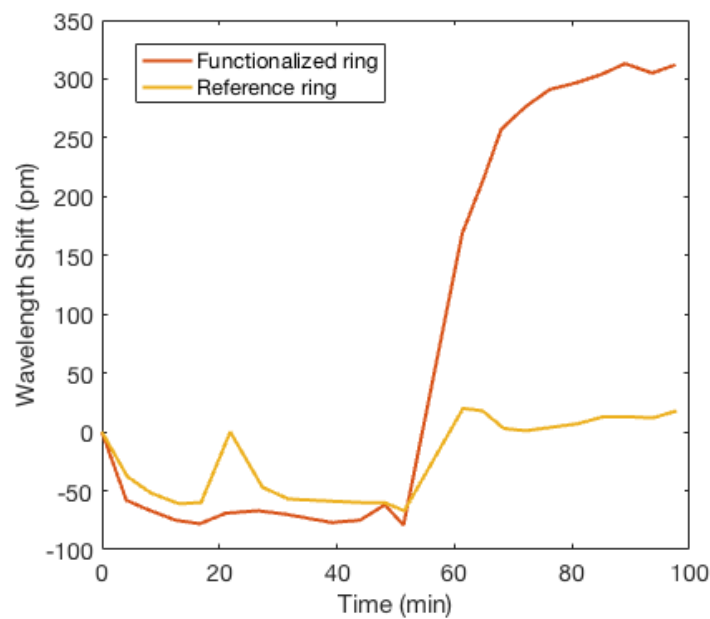
Figure 4.2: Calculated resonance shifts due to the addition of 150 nm nanoparticles as a function of time on a chip with a ring hybridized with 100 ng/mL of p24 (4.17 nM).

spectra are computed for a ring hybridized with 100 ng/mL of p24 and for a plain reference ring without functionalization. In this example, also the monitoring of the addition of secondary antibodies is shown: time 0 represents the moment of injection of the antibody solution, followed by a short negative shift transient experienced by both rings which is due to the lower temperature

of the solution with respect to the reactive surface. The sudden peak observed in the reference ring after about 25 minutes can be attributed to temporary instabilities in the laser system. The plot shows that the signal from the binding of secondary antibodies is not detected, while upon adding the beads (minute 55) the signal coming from the hybridized ring experiences a sudden big enhancement that reflects the exponential behaviour discussed in Section 2.1.2. When the beads are dispensed, also the reference ring experiences a resonance shift, but this contribution comes from the injection of the new buffer solution which causes a change of temperature and local refractive index; apart from this, its signal remains stable, which confirms the low sedimentation expected for 150 nm diameter nanoparticles.

It is also important to state that the dimension of the beads influences the outcome of the assay: indeed, small particles must be preferred to avoid sedimentation and thus the spurious contribution of false positives and to reduce steric hindrances that impact the binding efficiency; however, the reduced volume of the particles results in a lower signal enhancement.

For a further confirmation of negligible sedimentation and effective binding of the particles, the chips were observed with an optical microscope and an estimate of the number of beads per unit area was made. Figure 4.3 presents the two measured rings with fluorescent 150 nm beads after the washing step in PBS solution. Because of the difficulty in counting the beads positioned exactly on the thin micro-ring waveguides, the more evident pale area on the edge of the resonator was examined, corresponding to an area of 37x37 pixel. A colour threshold was chosen such that impurities, surface defects and spurious elements were left out and only the presence of the beads was revealed. The pixel dimension is 0.27x0.27 μm^2, and due to the fact that the dimension of the pixel and that of a 150 nm diameter bead are compatible, one black pixel is taken as a single bead. In such a way, a beads average density of 4
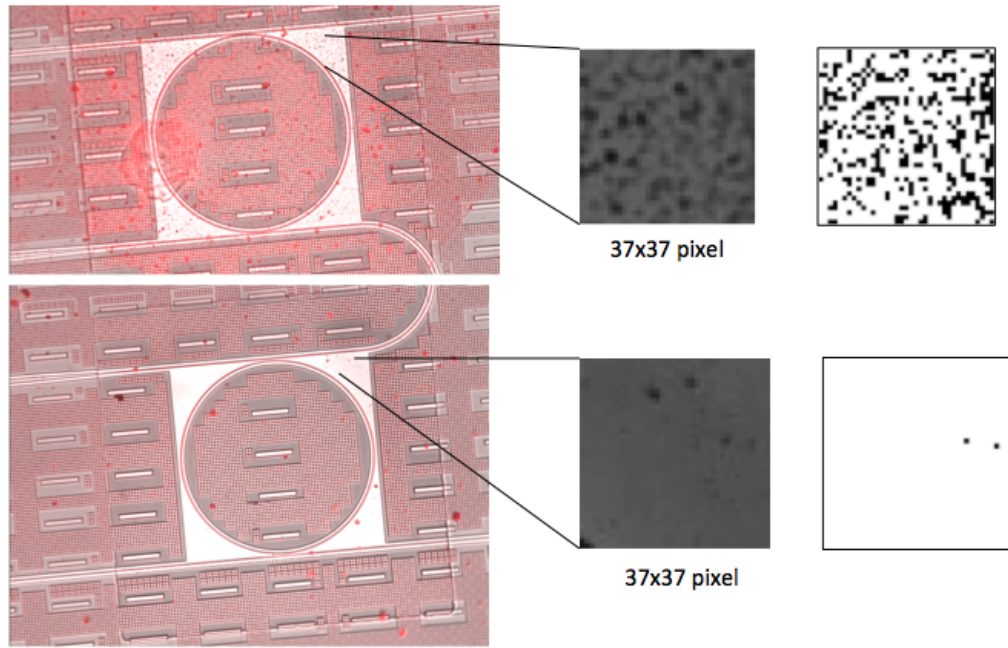
Figure 4.3: Functionalized (top) and plain reference (bottom) rings and the considered areas for bead density calculation.

particles/μm^2 was obtained for the ring hybridized with a p24 concentration of 100 ng/mL, and 0.03 particles/μm^2 for the reference one. The large difference in the computed densities in the two areas confirms the negligible sedimentation. If we want to compare the number of bound beads to the number of sandwich structures on the ring area, by considering a functionalized single ring area of $S \sim 45 \cdot 10^3$ μm^2, a number of $1.75 \cdot 10^5$ particles is obtained. Taking the previously obtained surface density of $\sigma_{lim} \sim 6.67 \cdot 10^{-11}$ moles/m^2, we have $1.81 \cdot 10^6$ antibodies. The difference in these values has to be evaluated accounting for a few considerations. First, the number of the bound biological targets has been computed assuming that at equilibrium total surface coverage with respect to the available binding sites has been reached by both p24 and the secondary antibodies, but Figure 4.1 clearly shows that, for the considered possible dissociation constants, in the 10^{-7} g/mL region the surface coverage

is only around 50%. Besides, the size of the magnetic particles is 150 nm in diameter, and this value is below the resolution of the microscope, which means that for every pixel revealing the presence of particles there may be more than a single bead. Finally, nanoparticles are coated with many streptavidin molecules, therefore they feature more than one binding site for biotin and can in principle bind to more than one biotinylated antibody.

4.1.3 Calibration curve

From these results, it is possible to infer that the bioassay performed on the p24 sandwich structure becomes feasible with our set-up, i.e. without microfluidic cell, only by adding nanoparticles, which are responsible for a significant signal enhancement in terms of resonance shift. Besides, the outcome of the experiments makes a quantitative assay possible in terms of the collection of resonance shifts produced by beads binding to different sandwich concentrations, in turn determined by the antigen first-injected concentrations. For this purpose, beads resonance shifts generated from different antigen concentrations are acquired and a calibration curve is built displaying resonance shifts as a function of antigen concentration. The curve, reported in Figure 4.4, is obtained by considering as the final shift the one reached by the system after 30 minutes from beads injection, because this is the time for correct complete beads hybridization, as discussed above. For each concentration $(0 - 2.5 - 10 - 20 - 50$ ng/mL), the signals resulting from the plain rings are also acquired and the resonance shift in the calibration curve is calculated as the difference between the shift from the functionalized ring and the reference at the end of the assay. A shift of 494 pm is acquired for the highest analyzed concentration (50 ng/mL), and drops down to a value of 121 pm for the lowest analyzed concentration (2.5 ng/mL). The error bars are computed by considering the sum of the maximum fluctuations of the signal from the functionalized ring
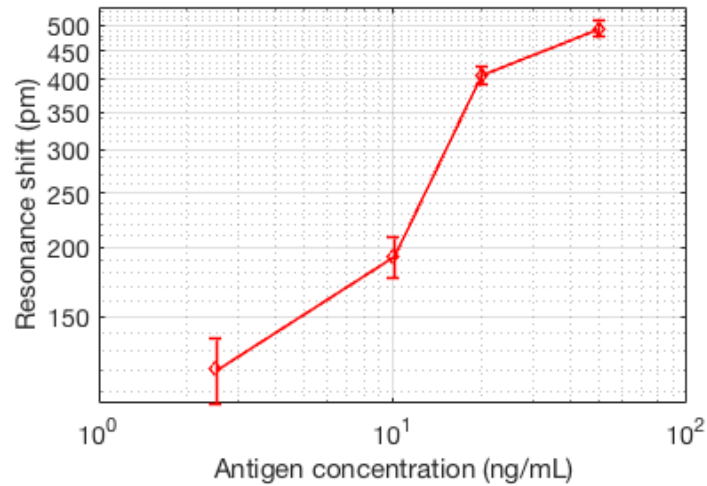
Figure 4.4: Calibration curve displaying the computed resonance wavelength shifts as a function of p24 concentration.

and from the reference ring. The experimental determination of the limit of detection of this platform for this sandwich assay requires further investigations for even lower concentrations: the LOD will be given by the concentration at which the calibration curve intersects the abscissa. Nevertheless, the shape of the calibration curve is very similar to that expected from the Langmuir isotherm. The experimental shift follows the theoretical trend for the surface coverage (see Figure 4.1) for a dissociation constant of 10^{-7} M, with a clear deviation from the linear regime below a concentration of 10 ng/mL, even if the computed error margin does not allow to take this as a certain fact, for the time being.

In order to perform investigations on even smaller concentrations, a more effective binding and measurement protocol needs to be adopted. This can be obtained with the employment of a microfluidic cell, which allows to enhance binding efficiency by exposing the reactive surface to a constant and continuous flux of analytes. Furthermore, the microfluidic cell is essential to reduce spurious fluctuations of the measurement conditions which are, at

present, the major limitation to reach low limits of detection. Nevertheless, the reported experimental data acquired at present conditions clearly demonstrate that detectable signals are reached for concentrations on the order of the LOD reached in many similar works in literature discussed in Section 2.4.1.2 which very often employ a microfluidic system. This indicates that our platform and bioassay scheme presents biological sensitivities comparable to the state of the art of micro-ring resonators exploiting passive nanoparticles enhancement.

As regards the choice of the nanoparticles employed for the experiments, in principle any streptavidin-coated particle with a different refractive index with respect to water would be eligible for signal enhancement in this kind of bioassay. Indeed, the magnetic properties of the beads are not exploited. However magnetic properties become important in the analyses performed with another kind of approach, described in the next Section. In this perspective, the use of magnetic particles also in the first approach is functional for performing bioassays that combine the two detection methods.

In the bioassays reported above, a real-time monitoring of the signal was carried out, and this allows on one hand to evaluate the correlation between resonance wavelength shifts and the binding dynamics, but on the other hand turns out to be time consuming, which would be impractical in a real study case. Besides, making sure that the detected signals arise from effective binding events instead of other spurious contributions (thermal drifts, instabilities in the optical alignments, beads sedimentation etc.) in realistic contexts is highly demanding, and this constitutes a severe limitation for real on-site applications. For this reason, the following Section presents a different and more robust detection strategy, which combines the use of biosensitive waveguides and magnetic actuation of nanoparticles. This approach allows to get rid of the

contributions of spurious shifts in real-time measurements through an on-off-like detection.

4.2 Opto-magnetic detection of DNA recognition

4.2.1 Procedure

The opto-magnetic technique allows for the quantification of biomolecular recognition events at the surface of ring resonators. We thus assume that all the biochemical reactions needed for the recognition have been fully accomplished, including washing, thus leaving on the chip surface some magnetic beads bound to the target-analyte complexes after recognition. The transmission spectrum of the selected micro-ring is acquired in order to determine the position of the various resonances, and one of them is chosen as a reference for the measurements. The laser is tuned to the wavelength corresponding to the maximum slope of the notch resonance shape, which is usually located about 5 dBm below the flat region of the spectrum. Once the electromagnet has been carefully positioned in the correct area below the active micro-rings of the chip, it is fed with a sinusoidal current signal with amplitude of 2 A generated by a current generator driven by the lock-in amplifier. The response signal extracted from the electronics combines the photodiode output, set to return 1 V when the optical power corresponds to -30 dBm, and the voltage driving the electromagnet, set to 2.5 V in order to provide a current of 2 A. The driving frequency can be varied freely to investigate the frequency response of the system. As already mentioned in Chapter 3, the optimum oscillation frequency should be chosen in order to maximize the response of magnetic nanoparticles immersed in the AC magnetic field. The force driving the beads

is proportional to the magnetic susceptibility, so in principle one should directly refer to the frequency response of χ. However, in these conditions the beads cannot freely rotate, because they are bound to DNA double strands through streptavidin molecules they are coated with. This will increase the effective viscosity experienced by such particles, therefore we can suppose that in this case $\chi'(\omega)$ and $\chi''(\omega)$ curves (see Section 2.3.4) are slightly shifted towards the lower frequencies side, because the frequency of the peak of $\chi''(\omega)$, assumed to coincide with the Brownian relaxation frequency $f_B = \frac{k_B T}{6\pi\eta V_h}$, will be lower for higher viscosity. For a typical bead of 250 nm diameter, the Brownian relaxation frequency is on the order of 10 Hz [84], but in the present case we expect a much lower relaxation frequency, because the beads cannot freely rotate. This means that, avoiding unpractical frequencies of modulation below a few Hz, the magnetic susceptibility is supposed to decrease when increasing the excitation frequency. Nevertheless, the presence of $1/f$ electronic noise sets a limitation to the effective lower limit of suitable driving frequencies. Furthermore, the frequency dependence of the opto-magnetic signal will also be determined by the frequency response of the mechanical system made of the magnetic bead and the DNA double strand, which could present a resonance at higher frequency. In order to preserve a sufficient value of the signal-to-noise ratio, a value of 10 Hz for preliminary investigations was chosen as a good compromise. A more detailed analysis of the output signal at various frequencies is reported in Section 4.2.3

The working frequencies, especially the low ones, require output signals to be subjected to a filter of amplitude of 0.1 Hz or narrower, in order to leave out as much noise as possible. Such a constraint sets a minimum value for measurement times, which have to be of the order of 10 s or longer. A frequency of $f_d = 2f_0$, f_0 being the modulating frequency, is used for signal demodulation, to acquire the response coming from the magnetic actuation of the nano-sized

beads which, being proportional to ∇H^2, oscillate at a frequency that is double with respect to the driving frequency, as explained in Section 2.4.2.2.

4.2.2 On-off signals

One of the advantages of the opto-magnetic detection technique is that it offers the possibility to return a signal only when magnetic field is applied. This leads to a significant reduction in the measurement times, which can be of the order of a few seconds, with respect to higher times required by other existing configurations.
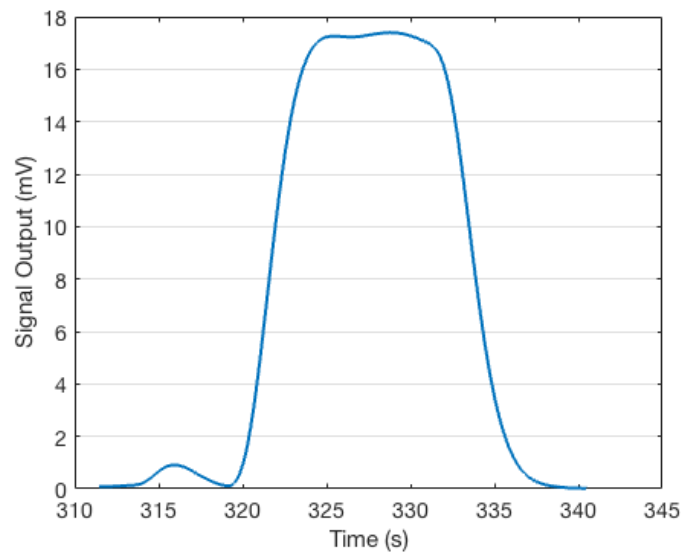
Figure 4.5: Typical on-off signal acquired with the opto-magnetic platform (100 nM DNA, 130 nm beads).

An example of an on-off signal is shown in Figure 4.5. Whenever the magnetic field is turned on, the presence of magnetic particles bound to biological samples is recognized, and the information is transduced into a measurable signal, well distinguished from the average noise in the background, while as soon as the magnetic field is turned off it quickly drops to zero. This specific case

refs to 130 nm diameter beads bound to DNA strands previously hybridized on the sensor surface with a concentration of 100 nM.

This signal, filtered at 0.1 Hz, displays a computed signal-to-noise ratio of 35.42 dB. This specific example of signal is acquired at a working frequency of $f_0 = 10$ Hz and demodulated at $2f_0 = 20$ Hz, but, as explained later, detectable signals can be collected at many frequencies up to the cut-off. The latter depends, for a specific biological entity, on the size of the beads and their binding capacity. Of course, high-frequency cut-offs allow for better filtering of the $1/f$ noise, thus improving the sensitivity.

4.2.2.1 Comparison between electromagnets

This section presents the results obtained from testing the newly designed electromagnet with a bottle-neck shaped iron core, with respect to the old one. On-off signals were acquired with the different electromagnets one after the other on the same chip in the same conditions in terms of positioning. Voltage supply through the lock-in device is set to a value such that the generated magnetic fields on the chip were equal. To achieve this condition, a higher input current (2.6 A) is required for the old electromagnet, with respect to the new one (2 A). Signals from the same micro-ring are compared. The results obtained from this kind of comparison from a concentration of 10 nM DNA target single strands actuating 130 nm beads at 10 Hz are plotted in Figure 4.6.

From simulations presented in Section 3.1.2, it results that potential improvement of the spatial gradient of H^2 could be up to at least one order of magnitude in close proximity to the top surface of the magnet. However, the magnitude of the gradient rapidly falls with increasing distance from the top surface. Due to the restrictions imposed by the present measurement set-up, which includes the intrinsic thickness of the chip and, especially, the
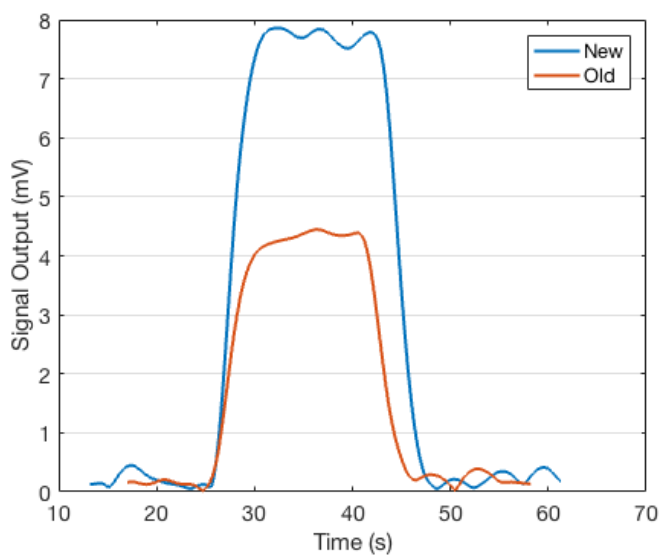
Figure 4.6: Comparison between demodulated signals generated by the exploitation of the new design of the electromagnet and the old one on a sample of 10 nM DNA concentration and 130 nm beads.

non-minimized thickness of the available PMMA holder, the improvement of the output signal is just by a factor two.

4.2.3 Frequency response

Another interesting quantitative assay regards the frequency behaviour of the opto-magnetic output signal. Such an experimental response depends on the viscosity of the buffer, on the geometric packing of the ensemble of DNA-bead compounds and on the stiffness it displays.

First of all, a discussion about the magnetic beads dynamics in the system at our disposal should be made, recalling the theoretical considerations presented in Section 2.4.2.2. The particles that are used in these experiments have a diameter on the order of hundreds of nanometers, and as such are much larger in size than DNA, which is about 20 nm long and 2 nm wide. From technical data sheets of the utilized beads (Micromod Nanomag-D) it is possible to get

the average number of streptavidin molecules per magnetic particle. We will focus on considerations regarding two specific kinds of beads, which are different in size: beads of diameter of 250 nm have an average number of streptavidin sites of 475 per magnetic particle, whereas this value falls to 65 for 130 nm ones. If we take as a rough estimate the radius of the contact surface of a bead to be around one fourth of its total radius, this leads to an approximated number of 8 biotinylated DNA molecules bound to each bead for 250 nm particles, and 1 for 130 nm ones[1]. Detailed computations of the elastic behaviour of DNA molecules requires specific models and appropriate simulations, however we can make some simple estimates to build a realistic picture of our system. Because within the context of the already mentioned WLC model (see Section 2.4.2.2) DNA strands can be considered as stiff springs (their length being smaller than the persistence length), the mechanical system on a microscopic scale consists of a multiplicity of beads, each of which lies on top of a certain number of stiff parallel 20 nm-long rods. As a consequence, the beads are subjected to spatial displacement because they tilt together with DNA strands, rather than because DNA molecules behave as actual springs.

An example of the obtained results is plotted in Figure 4.7 where the signal response of 250 nm beads at different frequencies of the magnetic field acquired with a 1 Hz filter is reported.

Interpreting these results is possible by recalling the mass-spring model for the DNA-bead complex examined in Section 2.4.2.2. The model describes the oscillating dynamics of the bead under the influence of the AC magnetic field when it is attached to a DNA strand bending back and forth that can be represented by an effective elastic spring. The stationary solution to the equation of motion is $A_p = \tilde{A}(\omega_F) \sin(\omega_F t + \phi)$, where the amplitude $\tilde{A}(\omega_F)$ is

---

[1]In this calculation, the possibility for streptavidin to display multiple binding sites for biotin has not been taken into account, however, in this case the number of DNA molecules that can bind to a single bead is even higher.
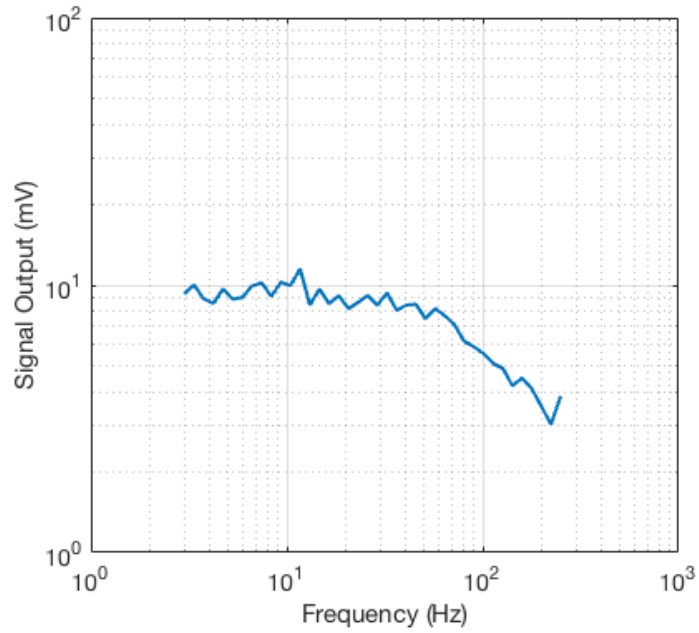
Figure 4.7: Signal trend as a function of frequency generated by a ring of 10 nM of DNA actuating 250 nm beads.

given by

$$\tilde{A}(\omega_F) = \frac{\frac{F_0}{m}}{\sqrt{\left(\frac{k}{m} - \omega_F^2\right)^2 + \gamma^2\omega_F^2}}$$

This quantity represents in the opto-magnetic assay the maximum extension of the oscillation of the beads, therefore it is closely related to the frequency response of the system. A low-pass filter behaviour is expected for sizable damping and, as a matter of fact, experimental data show no resonance peak at all, thus confirming that the oscillator is overdamped. We can compare this quantity with the reported experimental data in order to obtain from the fitting an estimate of the effective elastic constant k. The analytical computation of the various quantities that appear within the expression of $\tilde{A}(\omega_F)$ can begin by calculating the magnetic force. Recalling Equation 2.55, we need values for the susceptibility of the beads, their volume and the gradient of the square of the magnetic field: χ is extracted from the magnetization curve of the beads from

the vibrating sample magnetometer, and a value of $\chi = 2.4$ for 250 nm particles is obtained. The bead volume is easily computed from the diameter dimension, considering a spherical shape, and it is equal to $8.18 \cdot 10^{-21}$ m^3; regarding ∇H^2, a value of 10^{10} A^2/m^3 is chosen from experimental data considering the effective average distance of the beads from the electromagnet. Inserting these values in Equation 2.55, a magnetic force $F_{magn} = 1.233 \cdot 10^{-16}$ N results. This value is computed with the low-frequency magnetic susceptibility, however a more correct expression should consider the frequency dependence of χ as

$$F(\omega_F) = F_0 \frac{\chi(\omega_F)}{\chi_0} \tag{4.1}$$

where χ_0 is the DC magnetic susceptibility used in the computations above.

The mass of a bead is equal to $2.04 \cdot 10^{-17}$ kg and the damping coefficient introduced in Section 2.4.2.2 is $\gamma = 6\pi\eta r/2m = 5.9 \cdot 10^7$ s^{-1} for a fluid viscosity $\eta = 0.001$ Pa·s.

The signal amplitude at low frequencies depends, with reference to $\tilde{A}(\omega_F)$ in our model, on the magnetic force (directly related to the particle magnetic susceptibility), and on the k/m ratio. Physically speaking, also the analyte concentration, the bead volumetric fraction that is able to interact with the evanescent field tail and the shape of the notch resonator spectrum play a role in determining the measured signal amplitude. However, the measured values also depend on the specific transfer function of the whole system, which is why a quantitative prediction of the exact amplitude value is complicated to achieve, and only considerations about its relative variations with varying known parameters can be made. A qualitative comparison between the trend of the experimental signal frequency response and the obtained expression for $\tilde{A}(\omega_F)$ (normalized in amplitude) is reported in Figure 4.8.

The value of the effective elastic constant can in principle be extracted from the pole frequency of the fitting function. If we consider for damping coefficient the given expression $\gamma = 6\pi\eta r/2m$, a rough estimate of $k = 5.71 \cdot 10^{-7}$ N/m
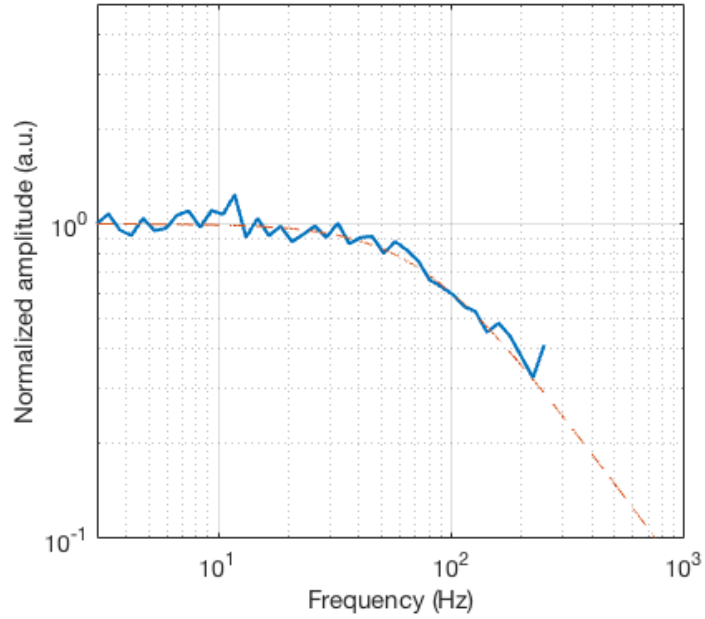
Figure 4.8: Comparison between the normalized experimental data as a function of frequency and fitting low-pass-filter-like function. From the fit, an estimate of the effective elastic constant can be extracted.

can be obtained. However, the considered γ describes damping phenomena undergone by free particles, but our system consists of DNA-bead complexes attached to the sensor surface, thus a physical quantitative evaluation of the damping is not straightforward. Of course, this reflects in the uncertainty on the k value estimated above. Another possible approach can consist in employing simulations of the average displacement Δz of the beads on top of DNA strands when subjected to the sinusoidal force. In this case, for high bead surface coverage (which corresponds to DNA concentrations of about 100 nM) an average displacement of 80 pm has been obtained, yielding to an elastic constant $k = \frac{F}{\Delta z} = 1.5 \cdot 10^{-6}$ N/m [85]. Such a theoretical derivation can allow for an estimate of the damping coefficient γ from the fitting of experimental values. Note that the values of the effective elastic constants derived from the two approaches just differ by a factor 3. This means that the rough model

presented above is not unrealistic and can be used at least for qualitative interpretation of the experimental data.

During this thesis work, the focus was on the optimization of the signal, therefore a comparison between values extracted in different conditions is presented in the following. In particular we consider two factors: the quality factor that characterizes the employed micro-ring resonator and the size of the magnetically actuated beads. Both studies are reported in the following sections, and the final conclusions will offer the possibility of plotting a calibration curve.

4.2.3.1 Rings with different Q factor
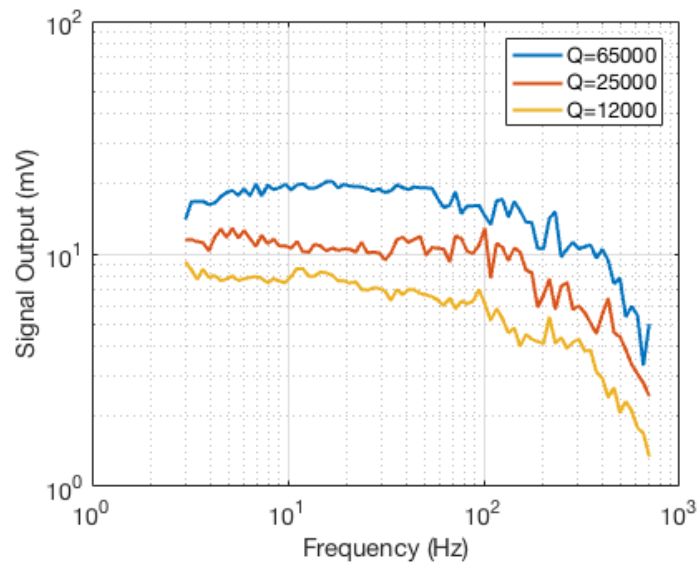
Figure 4.9: Signals generated by 100 nM DNA initial solution and 130 nm beads on rings with different quality factor.

Figure 4.9 shows the different experimental plots of the frequency behaviour of the signal from micro-rings with different Q_{factor} for beads of 130 nm at a concentration of 100 nM. As already discussed in Section 2.4.2.1, if the magnetic field oscillates at a frequency ω_0, the applied force will in turn oscillate at $\omega_F = 2\omega_0$. As a consequence, the transmitted optical intensity

within the resonator will oscillate at ω_F due to the periodical perturbation of the refractive index and resonance wavelength. The variation of the intensity can be expressed in terms of the series expansion with respect to λ, considering the first order term to a first approximation:

$$\Delta I(\lambda_0) \simeq \left(\frac{\partial I}{\partial \lambda}\right)_{\lambda_0} \Delta\lambda(2\omega_0)$$

Therefore, it is evident that the shape of the power spectrum of a micro-ring
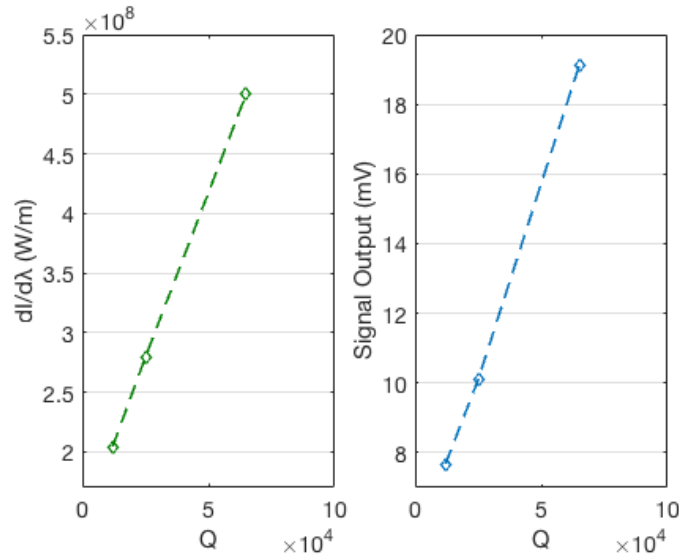
Figure 4.10: Comparison between the increment of the slope of the resonator notch with respect to Q (on the left), and the increment in the measured signal at 10 Hz from 100 nM DNA and 130 nm beads on rings with different Q.

deeply influences the acquired signal. Indeed, the variation of the intensity is directly proportional to the first derivative of the spectrum at the considered λ, which is for this reason chosen as the wavelength corresponding to the steepest point of the resonator notch, usually around -5 dBm from the flat region. The quality factor quantifies the sharpness of the resonance, so it is directly related to the magnitude of the derivative of the notch. From experimental optical spectra of the different used resonators, the values of the first derivative at -5

dBm from the flat region of the used notch around $\lambda \sim 1550$ nm for rings with $Q = 65000$, 25000 and 12000 can be computed. It turns out (Figure 4.10) that the ratio between the experimental signals from different resonators is reflected by the ratio between the derivatives of the corresponding spectra calculated in the same position on the notch, and in our case is equal to 1.37. These data confirm the proportionality between the output signal and the intensity derivatives and that high-Q micro-rings should be preferred for better detection.

4.2.3.2 Beads of different sizes

The characteristics of the magnetic particles used in the experiments deeply influence the final output signal, and they can be different not only in size, but also in magnetic properties. In order to make quantitative comparisons between different kinds of beads, experiments were made employing those with 250 and 130 nm diameter. The resulting signals, both for a DNA concentration of 10 nM and on the high-Q ring resonator ($Q = 65000$) are reported in Figure 4.11

As it can be noticed from the image, signals from small magnetic beads result in a larger amplitude and a higher pole frequency. As regards a physical interpretation of the increase in signal amplitude, if we evaluate the amplitude dependences from the formula, we notice that for $\omega_F \to 0$, $\tilde{A}(\omega_F) \to F_0/k$. The force on a 250 nm magnetic bead has been already computed above, and it is $F_{magn} = 1.23 \cdot 10^{-16}$ N. Using for 130 nm particles a volume of $1.15 \cdot 10^{-21}$ m^3 and a magnetic susceptibility $\chi = 3.9$ extracted from VSM data, the magnetic force results $F_{magn} = 2.82 \cdot 10^{-17}$ N. This value is about 5 times smaller than that of 250 nm particles. As regards the effective elastic constant, we cannot use the fitting method presented above to extract reliable values of the elastic constants for 130 nm and 250 nm beads, mainly because k from the fit strongly depends on the damping parameter, that we do not know with enough accuracy.
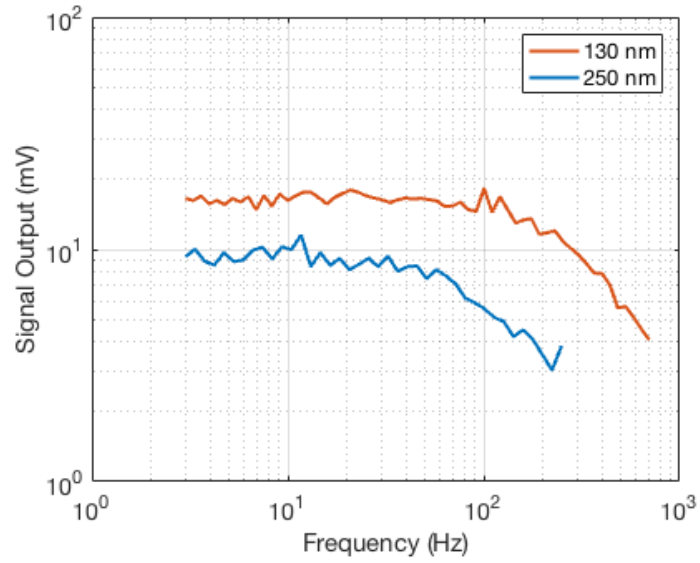
Figure 4.11: Plots of acquired outputs from 250 and 130 nm beads on a 10 nM surface of DNA. The signals generated by smaller beads feature a higher value of the pole frequency and also a higher amplitude.

For this reason, we prefer to estimate the ratio between the k values for the two particle sizes, just considering the ratio between DNA molecules binding the bead to the surface. As explained above, this number is 1 for 130 nm and 8 for 250 nm beads. Assuming that the effective elastic constant is proportional to the number of DNA molecules bound to the bead, we can say that $k_{250} = 8k_{130}$. As summarized in Table 4.1 below, the A/k ratio, which is proportional to the amplitude of the oscillation in our simple model, for 130 nm particles is about twice larger than that of 250 nm ones.

Diameter	χ	F_0	k_{estim}	$A_0 = F_0/k_{estim}$
130 nm	3.9	$2.82 \cdot 10^{-17}$ N	k_0	$2.82 \cdot 10^{-17}/k_0$ m
250 nm	2.4	$1.23 \cdot 10^{-16}$ N	$8k_0$	$1.23 \cdot 10^{-16}/8k_0$ m

Table 4.1: Main parameters for 250 and 130 nm beads

As 250 nm particles are about twice as big as 130 nm ones, the overall volumetric fraction of the surface layer where a sizable evanescent wave exists (with thickness on the order of $\lambda = 1.55$ μm in our case) is almost the same for a monolayer of beads. We can thus conclude that the estimate of the low-frequency amplitude of the oscillation arising from Table 4.1 should correctly capture the main physics of our system. Indeed, the experimental ratio between the amplitudes at 10 Hz for 130 nm and 250 nm beads is on the order of 1.8, very close to that estimated in Table 4.1.

The quantitative explanation of the shift of the frequency corner to higher frequency for 130 nm is more difficult, the main reason being the fact that the exact position of the corner depends both on the damping coefficient γ and on the elastic constant k, which are not well known. On the other hand, we cannot forget that also the susceptibility of magnetic beads has a well defined frequency behaviour which impacts on the applied force and thus on the signal frequency response. The frequency dependent bead susceptibility has been discussed in Section 2.3.4, and for magnetic particles bigger than 50 nm the trend is mainly governed by Brownian relaxation, having a characteristic frequency of $f_B = k_B T / 6\pi \eta V_h$. Previous works on the experimental evaluation of the Brownian relaxation frequency of free particles of different sizes reported that f_B for particles of 130 nm is about 7 times larger than that of 250 nm ones [84]. This can be regarded as another possible contribution to the higher pole for 130 nm beads. As mentioned above, a more refined model is required in order to correctly interpret the signal frequency behaviour. Nevertheless, the extension of the flat region up to 100 Hz for 130 nm beads is extremely advantageous for our purposes because it allows to acquire detectable signals at higher frequencies with a lower contribution from the $1/f$ electronic noise.

4.2.4 Calibration curve

The examination of all the mentioned parameters that play a role in determining the amplitude of the detected signal naturally leads to the possibility of a real biosensing test that comprises detection and quantification of analytes. Once the problems regarding the choice of optimum gradient spatial profile, resonator spectrum, bead size and characteristics have been sorted out, measurements on the final system can be carried out employing different concentrations of hybridized analytes. In our case solutions of complementary DNA molecules
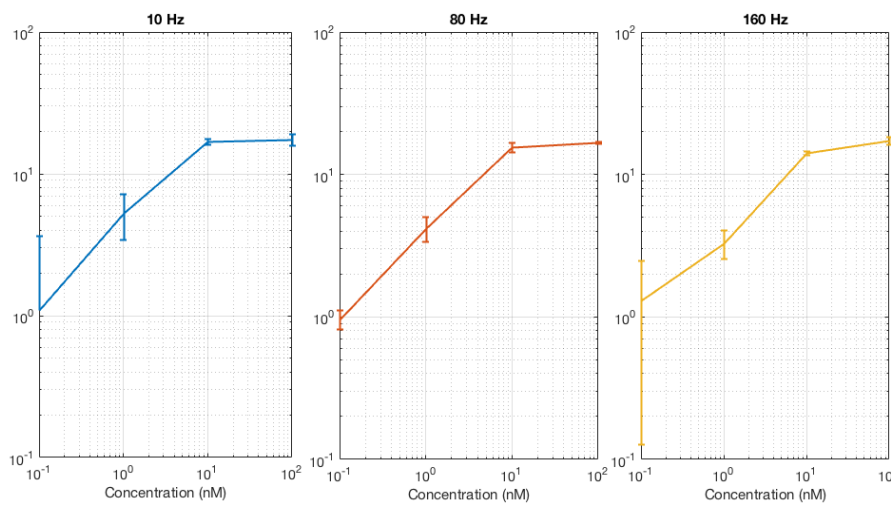
Figure 4.12: Calibration curves at different frequencies of signals obtained with the opto-magnetic platform.

are dispensed on the microchip coated with a layer of biotinylated DNA single strands, and afterwards biotin sites are occupied by inserting magnetic beads. Obtained experimental data are plotted in Figure 4.12.

The feasibility of these measurements with the opto-magnetic platform has been investigated acquiring calibration curves at different frequencies. Data are acquired from on-off signals employing a narrow filter of 0.1 Hz for more precise and reliable measured output signals. The image also reports the relative error

bars: errors are evaluated considering the sum of the maximum variations of the "on" signal when the magnetic field is switched on and that of the "off" signal. Errors can become significant when detecting pM concentrations, however data
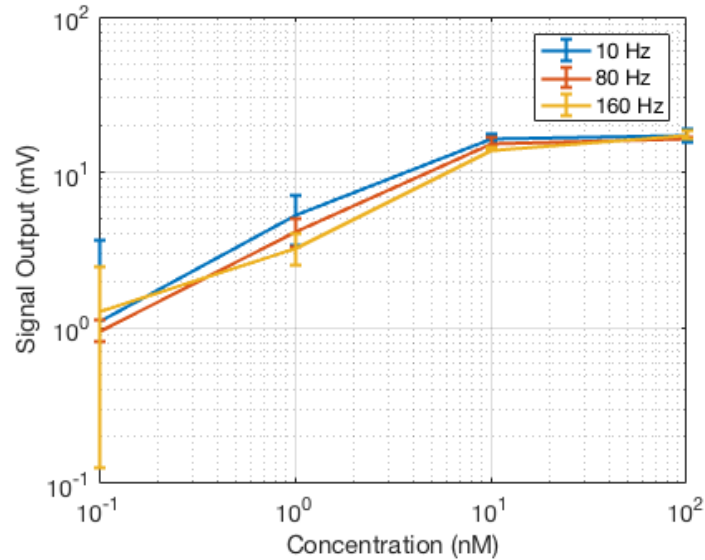
Figure 4.13: Congruency between signals acquired at different frequencies.

at 80 Hz present low error estimates for all examined concentrations. Such data confirm the possibility of reliable detection of concentrations down to 100 pM, and Figure 4.13 shows the mutual correspondence between signals acquired at different frequencies. Detection of smaller concentrations in these conditions requires further investigations and an optimized hybridization protocol with a microfluidic cell.

Determining the precise dynamics that characterize the DNA-bead complex on a micrometer scale is not straightforward and would require a detailed theoretical analysis, possibly combined with the appropriate simulations. This would allow for a deeper insight on the mechanical phenomena that take place not only considering the beads as single entities, but also accounting for the collective behaviour involving all the particles as a compact ensemble.

Conclusions

This thesis work was focussed on the purpose of investigating and describing the operation and the performances of a biosensing method based on the combination of integrated optics sensing technology and magnetic nanoparticles used as passive and active labels.

Passive magnetic labels have been used to enhance the refractive index change at the surface of ring resonators upon recognition of target molecules. A significant signal enhancement and the almost total rejection of false positives was achieved. This increase in sensitivity and robustness enabled successful biorecognition measurements exploiting the immunosensing sandwich assay of HIV antigen p24 between two antibodies.

Active labels were exploited in the opto-magnetic platform, which was appropriately optimized in terms of:

i) the generated AC magnetic field;

ii) the physical characteristics of the sensitive micro-ring resonators (Q-factor);

iii) the magnetic beads (size).

Reliable signals have been recorded in case of DNA recognition for concentrations down to the pM range.

The possibility to employ the same magnetic particles as passive and active labels in two different phases of the assay was studied. While the "passive" mode allows for monitoring the kinetics of biomolecular recognition, it requires

stable condition of operation during the assay duration, as any fluctuation could alter the quantification process based on the measurement of the signal variation with respect to a given base-line. The "active" opto-magnetic mode, instead, does not require a sinchronous quantification with the recognition and results much more insensitive to disturbances. This comes with a very short assay duration, since continuous monitoring of the resonance shift in time is not required. Furthermore, this approach enables multiplexing strategies, consisting in performing assays on various analytes on the same device at the same time. This could be achieved by employing different types of labels, with distinct frequency response that could be used to disentangle the signal coming from beads labelling different targets.

Even if some preliminary calibration curves in both biosensing schemes have been provided, our experiments have confirmed that the limit of detection can be further reduced by adopting for biochemical hybridization a suitable microfluidic system. It would allow to define an optimized flow rate and stable measurement conditions ensuring a better binding efficiency and lower noise, which becomes important in the case of small concentrations starting from the the pM range. Finally, further improvements in the efficiency and flexibility of the opto-magnetic platform require to extend the technique to other types of biomolecules and biochemical complexes.

Bibliography

[1] S. Chung, A. Hoffmann, S. Bader, C. Liu, B. Kay, L. Makowski, and L. Chen, "Biological sensors based on brownian relaxation of magnetic nanoparticles," *Applied physics letters*, vol. 85, no. 14, pp. 2971–2973, 2004.

[2] A. N. Nordin, "Optical-resonator-based biosensing systems: current status and future prospects," *Nanobiosensors in Disease Diagnosis*, vol. 5, pp. 41–50, 2016.

[3] R. Karlsson, A. Michaelsson, and L. Mattsson, "Kinetic analysis of monoclonal antibody-antigen interactions with a new biosensor based analytical system," *Journal of immunological methods*, vol. 145, no. 1-2, pp. 229–240, 1991.

[4] D. R. Thévenot, K. Toth, R. A. Durst, and G. S. Wilson, "Electrochemical biosensors: recommended definitions and classification," *Analytical Letters*, vol. 34, no. 5, pp. 635–659, 2001.

[5] C. S. Kumar, *Nanomaterials for biosensors.* John Wiley & Sons, 2007.

[6] C. Jianrong, M. Yuqing, H. Nongyue, W. Xiaohua, and L. Sijiao, "Nanotechnology and biosensors," *Biotechnology advances*, vol. 22, no. 7, pp. 505–518, 2004.

[7] J. Inczedy, T. Lengyel, A. M. Ure, A. Gelencsér, A. Hulanicki *et al.*, "Compendium of analytical nomenclature," *The Orange Book, 3rd Edn.*, 1998.

[8] W. Tan, L. Sabet, Y. Li, T. Yu, P. R. Klokkevold, D. T. Wong, and C.-M. Ho, "Optical protein sensor for detecting cancer markers in saliva," *Biosensors and Bioelectronics*, vol. 24, no. 2, pp. 266–271, 2008.

[9] J. Wang, "Electrochemical nucleic acid biosensors," *Analytica chimica acta*, vol. 469, no. 1, pp. 63–71, 2002.

[10] U. Yogeswaran and S.-M. Chen, "A review on the electrochemical sensors and biosensors composed of nanowires as sensing material," *Sensors*, vol. 8, no. 1, pp. 290–313, 2008.

[11] O. S. Wolfbeis, "Fiber-optic chemical sensors and biosensors," *Analytical chemistry*, vol. 80, no. 12, pp. 4269–4283, 2008.

[12] A. Leung, P. M. Shankar, and R. Mutharasan, "A review of fiber-optic biosensors," *Sensors and Actuators B: Chemical*, vol. 125, no. 2, pp. 688–703, 2007.

[13] H. Muramatsu, J. Kim, and S. Chang, "Quartz-crystal sensors for biosensing and chemical analysis," *Analytical and bioanalytical chemistry*, vol. 372, no. 2, pp. 314–321, 2002.

[14] J. Wang, "Carbon-nanotube based electrochemical biosensors: A review," *Electroanalysis: An International Journal Devoted to Fundamental and Practical Aspects of Electroanalysis*, vol. 17, no. 1, pp. 7–14, 2005.

[15] R. J. Leatherbarrow and P. R. Edwards, "Analysis of molecular recognition using optical biosensors," *Current opinion in chemical biology*, vol. 3, no. 5, pp. 544–547, 1999.

[16] J. Dostálek and W. Knoll, "Biosensors based on surface plasmon-enhanced fluorescence spectroscopy," *Biointerphases*, vol. 3, no. 3, pp. FD12–FD22, 2008.

[17] V. S.-Y. Lin, K. Motesharei, K.-P. S. Dancil, M. J. Sailor, and M. R. Ghadiri, "A porous silicon-based optical interferometric biosensor," *Science*, vol. 278, no. 5339, pp. 840–843, 1997.

[18] B. Lin, J. Pepper, B. T. Cunningham, J. Gerstenmaier, P. Li, J. Qiu, and H. Pien, "Label-free methods for performing assays using a colorimetric resonant reflectance optical biosensor," Dec. 26 2006, uS Patent 7,153,702.

[19] J. Yu, L. Ge, J. Huang, S. Wang, and S. Ge, "Microfluidic paper-based chemiluminescence biosensor for simultaneous determination of glucose and uric acid," *Lab on a Chip*, vol. 11, no. 7, pp. 1286–1291, 2011.

[20] J. Dostalek, J. Čtyrokỳ, J. Homola, E. Brynda, M. Skalskỳ, P. Nekvindova, J. Špirková, J. Škvor, and J. Schröfel, "Surface plasmon resonance biosensor based on integrated optical waveguide," *Sensors and actuators B: Chemical*, vol. 76, no. 1-3, pp. 8–12, 2001.

[21] P. Mehrotra, "Biosensors and their applications–a review," *Journal of oral biology and craniofacial research*, vol. 6, no. 2, pp. 153–159, 2016.

[22] S. L. Brooks, R. E. Ashby, A. P. Turner, M. R. Calder, and D. J. Clarke, "Development of an on-line glucose sensor for fermentation monitoring," *Biosensors*, vol. 3, no. 1, pp. 45–56, 1987.

[23] P.-C. Nien, T.-S. Tung, and K.-C. Ho, "Amperometric glucose biosensor based on entrapment of glucose oxidase in a poly (3, 4-ethylenedioxythiophene) film," *Electroanalysis: An International Journal Devoted to Fundamental and Practical Aspects of Electroanalysis*, vol. 18, no. 13-14, pp. 1408–1415, 2006.

[24] C. M. Girardin, C. Huot, M. Gonthier, and E. Delvin, "Continuous glucose monitoring: A review of biochemical perspectives and clinical use in type 1 diabetes," *Clinical biochemistry*, vol. 42, no. 3, pp. 136–142, 2009.

[25] S. Rodriguez-Mozaz, M. J. L. de Alda, M.-P. Marco, and D. Barceló, "Biosensors for environmental monitoring: A global perspective," *Talanta*, vol. 65, no. 2, pp. 291–297, 2005.

[26] S. Sharma, H. Byrne, and R. J. O'Kennedy, "Antibodies and antibody-derived analytical biosensors," *Essays in biochemistry*, vol. 60, no. 1, pp. 9–18, 2016.

[27] P. J. Conroy, S. Hearty, P. Leonard, and R. J. O?Kennedy, "Antibody production, design and use for biosensor-based applications," in *Seminars in cell & developmental biology*, vol. 20, no. 1.   Elsevier, 2009, pp. 10–26.

[28] P. Hornbeck, "Enzyme-linked immunosorbent assays," *Current protocols in immunology*, vol. 1, no. 1, pp. 2–1, 1992.

[29] C. R. Horsburgh JR, J. Jason, I. Longini JR, K. Mayer, G. Schochetman, G. Rutherford, G. SEAGE III, C. Ou, S. Holmberg, C. Schable *et al.*, "Duration of human immunodeficiency virus infection before detection of antibody," *The Lancet*, vol. 334, no. 8664, pp. 637–640, 1989.

[30] N. S. Lipman, L. R. Jackson, L. J. Trudel, and F. Weis-Garcia, "Monoclonal versus polyclonal antibodies: distinguishing characteristics, applications, and information resources," *ILAR journal*, vol. 46, no. 3, pp. 258–268, 2005.

[31] K. Maehashi, K. Matsumoto, Y. Takamura, and E. Tamiya, "Aptamer-based label-free immunosensors using carbon nanotube field-effect transistors," *Electroanalysis: An International Journal Devoted to Fundamental*

and Practical Aspects of Electroanalysis, vol. 21, no. 11, pp. 1285–1290, 2009.

[32] S. Sang, Y. Wang, Q. Feng, Y. Wei, J. Ji, and W. Zhang, "Progress of new label-free techniques for biosensors: a review," *Critical reviews in biotechnology*, vol. 36, no. 3, pp. 465–481, 2016.

[33] E. Hitt, "Label-free methods are not problem free," *Drug Discov. Devel*, vol. 7, no. 9, pp. 34–42, 2004.

[34] P. Kara, K. Kerman, D. Ozkan, B. Meric, A. Erdem, P. E. Nielsen, and M. Ozsoz, "Label-free and label based electrochemical detection of hybridization by using methylene blue and peptide nucleic acid probes at chitosan modified carbon paste electrodes," *Electroanalysis: An International Journal Devoted to Fundamental and Practical Aspects of Electroanalysis*, vol. 14, no. 24, pp. 1685–1690, 2002.

[35] M. S. Luchansky, A. L. Washburn, M. S. McClellan, and R. C. Bailey, "Sensitive on-chip detection of a protein biomarker in human serum and plasma over an extended dynamic range using silicon photonic microring resonators and sub-micron beads," *Lab on a Chip*, vol. 11, no. 12, pp. 2042–2044, 2011.

[36] L. He, M. D. Musick, S. R. Nicewarner, F. G. Salinas, S. J. Benkovic, M. J. Natan, and C. D. Keating, "Colloidal au-enhanced surface plasmon resonance for ultrasensitive detection of dna hybridization," *Journal of the American Chemical Society*, vol. 122, no. 38, pp. 9071–9077, 2000.

[37] S. Kim, J. Lee, S. J. Lee, and H. J. Lee, "Ultra-sensitive detection of ige using biofunctionalized nanoparticle-enhanced spr," *Talanta*, vol. 81, no. 4-5, pp. 1755–1759, 2010.

[38] T. Wink, S. J. van Zuilen, A. Bult, and W. P. Van Bennekom, "Liposome-mediated enhancement of the sensitivity in immunoassays of proteins and peptides in surface plasmon resonance spectrometry," *Analytical Chemistry*, vol. 70, no. 5, pp. 827–832, 1998.

[39] S. Kubitschko, J. Spinke, T. Brückner, S. Pohl, and N. Oranth, "Sensitivity enhancement of optical immunosensors with nanoparticles," *Analytical Biochemistry*, vol. 253, no. 1, pp. 112–122, 1997.

[40] C. E. Jordan, A. G. Frutos, A. J. Thiel, and R. M. Corn, "Surface plasmon resonance imaging measurements of dna hybridization adsorption and streptavidin/dna multilayer formation at chemically modified gold surfaces," *Analytical Chemistry*, vol. 69, no. 24, pp. 4939–4947, 1997.

[41] K. Choi, H. J. Youn, Y. C. Ha, K. J. Kim, and J. Do Choi, "Detection of cholera cells using surface plasmon resonance sensor," *The Journal of Microbiology*, vol. 36, no. 1, pp. 43–48, 1998.

[42] M. Hayat, "Colloidal au: Principles," *Methods and Applications (California: Academic)*, 1989.

[43] K. Mishra, D. Kumar Raj, R. Hazra, and A. Dash, "A simple, artificial-membrane feeding method for the radio-isotope labelling of aedes aegypti polypeptides in vivo," *Annals of Tropical Medicine & Parasitology*, vol. 99, no. 8, pp. 803–806, 2005.

[44] T. Kaláb and P. Skládal, "Disposable multichannel immunosensors for 2, 4-dichlorophenoxyacetic acid using acetylcholinesterase as an enzyme label," *Electroanalysis*, vol. 9, no. 4, pp. 293–297, 1997.

[45] M. S. T. Gonçalves, "Fluorescent labeling of biomolecules with organic probes," *Chemical reviews*, vol. 109, no. 1, pp. 190–212, 2008.

[46] D. Danon, L. Goldstein, Y. Marikovsky, and E. Skutelsky, "Use of cationized ferritin as a label of negative charges on cell surfaces," *Journal of ultrastructure research*, vol. 38, no. 5-6, pp. 500–510, 1972.

[47] K. Kerman, M. Kobayashi, and E. Tamiya, "Recent trends in electrochemical dna biosensor technology," *Measurement Science and Technology*, vol. 15, no. 2, p. R1, 2003.

[48] M. A. Gijs, "Magnetic bead handling on-chip: new opportunities for analytical applications," *Microfluidics and nanofluidics*, vol. 1, no. 1, pp. 22–40, 2004.

[49] J. W. Bulte, "In vivo mri cell tracking: clinical studies," *American Journal of Roentgenology*, vol. 193, no. 2, pp. 314–325, 2009.

[50] A. S. Lübbe, C. Alexiou, and C. Bergemann, "Clinical applications of magnetic drug targeting," *Journal of Surgical Research*, vol. 95, no. 2, pp. 200–206, 2001.

[51] D. Hall, R. Gaster, T. Lin, S. Osterfeld, S. Han, B. Murmann, and S. Wang, "Gmr biosensor arrays: A system perspective," *Biosensors and Bioelectronics*, vol. 25, no. 9, pp. 2051–2057, 2010.

[52] G. Li, V. Joshi, R. L. White, S. X. Wang, J. T. Kemp, C. Webb, R. W. Davis, and S. Sun, "Detection of single micron-sized magnetic bead and magnetic nanoparticles using spin valve sensors for biological applications," *Journal of applied physics*, vol. 93, no. 10, pp. 7557–7559, 2003.

[53] M. Eddowes, "Direct immunochemical sensing: basic chemical principles and fundamental limitations," *Biosensors*, vol. 3, no. 1, pp. 1–15, 1987.

[54] B. Kattenbeck, A. Rohrhofer, M. Niedrig, H. Wolf, and S. Modrow, "Defined amino acids in the gag proteins of human immunodeficiency virus

type 1 are functionally active during virus assembly," *Intervirology*, vol. 39, no. 1-2, pp. 32–39, 1996.

[55] T. M. Squires, R. J. Messinger, and S. R. Manalis, "Making it stick: convection, reaction and diffusion in surface-based biosensors," *Nature biotechnology*, vol. 26, no. 4, p. 417, 2008.

[56] A. Sadana and A. M. Beelaram, "Antigen-antibody diffusion-limited binding kinetics of biosensors: a fractal analysis," *Biosensors and Bioelectronics*, vol. 10, no. 3-4, pp. 301–316, 1995.

[57] N. L. Hubert H. Girault, "Adsorption in biosensors," *LEPA - Laboratory of Physical and Analytical Electrochemistry - EPFL*.

[58] P. Delahay and I. Trachtenberg, "Adsorption kinetics and electrode processes," *Journal of the American Chemical Society*, vol. 79, no. 10, pp. 2355–2362, 1957.

[59] M. Srisa-Art, E. C. Dyson, A. J. deMello, and J. B. Edel, "Monitoring of real-time streptavidin- biotin binding kinetics using droplet microfluidics," *Analytical chemistry*, vol. 80, no. 18, pp. 7063–7067, 2008.

[60] H. Kogelnik, "2. theory of dielectric waveguides," in *Integrated optics*. Springer, 1975, pp. 13–81.

[61] W. Bogaerts, P. De Heyn, T. Van Vaerenbergh, K. De Vos, S. Kumar Selvaraja, T. Claes, P. Dumon, P. Bienstman, D. Van Thourhout, and R. Baets, "Silicon microring resonators," *Laser & Photonics Reviews*, vol. 6, no. 1, pp. 47–73, 2012.

[62] K. M. Krishnan, "Transactions on magnetics," *IEEE Magnetics Society*, vol. 46, no. 7, pp. C2–C2, 2010.

[63] R. C. O'handley, *Modern magnetic materials: principles and applications.* Wiley, 2000.

[64] W. F. Brown Jr, "Thermal fluctuations of a single-domain particle," *Physical Review*, vol. 130, no. 5, p. 1677, 1963.

[65] L. Néel, "Théorie du traînage magnétique des substances massives dans le domaine de rayleigh," *J. phys. radium*, vol. 11, no. 2, pp. 49–61, 1950.

[66] W. Coffey, P. Cregg, and Y. Kalmykov, "On the theory of debye and néel relaxation of single domain ferromagnetic particles," *Advances in Chemical Physics*, vol. 83, pp. 263–464, 1992.

[67] S. M. Barnett and R. Loudon, "On the electromagnetic force on a dielectric medium," *Journal of Physics B: Atomic, Molecular and Optical Physics*, vol. 39, no. 15, p. S671, 2006.

[68] S. S. Shevkoplyas, A. C. Siegel, R. M. Westervelt, M. G. Prentiss, and G. M. Whitesides, "The force acting on a superparamagnetic bead due to an applied magnetic field," *Lab on a Chip*, vol. 7, no. 10, pp. 1294–1302, 2007.

[69] S. Arnold, M. Khoshsima, I. Teraoka, S. Holler, and F. Vollmer, "Shift of whispering-gallery modes in microspheres by protein adsorption," *Optics letters*, vol. 28, no. 4, pp. 272–274, 2003.

[70] K. Tiefenthaler and W. Lukosz, "Sensitivity of grating couplers as integrated-optical chemical sensors," *JOSA B*, vol. 6, no. 2, pp. 209–220, 1989.

[71] E. Valera, M. S. McClellan, and R. C. Bailey, "Magnetically-actuated, bead-enhanced silicon photonic immunosensor," *Analytical Methods*, vol. 7, no. 20, pp. 8539–8544, 2015.

[72] V. Raghunathan, N. Y. Winnie, J. Hu, T. Izuhara, J. Michel, and L. Kimerling, "Athermal operation of silicon waveguides: spectral, second order and footprint dependencies," *Optics express*, vol. 18, no. 17, pp. 17 631–17 639, 2010.

[73] M. S. Luchansky and R. C. Bailey, "Silicon photonic microring resonators for quantitative cytokine detection and t-cell secretion analysis," *Analytical chemistry*, vol. 82, no. 5, pp. 1975–1981, 2010.

[74] ——, "Rapid, multiparameter profiling of cellular secretion using silicon photonic microring resonator arrays," *Journal of the American Chemical Society*, vol. 133, no. 50, pp. 20 500–20 506, 2011.

[75] M. S. Luchansky, A. L. Washburn, T. A. Martin, M. Iqbal, L. C. Gunn, and R. C. Bailey, "Characterization of the evanescent field profile and bound mass sensitivity of a label-free silicon photonic microring resonator biosensing platform," *Biosensors and Bioelectronics*, vol. 26, no. 4, pp. 1283–1291, 2010.

[76] J. T. Kindt, M. S. Luchansky, A. J. Qavi, S.-H. Lee, and R. C. Bailey, "Subpicogram per milliliter detection of interleukins using silicon photonic microring resonators and an enzymatic signal enhancement strategy," *Analytical chemistry*, vol. 85, no. 22, pp. 10 653–10 657, 2013.

[77] J. F. Marko and S. Cocco, "The micromechanics of dna," *Physics World*, vol. 16, no. 3, p. 37, 2003.

[78] R. Padinhateeri and G. I. Menon, "Stretching and bending fluctuations of short dna molecules," *Biophysical journal*, vol. 104, no. 2, pp. 463–471, 2013.

[79] J. P. Peters and L. J. Maher, "Dna curvature and flexibility in vitro and in vivo," *Quarterly reviews of biophysics*, vol. 43, no. 1, pp. 23–63, 2010.

[80] T. Strick, J.-F. Allemand, V. Croquette, and D. Bensimon, "Twisting and stretching single dna molecules," *Progress in biophysics and molecular biology*, vol. 74, no. 1-2, pp. 115–140, 2000.

[81] C. Bustamante, S. B. Smith, J. Liphardt, and D. Smith, "Single-molecule studies of dna mechanics," *Current opinion in structural biology*, vol. 10, no. 3, pp. 279–285, 2000.

[82] J. Lottersberger, J. Salvetti, L. Beltramini, and G. Tonarelli, "Antibody recognition of synthetic peptides mimicking immunodominant regions of hiv-1 p24 and 017 proteins," *Revista Argentina de microbiologia*, vol. 36, no. 4, p. 151, 2004.

[83] N. Peserico, A. Annoni, A. Varriale, S. D'Auria, L. Bellieres, F. Cuesta-Soto, M. Rodrigo, S. Peransi, and A. Melloni, "Experimental demonstration of integrated photonic free-label biosensor for cbrn threats using microring resonators," in *Transparent Optical Networks (ICTON), 2016 18th International Conference on.* IEEE, 2016, pp. 1–4.

[84] M. Donolato, E. Sogne, B. T. Dalslet, M. Cantoni, D. Petti, J. Cao, F. Cardoso, S. Cardoso, P. Freitas, M. F. Hansen *et al.*, "On-chip measurement of the brownian relaxation frequency of magnetic beads using magnetic tunneling junctions," *Applied Physics Letters*, vol. 98, no. 7, p. 073702, 2011.

[85] P. P. Sharma, "Magnetoresistive and opto-magnetic biosensors," *Politecnico di Milano*.